Search for the Decays of the Λ_b^0 Baryon with the DØ Experiment

Enrique Camacho Perez

Department of Physics

CINVESTAV

A thesis submitted for the degree of

Doctor of Philosophy

November 25, 2011

Contents

Chapter 1

Introduction

This thesis presents work I performed within the DØ Collaboration to make the measurement of the Branching Ratio of Λ_b^0 baryon in the channel $\Lambda_b^0 \to J/\psi\Lambda^0$. The b-hadron such as the Λ_b^0 are currently the subject of much research in both the theorical and experimental particle physics communities. Measurements of the production and decays of b-hadrons can improve the understanding of the electroweak and strong interactions described by the Standard Model of particle physics, as well as proving opportunities to search for physics beyond the Standard Model.

The DØ Collaboration is based at Fermilab in Batavia Illinois, USA. Fermilab is home of the Tevatron, that was up to December 2009 the highest energy particle accelerator in the world. Protons collided with anti-protons inside of the DØ and CDF detectors, at a centre of mass energy of approximately 2 TeV. A vast range of process may ocurr when the particle collide, in this environment a large number of b-hadrons are produced, allowing the Tevatron to be an important instrument in the study of their physics properties.

This thesis is organised as follows: The Second Chapter provides a brief . An overview of the experimental environment, the FERMILAB collider and the DØ detector are presented in Chapter 3. This is followed by an introduction into event reconstruction and object identification in Chapter 4 and the $f(b \to \Lambda_b^0) \times \mathcal{B}(\Lambda_b^0 \to J/\psi\Lambda^0)$ calculation in Chapter 5. The optimisation of the analyses is presented in Chapter 6. The results and consistency estudies are presented in the Chapeters 7 and 8. In the Chapter 10 is presented an estimate value of

$\mathcal{B}(\Lambda_b^0 \to J/\psi\Lambda^0)$ In Chapter 11 the search for the rare Baryonic Flavor-Changing Neutral Current Decay $\Lambda_b^0 \to \mu^+\mu^-\Lambda^0$ is presented. This thesis is concluded with an outlook and a summary.

Chapter 2

Overview

The first observation of the Λ_b^0 was reported more than a decade ago from the UA1 Collaboration at CERN [1], where 16 ± 5 events were reconstructed in the exclusive decay model $\Lambda_b^0 \to J/\psi\Lambda^0$ and a branching fraction of $\mathcal{B}(\Lambda_b^0 \to J/\psi\Lambda^0) = (1.8 \pm 1.1) \times 10^{-2}$ was determined. Later, the CDF experiment put an upper limit of $\mathcal{B}(\Lambda_b^0 \to J/\psi\Lambda^0) < 0.5 \times 10^{-2}$ at the 90% confidence level, using 2.6 pb^{-1} of data collected during 1988-1989 [2]. The most recent study was reported by the CDF experiment in 1997 [3], using 110 pb^{-1} of $p\bar{p}$ collision data taken at $\sqrt{s} = 1.8$ TeV, and measuring $f(b \to \Lambda_b) \cdot \mathcal{B}(\Lambda_b^0 \to J/\psi\Lambda^0) = (4.7 \pm 2.3) \times 10^{-5}$.

2.1 b-hadron production fractions

Quantities such as b-hadron production fractions, b-hadron lifetimes, and neutral B-meson oscillation frequencies have been studied in the nineties at LEP and SLC (e^+e colliders at $\sqrt{s} = m_Z$) as well as at the first version of the Tevatron ($p\bar{p}$ collider at $\sqrt{s}$ =1.8 TeV). Since then precise measurements of the B^0 and B^+ lifetimes, as well as of the B^0 oscillation frequency, have also been performed at the asymmetric B factories, KEKB and PEPII (e^+e colliders at$\sqrt{s} = m_{\gamma(4S)}$) while measurements related to the other b-hadrons, in particular B_s , B_c and Λ_b^0 , are being performed at the upgraded Tevatron ($\sqrt{s} = 1.96$ TeV). In most cases, these basic quantities, although interesting by themselves, became necessary ingredients for the more complicated and refined analyses at the asymmetric B

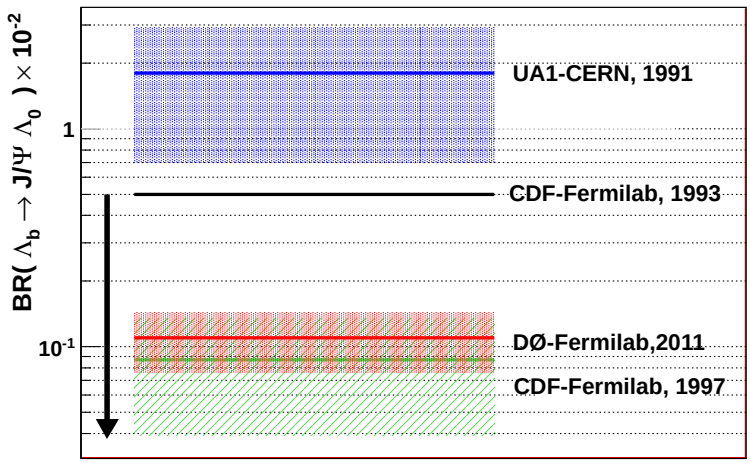

Figure 2.1: Different measurements of $\mathcal{B}(\Lambda_b^0 \to J/\psi\Lambda^0)$

factories and at the Tevatron, in particular the time-dependent CP asymmetry measurements. It is therefore important that the best experimental values of these quantities continue to be kept up-to-date and improved.

2.1.1 b-hadron production fractions at high energy

At high energy, all species of weakly-decaying b hadrons can be produced, either directly or in strong and electromagnetic decays of excited b-hadrons. It is often assumed that the fractions of these different species are the same in unbiased samples of high-p_T b-jets originating from Z^0 decays or from $p\bar{p}$ collisions at the Tevatron. This hypothesis is plausible considering that, in both cases, the last step of the jet hadronization is a non-perturbative QCD process occurring at the scale of Λ_{QCD} . On the other hand, there is no strong argument to claim that these fractions should be strictly equal, so this assumption should be checked experimentally. Although the available data is not sufficient at this time to perform a significant check, it is expected that more data from Tevatron Run II may improve this situation and allow one to confirm or disprove this assumption with reasonable confidence. Meanwhile, the attitude adopted here is that these fractions are assumed to be equal at all high-energy colliders until demonstrated

otherwise by experiment [1].

However, as explained below, the measurements performed at LEP and at the Tevatron show discrepancies. Therefore we present three sets of averages: one set including only measurements performed at LEP, a second set including only measurements performed at the Tevatron, and a third set including measurements performed at both LEP and Tevatron.

Contrary to what happens in the charm sector where the fractions of D^+ and D^0 are different, the relative amount of B^+ and B^0 is not affected by the electromagnetic decays of excited $B^{+*}$and B^{0*} states and strong decays of excited $B^{+**}$and B^{0**} states. Decays of the type $B_s \to B_() K$ also contribute to the B^+ and B^0 rates, but with the same magnitude if mass effects can be neglected. We therefore assume equal production ofB^+ and B^0. We also neglect the production of weakly-decaying states made of several heavy quarks (like B_c^+ and other heavy baryons) which is known to be very small. Hence, for the purpose of determining the b-hadron fractions, we use the constraints

$$\begin{aligned} f_u &= f_d \\ f_u + f_d + f_s + f_{baryon} &= 1, \end{aligned} \tag{2.1}$$

where f_u , f_d , f_s and f_{baryon} are the unbiased fractions of B^+ , B^0 , B_s and b-baryons, respectively.

The LEP experiments have measured $f_s \times \mathcal{B}(B_s^0 \to D_s^- l^+ \nu_l X)$ [4], $f(b \to \Lambda_b) \times \mathcal{B}(\Lambda_b \to \Lambda_c^+ l^- \bar{\nu}_l X)$ [? ?], and $f(b \to \Xi_b^-) \times \mathcal{B}(\Xi_b^- \to \Xi^- l^- \bar{\nu}_l X)$ [7, 8] [2]

from partially reconstructed final states including a lepton, f_{baryon} from protons identified in b events [10], and the production rate of charged b-hadrons [11]. The various b-hadron fractions have also been measured at CDF using lepton-charm final states [12, 13, 14] [3]

and double semileptonic decays with $K\mu^+\mu^-$ and $\varphi\mu^+\mu^-$ final states [15].

[1] It is likely that the b-hadron fractions in low-p_T jets at a hadronic machine be different; in particular, beam-remanent effects may enhance the b-baryon production

[2]The DELPHI result of [8]is considered to supersede an older one [9]

[3]CDF updated their measurement of f_{baryon}/f_d [12] to account for a measured p_T dependence between exclusively reconstructed Λ_b^0 and B^0 [14]

Recent measurements of heavy flavor baryon production at the Tevatron are included in the determination of f_{baryon} [42, 17, 18] using the constraint

$$\begin{aligned} f(b \to b_{baryon}) = & \quad f(b \to \Lambda_b) + f(b \to \Xi_b^0) + f(b \to \Xi_b^-) + f(b \to \Omega_b^-) \\ = & \quad f(b \to \Lambda_b) \times \left(1 + 2\frac{\Xi_b^0}{\Lambda_b} + \frac{\Xi_b^0}{\Omega_b^-}\right) \end{aligned} \tag{2.2}$$

where isospin invariance is assumed in the production of Ξ_b^0 and Ξ_b^- . Other b-baryons are expected to decay strongly or electromagnetically to those baryons listed. For the production measurements, both CDF and DØ reconstruct their b-baryons exclusively to final states which include a J/Ψ and a hyperon ($\Lambda_b \to J/\psi\Lambda$, $\Xi_b \to J/\psi\Xi^-$ and $\Omega_b \to J/\psi\Omega^-$). We assume that the partial decay width of a b baryon to a J/Ψ and the corresponding hyperon is equal to the partial width of any other b-baryon to a J/Ψ and the corresponding hyperon.

All these published results have been combined following the procedure and assumptions described in [19], to yield

$$\begin{aligned} fu = & \quad fd = 0.405 \pm 0.012 \\ fs = & \quad 0.100 \pm 0.017 \\ f_{baryon} = & \quad 0.089 \pm 0.022 \end{aligned} \tag{2.3}$$

under the constraints of Eq. 2.1. Following the PDG prescription, we have scaled the combined uncertainties on these fractions by 1.4 to account for slight discrepancies in the input data. Repeating the combinations, we obtain

$$\begin{aligned} fu = & \quad fd = 0.407 \pm 0.009 \\ fs = & \quad 0.087 \pm 0.014 \\ f_{baryon} = & \quad 0.099 \pm 0.016 \end{aligned} \tag{2.4}$$

when using the LEP data only, and

$$
\begin{aligned}
fu = \quad & fd = 0.322 \pm 0.032 \\
fs = \quad & 0.094 \pm 0.016 \\
f_{baryon} = \quad & 0.262 \pm 0.073
\end{aligned} \tag{2.5}
$$

when using the Tevatron data only. When the Tevatron and LEP data are separated, we find no need to scale the uncertainties of either combination. For these combinations other external inputs are used, e.g. the branching ratios of B mesons to final states with a D, D^* or D^{**} in semileptonic decays, which are needed to evaluate the fraction of semileptonic B_s decays with a D_s^- in the final state.

Table 2.1: Fractions of the different b-hadron species in an unbiased sample of weakly-decaying b hadrons, obtained from both direct and mixing measurements. The last column includes measurements performed at both LEP and Tevatron

Quantity		in Z decays	at Tevatron	Combined
B^+ or B^0 fraction	$f_u = f_d$	0.403 ± 0.009	0.339 ± 0.031	0.404 ± 0.012
B_s^0 fraction	f_s	0.103 ± 0.009	0.111 ± 0.014	0.109 ± 0.012
b-baryon fraction	f_{baryon}	0.090 ± 0.015	0.211 ± 0.069	0.083 ± 0.020
Correlation between	f_s and $f_u = f_d$	0.523	+0.426	0.475
Correlation between	f_{baryon} and $f_u = f_d$	-0.870	0.984	0.854
Correlation between	f_{baryon} and f_s	+0.035	0.582	0.053

2.2 Results for b-baryons at DØ experiment

The DØ detector at the Fermilab have each accumulated more that 10 fb^{-1} of integrated luminosity. The corresponding large datasets enable the to perform studies of heavy flavor hadron properties. Here is presented the some DØ measurements, focusing on lifetime and b-baryon spectroscopy.

2.2.1 Lifetime

Precise lifetimes are key in extracting the weak parameters that are important for understanding the role of the CKM matrix in CP violation, such as the determination of V_{cb} and $B_s^0 \bar{B}_s^0$ mixing measurements.

- Measurement of the Λ_b^0 Lifetime in the Decay $\Lambda_b^0 \to J/\psi \Lambda^0$ [20, 21]
- Measurement of the Λ_b^0 Lifetime Using Semileptonic Decays [20]

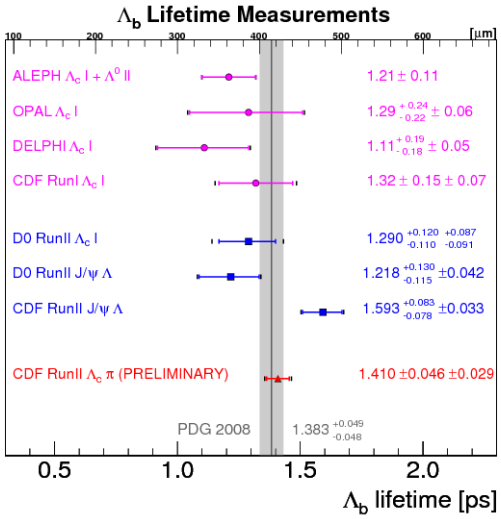

Figure 2.2: Λ_b^0 lifetime result compared with PDG 2008 and other measurements contributing to it (right).

2.2.2 b-baryon spectroscopy

DØ have had major contribution to b-baryon spectroscopy, with the Ξ_b^- (dsb) Ω_b^- (ssb) baryons.

- Observation of the Doubly Strange b-baryon Ω_b^- [24]
- Direct Observation of the Strange b-baryon Ξ_b^- [23]

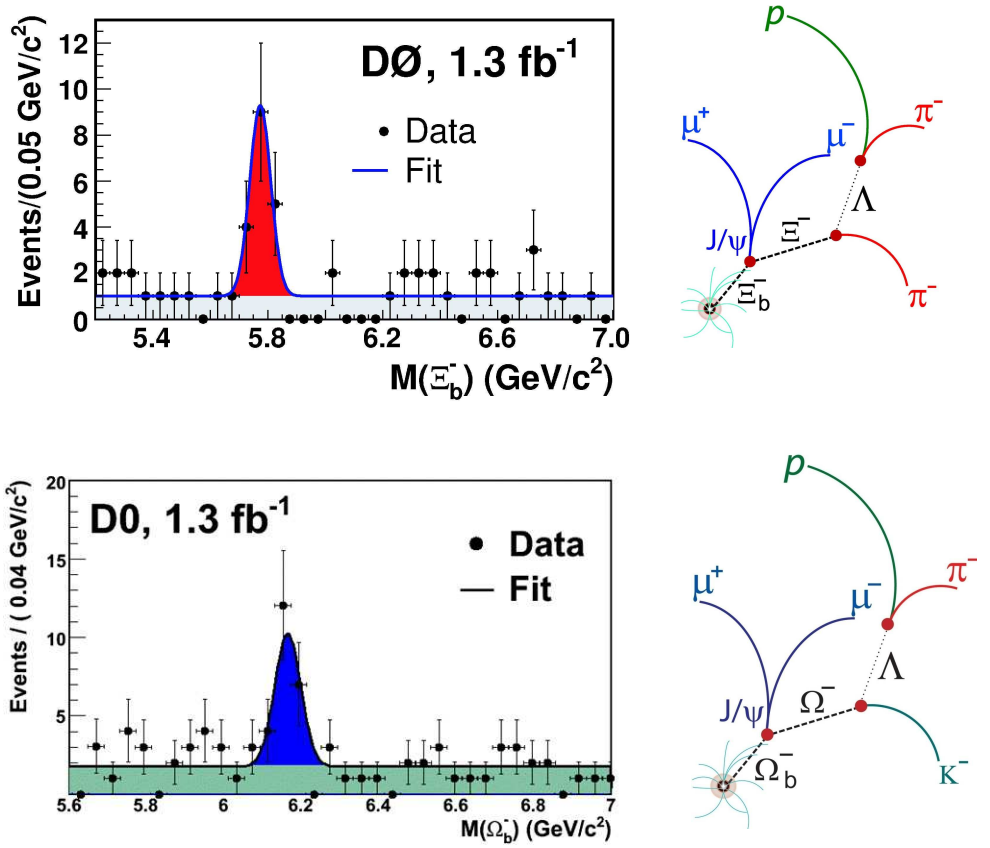

Figure 2.3: Mass distributions for Ξ_b^- and Ω_b^-, and its schematic decay topology

2.3 Rare decay $\Lambda_b^0 \to \mu^+\mu^-\Lambda^0$

Rare decays of hadrons containing bottom quarks through the process $b \to s\mu\mu$, occur in the standard model (SM) with $\mathcal{O}(10^6$) branching ratios [25, 26]. The b and s quarks carry the same charge but different flavor, so this process is a flavor-changing neutral-current (FCNC) decay. FCNC decays are suppressed at tree level in the SM, and must occur through higher order, and more suppressed, loop diagrams. Their suppressed nature and clean experimental signature, along with reliable theoretical predictions for their rates [25, 27, 28], make them excellent search channels for new physics. With multi-body final states, these modes offer sensitivity to new physics in a number of kinematic distributions in addition to the total branching ratio.

In addition, the study of the baryonic $b \to s\mu\mu$ decays is very important,

since the baryonic FCNC decays are sensitive to the helicity structure of effective Hamiltonian, which is lost in the hadronization of the mesonic decays [29]. Although the theoretical calculations of the exclusive baryonic $b \to s\mu\mu$ decays have large uncertainties compared to the mesonic decays due to additional degrees of freedom in the baryon bound states, the measurements of the total and the differential branching ratios can help the improvement of the theoretical treatments. One can also compare the measurements of the mesonic $b \to s\mu\mu$ decays with the baryonic decays, which follow the common quark transition. Measurements of both mesonic and baryonic FCNC decays therefore provide additional tests of the SM and its extensions. However, no b baryon FCNC decay has been observed and there are few experimental constraints on their decay rates.

The $\Lambda_b^0 \to \mu^+\mu^-\Lambda^0$ decay is considered promising in this respect [29, 30, 31, 32] and experimentally accessible since the branching ratio is predicted as$(4.0 \pm 1.2) \times 10^6$ [31].

CDF Collaboration [33] report the first observation of the baryonic flavor-changing neutral current decay $\Lambda_b^0 \to \mu^+\mu^-\Lambda^0$ with 24 signal events and a statistical significance of 5.8 Gaussian standard deviations. This measurement uses a $p\bar{p}$ collisions data sample corresponding to 6.8 fb^{-1} at $\sqrt{s} = 1.96$ TeV. The measurement that was reported for the branching ratio is $\mathcal{B}(\Lambda_b^0 \to \mu^+\mu^-\Lambda^0) = 1.73 \pm 0.69 \times 10^{-6}$

Chapter 3

Experimental Environment

3.1 Tevatron and DØ Detector

The data analyzed in this thesis were produced via the interaction of two primary experimental instruments: the Fermilab Tevatron and the DØ detector. The data were recorded during Run IIa and RunIIb of the Tevatron in the years 2004-2009. This experimental procedure consists of the Tevatron preparing high-energy beams of protons and anti-protons which are brought into collision. These collisions occur at the center of two particle detectors: the collider detector at Fermilab (CDF) and the DØ detector. These detectors measure the final states of the particles that are produced in the interactions initiated in the colliding beams.

3.1.1 The Tevatron Accelerator Complex

The Fermilab accelerator complex can be sub-divided into two main components, proton and antiproton production, including the storage of antiprotons inside the Recycler, and acceleration and injection of protons and antiprotons into the Tevatron itself. Once all the protons and antiprotons are injected into the Tevatron, the bunches are then accelerated to 980 GeV, and after cleaning of the bunches to remove the proton and antiproton halos, are then made to collide at two interaction points. It is at these interaction points that the two experiments lie, the Collider Detector at Fermilab (CDF) and DØ. The layout of the Fermilab

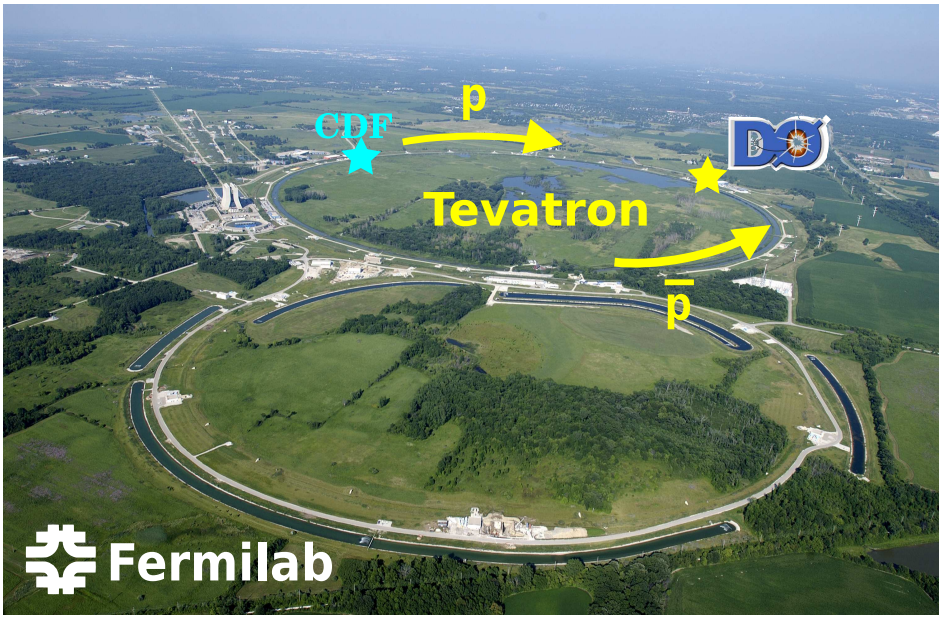

Figure 3.1: Tevatron Accelerator, CDF and DØ experiment

accelerator is shown in Figure 3.2.

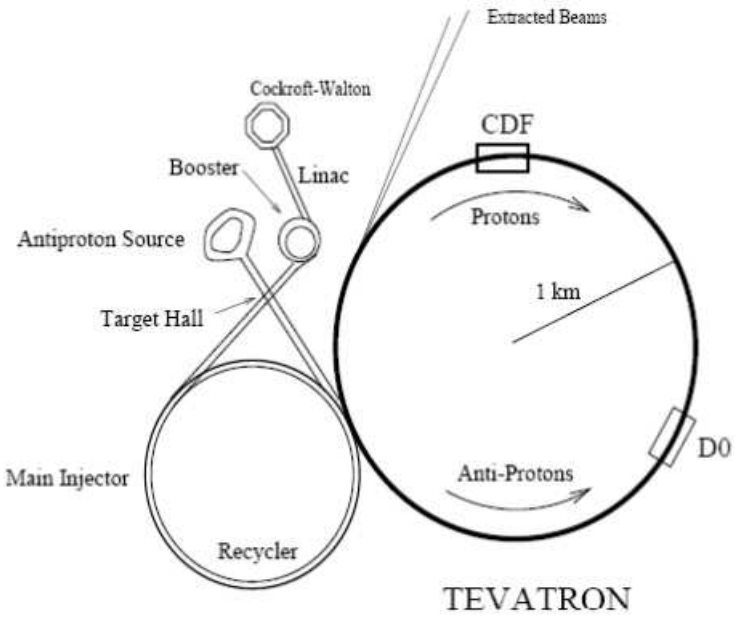

Figure 3.2: The Fermilab accelerator complex

3.1.1.1 Proton and antiproton production

The accelerator chain begins with proton production. Negative hydrogen ions are accelerated to 750 keV by a Cockcroft-Walton accelerator and are then further accelerated to 400 MeV within the Linac. From there the H ions are stripped of their electrons and the remaining protons are injected into the Booster where they are accelerated to 8 GeV and passed onto the Main Injector. The Booster is a synchrotron with a 75 m radius and is also used to provide 8 GeV protons for the MiniBooNE and SciBooNE neutrino experiments. The Main Injector is a 3 km synchrotron which accelerates the 8 GeV to either 120 GeV for antiproton production, the NuMI neutrino experiment and other fixed target experiments, or to 150 GeV ready for injection into the Tevatron. Antiproton production begins with the 120 GeV proton beam from the Main Injector. This is fired onto a Nickel alloy target from which a secondary spray of particles is formed. A Lithium lens is used to focus the spray and it is passed through a bending magnet in order to select 8 GeV antiprotons. These are collected first in the Debuncher, which cools the antiprotons and, once cooled enough, passed onto the Accumulator, which further cools the antiprotons and temporarily stores them ready for transfer to the Recycler. The Recycler is a fixed energy storage ring located in the Main Injector tunnel, designed for holding large numbers of 8 GeV antiprotons for a long period of time whilst further cooling the antiprotons.

3.2 The DØ Detector

The D0 detector [34] is one of the two detectors at the Tevatron accelerator at Fermilab. The detector performed extraordinarily well in Run I (19921996), as demonstrated by the discovery of the top quark [35] and many other published physics results. During Run I, the Tevatron operated using six bunches each of protons and anti-protons with 3500 ns between bunch crossings. In Run II, started in 2001, it is operated with 36 bunches of protons and 36 bunches of anti-protons with a bunch spacing of 396 ns. The instantaneous luminosity exceeds 4×10^{32} cm^{-2} s^{-1} , and around 11 fb^{-1} of data was delivered in Run II. The center-of- mass energy was 1.96 TeV in Run II compared to 1.8 TeV in Run I.

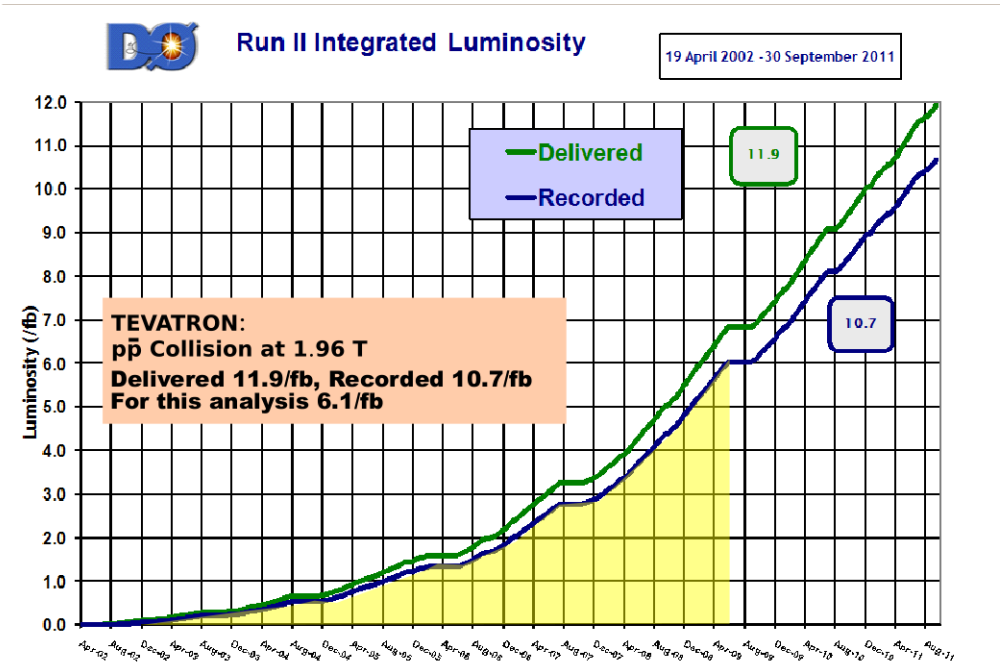

Figure 3.3: Cumulative integrated luminosity recorded by D0 during Run IIa. The difference between delivered and recorded luminosity arises from data acquisition inefficiencies, including hardware and software effects.

Figure 3.4 shows a cross-sectional view of the Run II D0 detector.

The detector consists of three major subsystems: central tracking detectors, uranium/liquid-argon calorimeters, and a muon spectrometer.

In the detector description and data analysis, we use a right- handed coordinate system in which the z-axis is along the proton direction and the y-axis is upward (Figure 3.4). The angles ϕ and θ are the azimuthal and polar angles, respectively. The r coordinate denotes the perpendicular distance from the z axis. The pseudorapidity, $\eta = -ln(tan(\theta/2))$, approximates the true rapidity,$y = 1/2ln[(E + p_z c)/(E - p_z c)]$, for finite angles in the limit that $(mc^2/E) \to 0$. We use the term forward to describe the regions at large $|\eta|$.

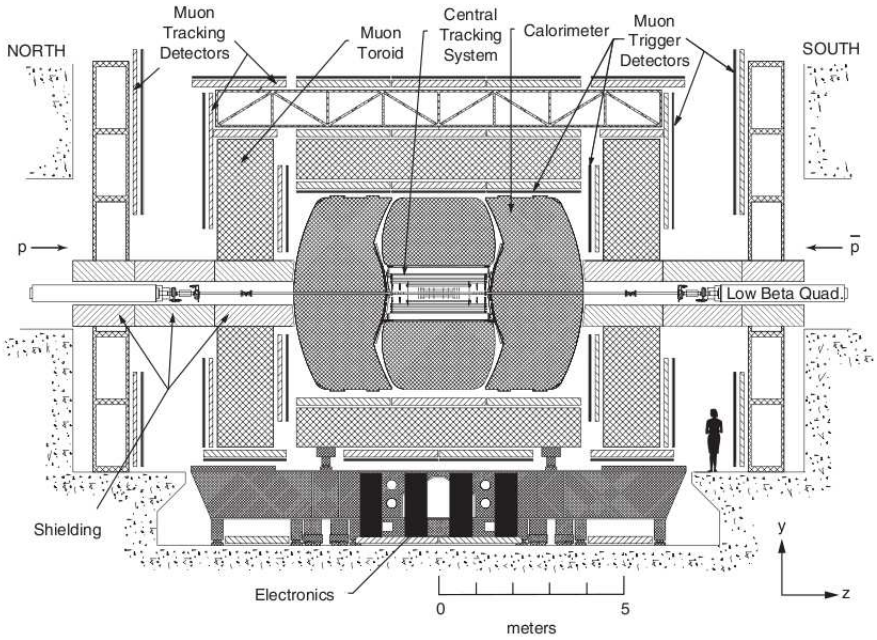

Figure 3.4: Diagram of the DØ detector, as installed in the collision hall and viewed from inside the Tevatron ring.

3.2.1 The Central Tracking Detector

Excellent tracking in the central region is necessary for studies of top quark, electroweak, and b-physics and to search for new phenomena, including the Higgs boson.

The central tracking system consists of the silicon microstrip tracker (SMT) and the central fiber tracker (CFT) surrounded by a solenoidal magnet. It surrounds the DØ beryllium beam pipe. The two tracking detectors locate the primary interaction vertex with a resolution of about 35 mm along the beamline. They can tag b-quark jets with an impact parameter resolution of better than 15 mm in $r - \phi$ for particles with transverse momentum $p_T > 10$ GeV/c at $|\eta| = 0$. The high resolution of the vertex position allows good measurement of lepton p_T, jet transverse energy (E_T), and missing transverse energy ($\not\!\!E_T$). Calibration of the electromagnetic (EM) calorimeter using E=p for electrons is now possible. Both the SMT and CFT provide tracking information to the trigger. The SMT provides signals to the Level 2 and 3 trigger systems and is used to trigger on

displaced vertices from b-quark decay. The CFT provides a fast and continuous readout of discriminator signals to the Level 1 trigger system. A schematic view of the central tracking system is shown in Figure 3.5.

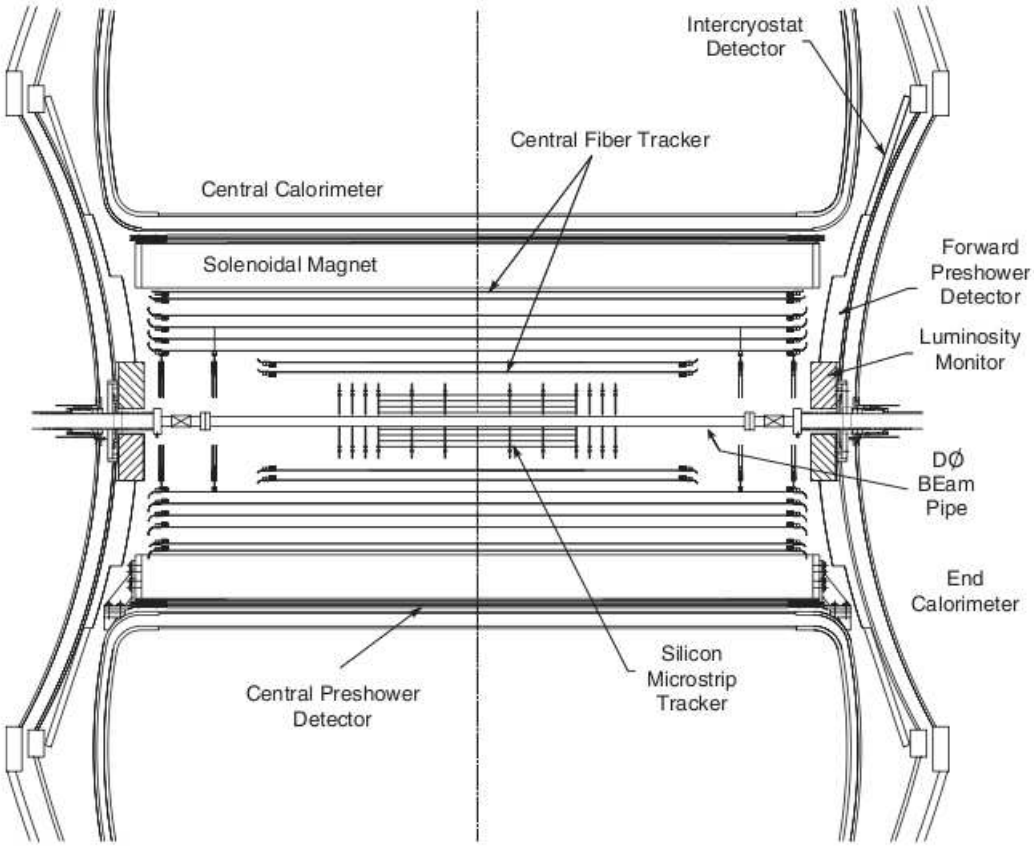

Figure 3.5: Cross-sectional view of the central tracking system in the $x-z$ plane. Also shown are the locations of the solenoid, the preshower detectors, luminosity monitor, and the calorimeters.

3.2.1.1 Silicon Microstrip Tracker

The innermost tracking system at DØ is the SMT, which is the closest detector component to the beryllium beam pipe3 of the Tevatron. The SMT provides high-resolution measurements of the paths of charged particles leaving the interaction region. The large z distribution of the $p\bar{p}$ interaction region ($\sigma_z \simeq 26cm$) provides

a challenge for designing a detector in which tracks are predominantly perpendicular to detector surfaces. This challenge motivates a detector geometry consisting of six barrels and sixteen disks of silicon wafers, creating a tracking coverage out to $|\eta| = 3.0$. A schematic of the SMT geometry is shown in Figure 3.6.

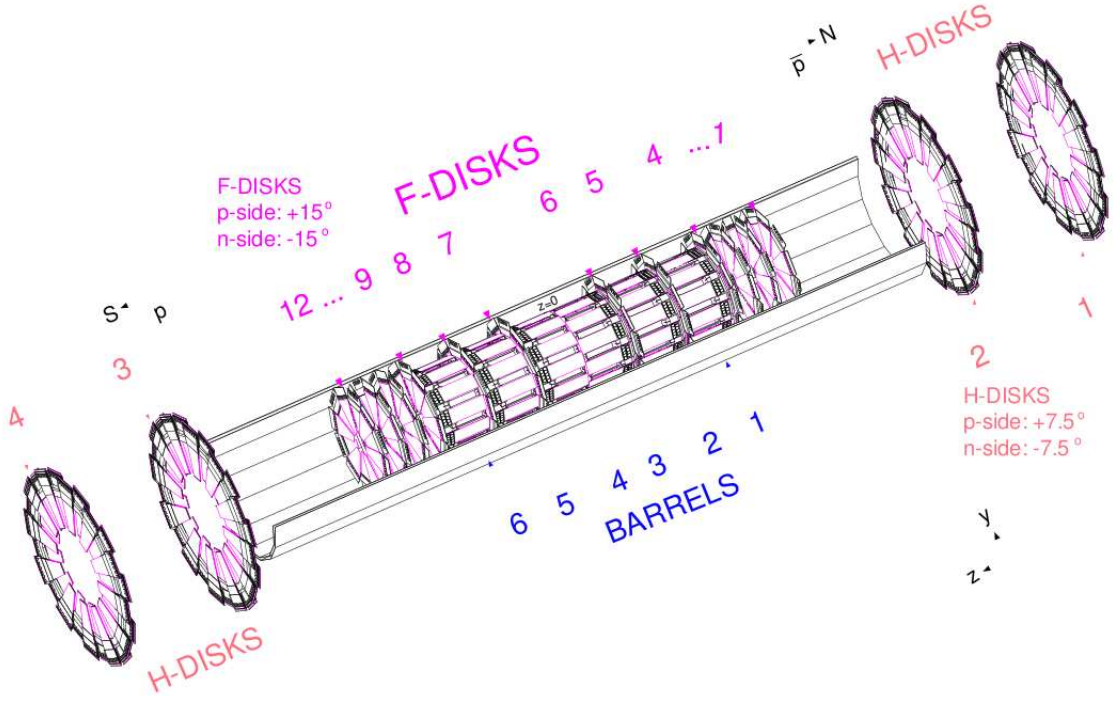

Figure 3.6: Schematic view of the SMT detector, illustrating the geometry of the barrel, F-disks, and H-disks.

The six barrel segments are 12 cm long and made up of four concentric layers of silicon wafers, allowing for $r\phi$ measurements of central tracks. Each layer of silicon is slightly overlapped to ensure full ϕ coverage. The six barrels provide coverage of the $|\eta| \leq 1.1$ region. Along the axis of the barrels are twelve 8 mm-thick disks, referred to as F-disks. The disks are made of twelve overlapping, double-sided silicon wedges, creating an annulus with central radius 2.6 cm and outer radius 10.5 cm. Two larger disks, referred to as H-disks, are placed on either end of the detector. These H-disks are made of 16 overlapping, single-sided silicon wedges, each forming an annulus with inner radius 9.5 cm and outer radius 26

cm. The F- and H-disks together provide rz and $r\phi$ tracking coverage out to $|\eta| = 3.0$. The SMT barrels and disk wedges are made of 300 μm-thick silicon wafers consisting of a n-type/p-type silicon interface (p-n junction). Interspersed on both sides of the silicon are thin conducting readout strips with a pitch varying from 50 μm to 153.5 μm. As charged particles pass through the silicon wafer, ionization produces electron-hole pairs. An applied bias voltage pulls these pairs (in opposite directions) to the readout strips, and the collected charge is stored in a capacitor array until the information is ready to be processed.

3.2.1.2 Central Fiber Tracker

The Central Fiber Tracker (CFT) lies immediately outside the SMT and provides tracking coverage up to $|\eta| = 2.0$ measurements of the SMT and CFT allow for improved tracking quality not achievable by either detector alone. The CFT consists of eight carbon fiber cylinders holding layers of scintillating fibers. Each cylinder supports a doublet layer of fibers oriented parallel to the beam line (axial fibers). The odd numbered cylinders (counting from the inside to outside) hold an additional doublet offset at alternating angles of$\pm 3^o$ (stereo fibers). The axial fibers provide ϕ measurements at a fixed radius and, when combined with the stereo fibers, can provide a measurement of z. Each fiber consists of a 775 μm polystyrene core that is doped with fluorescing molecules with peak emission at 535 nm. Surrounding the core are two 15 μm layers of cladding (acrylic and fluro-acrylic), increasing the light-collection efficiency. In total, the CFT contains 71,680 fibers. A quarter view schematic of the CFT is shown in Figure 3.4.

As charged particles pass through the fibers, scintillation light travels their length in both directions. The fibers, which range in length from 166 cm for the innermost cylinder to 257 cm for the outermost cylinders, have an aluminum mirror coating at one end to reflect photons back into the fiber. The other end is joined to clear fibers which guide the scintillation photons to a solid-state silicon device called a Visible Light Photon Counter (VLPC). Photons incident upon the surface of the VLPC are converted to electron-hole pairs, which are subsequently collected via a 6 V bias voltage. The VLPCs are grouped together in cassettes of 1024 VLPCs which are kept in liquid helium dewars to reduce electronic noise,

providing single-photon resolution.

3.2.1.3 Solenoid

A new addition to the DØ detector for Run II was a 2-T solenoid magnet that was added to allow for the determination of momentum of charged particles. The size of the magnet was restricted by the space in the central calorimeter void which is 2.73 m long with a 1.42 m diameter. It has two layers of 0.848 mm superconducting coil and operates at a temperature of 4.7 K and a current of 4749 A. The 2 T magnetic field has been measured to be uniform within 0.5%.

3.2.2 The Calorimeter

The DØ calorimeter lies outside the solenoid and measures the energies of electromagnetic particles (electrons, photons) and hadrons. This measurement is made by inducing interactions with incident particles via the material of the calorimeter, creating showers of secondary particles which lose energy through ionization in the calorimeters active medium. A measurement of a particle-s total energy is made when the showering process is fully contained. The calorimeter is a compensating, sampling calorimeter in which liquid argon is used as the active medium and depleted uranium (as well as copper and steel) is used as an absorber material. As it completely surrounds the inner detectors, the calorimeter has a modular design to provide access to the inner regions. This design consists of three cryostats, which are vessels containing the calorimeter and the cryogenics required to maintain the liquid argon at a constant temperature, and is shown in Figure 3.7 and Figure 3.8.

The calorimeter is comprised of three distinct modules: the Central Calorimeter (CC) covering the region $|\eta| < 1.2$ and two End Calorimeters (EC North and EC South) that extend coverage to $|\eta| \simeq 0.4$. The calorimeter modules themselves are further segmented into three sections. In order of increasing radius, these are the electromagnetic (EM), fine hadronic (FH), and coarse hadronic (CH) sections. The EM sections consist of four layers of depleted uranium absorber plates, each 3-4 mm thick. The FH section contain three (CC) or four (EC) layers of 6 mm-thick uranium- niobium (2%) alloy absorber plates. The outer CH section has

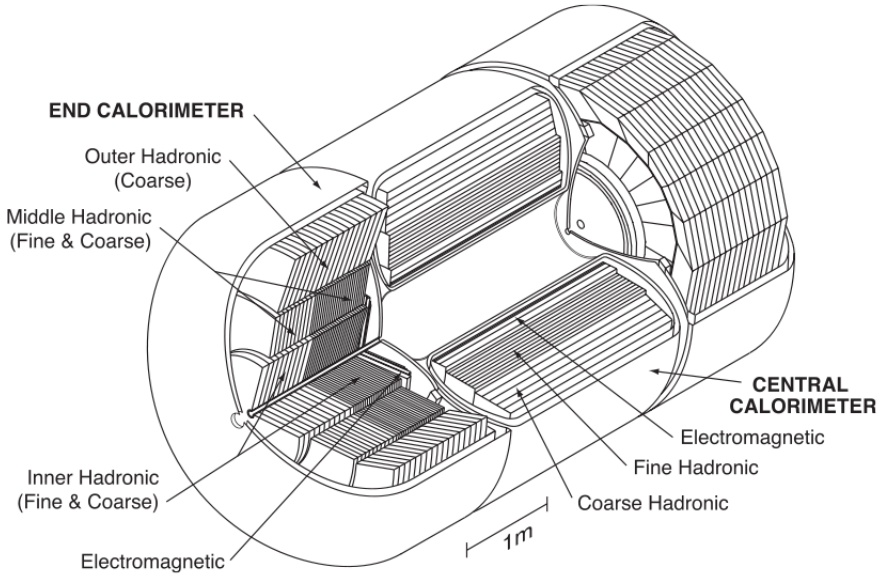

Figure 3.7: Cutaway view of the calorimeter system of the D detector.

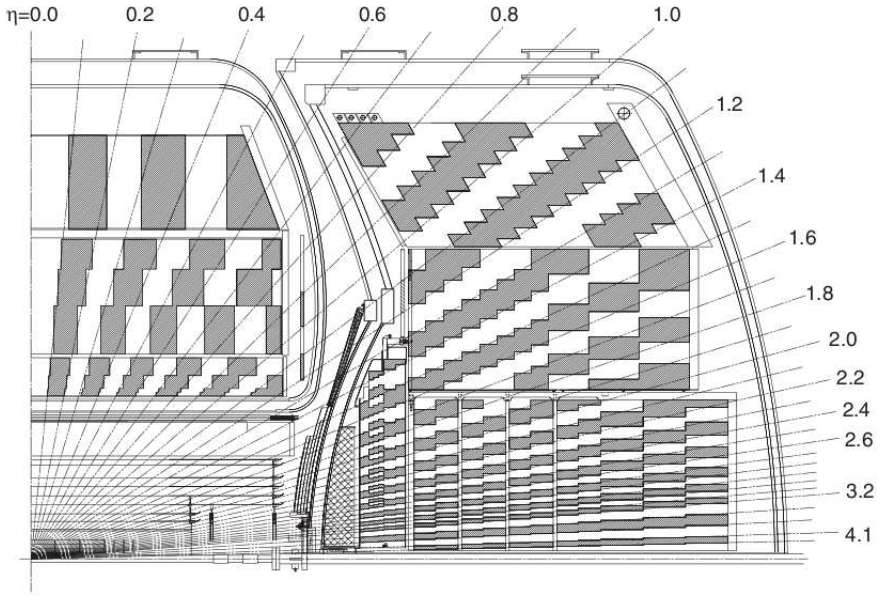

Figure 3.8: Schematic view of a portion of the DØ calorimeters showing the transverse and longitudinal segmentation pattern. The shading pattern indicates groups of cells ganged together for signal readout. The rays indicate pseudorapidity intervals from the center of the detector.

one 46.5 mm-thick absorber plate made of copper (CC) or steel (EC).

Each calorimeter layer is segmented into a set of readout cells. These cells are $\Delta\eta \times \Delta\phi = 0.1 \times 0.1$ in size, except in the third EM layer where the segmentation doubles. These readout cells are grouped radially to form a $\Delta\eta \times \Delta\phi = 0.2 \times 0.2$ readout geometry referred to as a tower. The readout cells consist of a group of adjacent unit cells immersed in the liquid argon of the calorimter. Each unit cell is a copper pad insulated with G10 plastic covered in a resistive epoxy coating. The resistive coating is held at a high voltage (~ 2.5 kV). The showering particles in the calorimeter ionize the liquid argon and the liberated electrons are drawn to the resistive coat. Via capacitive coupling, an image charge is induced on the copper pad. Readout electronics sample the charge on the pad, converting it to an analog signal proportional to the ionization energy recorded.

3.2.3 Intercryostat and Massless Gap Detectors

As evident in Figure 3.8, there is an uninstrumented region between the CC and EC covering the region $1.1 \simeq |\eta| \simeq 1.4$. The material in this region (cryostat walls, support structures, cabling...) can participate in shower evolution, and thus can impact jet measurements. To augment the shower sampling in this region, scintillator detectors have been mounted on the EC cryostat walls facing the gap. Each intercryostat detector (ICD) consists of 384 scintillator tiles of the same size as the calorimeter cells,$\Delta\eta \times \Delta\phi = 0.1 \times 0.1$. Separate single-cell structures, called massless gaps, are installed in the gap region to make further measurements of shower formation.

3.2.4 The Muon System

Electrons are stopped by the calorimeter, but the 200 times more massive muons pass through leaving only a fraction of their energy behind. Muons with energies between a few hundred MeV and a few hundred GeV are minimum ionizing particles, losing energy at a rate of around 0.25 GeV per nuclear interaction length traversed. Other than neutrinos, which are not detected at all, muons are the only SM particles that live long enough to travel through the detector, but are not

stopped by the calorimeter. Therefore, the muon system is the outermost section of the DØ detector designed to detect the muons as they exit the calorimeter.

The muon system has a rectangular geometry, like a cube, with three layers of detectors as shown in Figure 3.10 and Figure 3.10. The muon system consists of three primary components

- Wide Angle Muon Spectrometer (WAMUS) covering $|\eta| \leq 1$
- Forward Angle Muon Spectrometer (FAMUS) covering $1 \leq |\eta| \leq 2$
- A 1.8 Tesla iron toriodal magnet

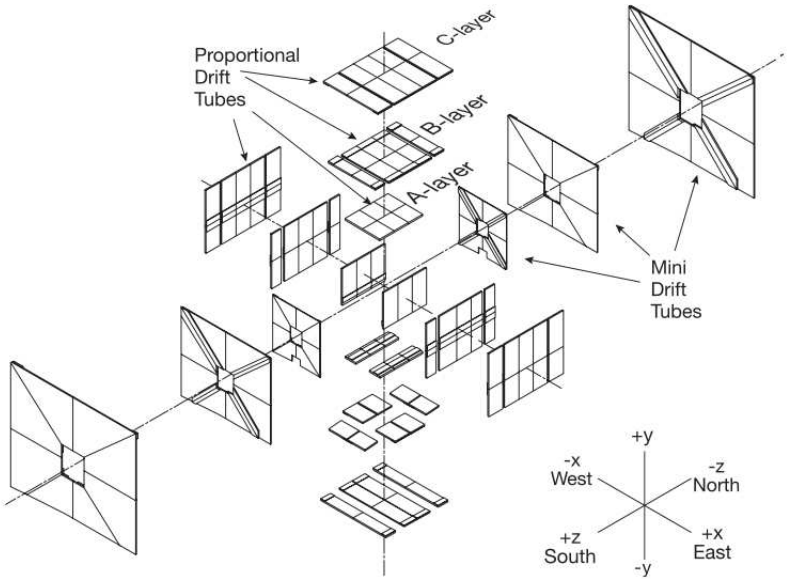

Figure 3.9: View of the muon wire chambers.

The WAMUS consists of two types of detector components: proportional drift tubes (PDTs) and scintillator tiles. These components are arranged in three layers, referred to as A-,B-, and C-layers. The A-layer is located inside the toroid and the B- and C-layers are outside the toroid. The FAMUS has a similar structure using mini drift tubes (MDTs) and scintillator pixels. The geometry of the muon system can be seen in Figure 3.10 and Figure 3.10. The muon drift tubes are filled with a gas mixture (80% argon, 10% CH4 , 10% CF4) which is easily

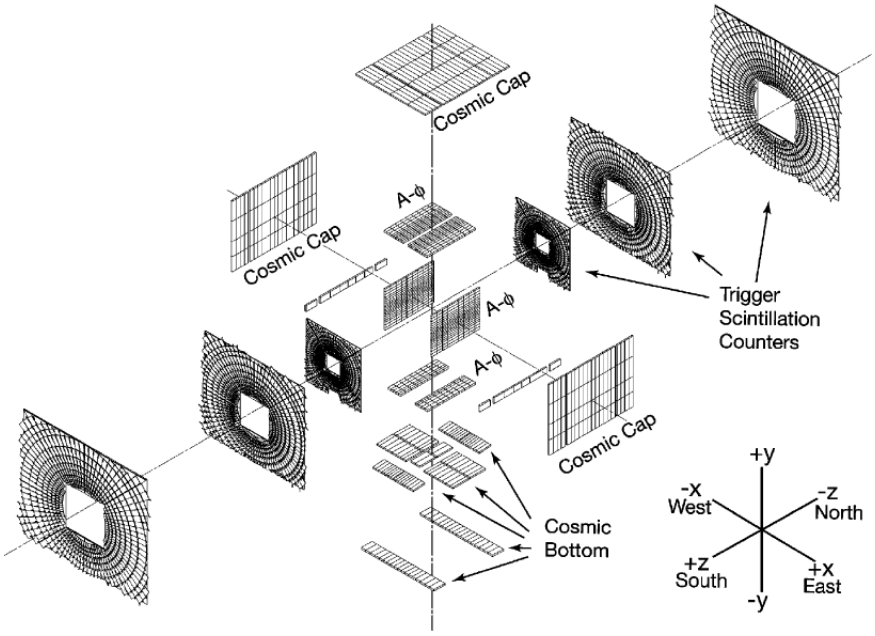

Figure 3.10: View of the muon scintillation detectors.

ionized by the passage of charged particles. Each tube contains a gold anode wire held at high voltage (relative to cathode pads on the top and bottom of the tube). The ionization is collected at the wire and converted to a signal via readout electronics, allowing for good position measurements but poor timing measurements ($\sim$ 500 ns resolution). The scintillators provide additional spatial information and $\sim$ 10 ns resolution time measurements, allowing for cosmic ray rejection. The iron toroid serves two purposes. First, it acts as an extra layer of dense shielding, effectively containing any hadronic showers which are not contained in the calorimeter. And second, its magnetic field provides a measurement of the muons momentum by comparing the position of hits in the inner layer to the outer layers. Whenever possible, the high-resolution tracks of the inner tracking detectors are used for making muon momentum measurements.

3.2.5 Luminosity Monitor

The Luminosity Monitor (LM) is the subdetector responsible for measuring the instantaneous luminosity being delivered to the DØ experiment. As the instanta-

neous luminosity drops steadily during beam collisions, an accurate measurement of the instantaneous luminosity allows for optimization of data taking rates and a reliable normalization measurement for specific event rates. The LM is constructed of two hodoscopes of plastic scintillation pixels mounted on the front faces of the EC calorimeters, as shown in Figure 3.11 and Figure 3.12. The LM spans the region $2.7 \leq |\eta| \leq 4.4$ and measures the inclusive rate of inelastic $p\bar{p}$ scattering by detecting charged particles from the interaction region.

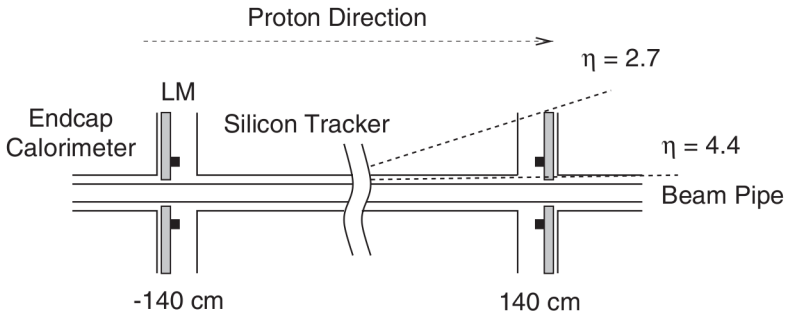

Figure 3.11: Schematic drawing showing the location of the LM detectors.

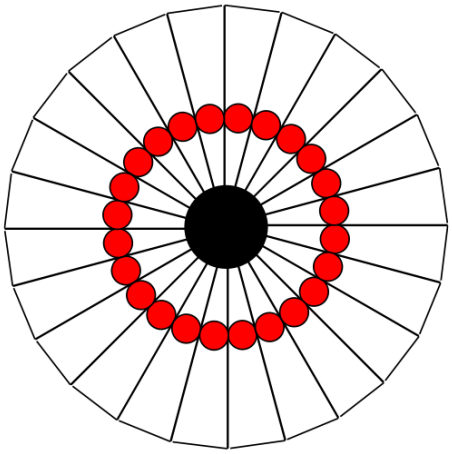

Figure 3.12: Schematic drawing showing the geometry of the LM counters and the locations of the PMTs (solid dots).

3.3 Triggering and Data Acquisition (DAQ)

With a Tevatron beam-crossing time of 396 ns, there are roughly 2.5 million possible events every second. Most of these events are due to low-pT , non-diffractive $p\bar{p}$scattering. These type of events have been studied extensively in the past and are not considered a physics priority at DØ . The task remains to identify the interesting events and record them. Identification of these events is performed using a technique known as triggering, which proceeds by matching event properties to a predefined set of patterns which are characteristic of the physics processes of interest. However, physical constraints limit the rate at which events can be triggered and recorded. First, the frequency at which the detector can be read out sets an upper limit on the event examination rate at about 10 kHz. Second, the maximum event processing and storage rate sets an upper limit on the rate of events which are ultimately recorded at about 100 Hz. The DØ detector utilizes a trigger structure comprised of three distinct stages, intuitively referred to as Level 1 (L1), Level 2 (L2), and Level 3 (L3) triggers. Each trigger level is increasingly more refined than the previous, creating a filtering system which maximizes the efficiency for identifying interesting physics events while satisfying the event rate constraint. The structure of this data acquisition path is shown in Figure 3.13. The Level 1 trigger, shown in Figure 3.14, consists of algorithms implemented in the firmware of Field Programmable Gate Arrays (FPGAs).

Condensed information from the calorimeter, preshower, CFT, and muon detectors is processed in parallel to make a preliminary triggering decision about each event. The latency for the L1 trigger is approximately 4.2 s, allowing for a small deadtime compared to the maximum readout rate of the detector of $\sim$ 10 kHz. The output of L1 is used to limit the rate for accepted events to $\sim$ 1.5 kHz. If the Level 1 trigger issues an accept, the Level 2 trigger queues the event for processing. The L2 trigger combines a hardware trigger scheme (as in L1) with a software trigger scheme. Different pieces of information from the subdetectors are correlated to construct basic physics objects (electrons, muons, tracks, jets) and this information is combined to make a global L2 trigger decision, further reducing the event rate to $\sim$ 800 Hz. When the L2 trigger system issues an accept, the

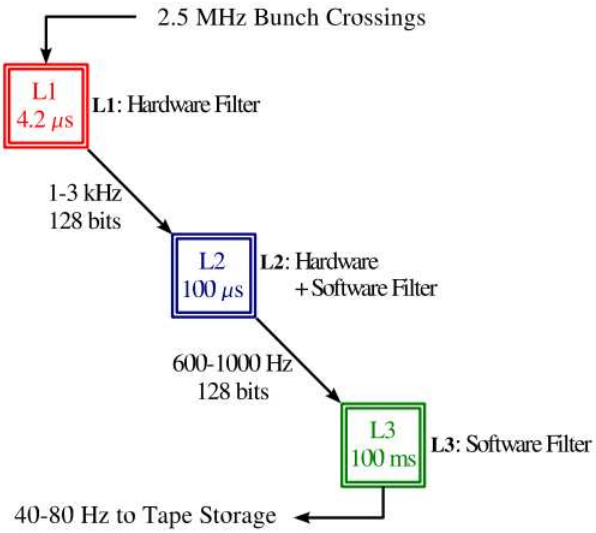

Figure 3.13: The DØ trigger layout and typical trigger rates.

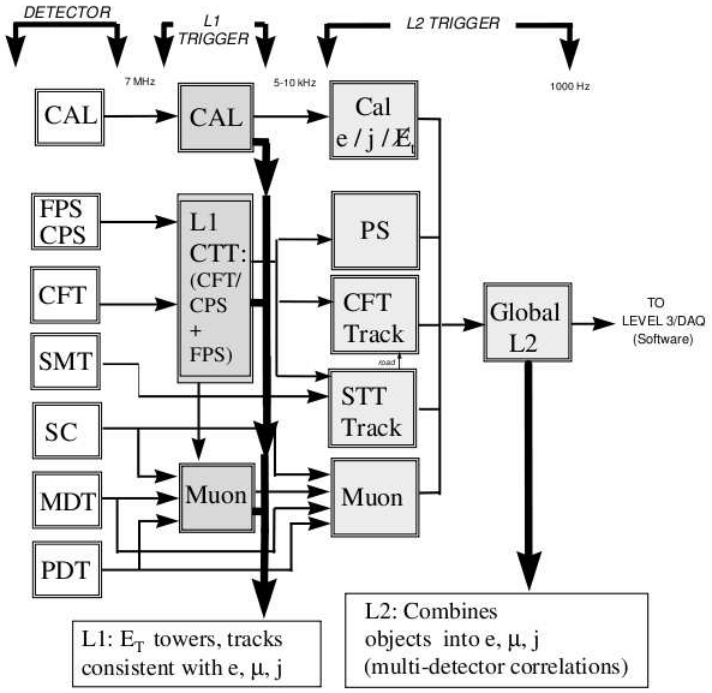

Figure 3.14: The Level 1 and Level 2 trigger data flow paths.

event is passed to the L3/Data Acquisition (DAQ) system. At this point, the full detector information is collected from the subdetector read out crates (ROCs). As shown in Figure 3.15, this event information is then routed to one of $\sim$ 125 Linux PCs in the L3 farm. Each PC processes the data with an identical copy of a filtering software package, reconstructing refined physics objects and applying sophisticated algorithms to arrive at a final trigger decision. Events which recieve a L3 accept are sent to a collection machine and are written to tape for future analysis.

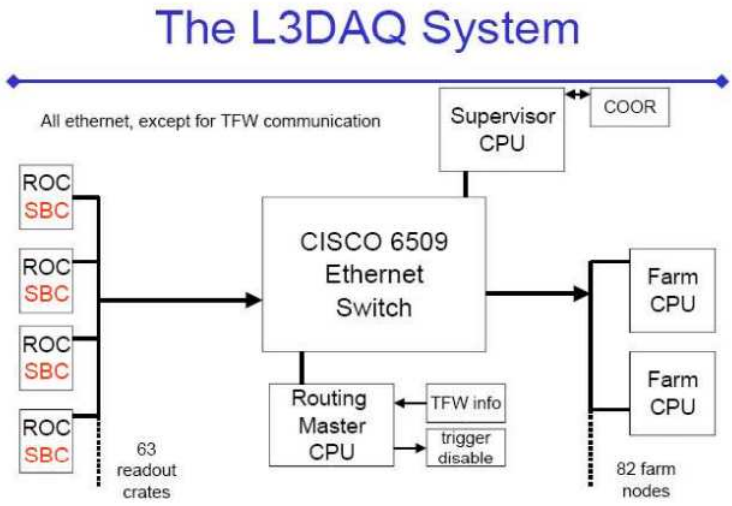

Figure 3.15: The L3 trigger and DAQ system architechture.

3.4 Event Simulation

Computer simulations of both signal and background events are used to model the response of the DØ detector. These Monte Carlo (MC) simulations proceed through a number of different steps which are described below.

3.4.1 Event Generation

"Event generators" which describe the production mechanism at the pp hard scatering level are used to generate simulated events. The typical output is a

list of vertices and particles that were produced at those vertices. The PYTHIA event generator [36] is the most widely used at DØand was used for this analysis. The program generates complete events incorporating our current understanding of the underlying physics. This includes hard and soft sub-processes, parton distribution functions, fragmentation, and decays etc. Monte Carlo techniques are used in addition to properly simulate the quantum mechanical variation between events observed in nature using both average behavior and fluctuations.

While b-hadron decays are created by `PYTHIA`, a program especially tuned for B physics, `EvtGen` XX [37] , is used to simulate the decays of b-hadrons and their daughter particles. Appendix XX lists the EvtGen decay files used for generating the different Monte Carlo samples used in this analysis. The generated events are then filtered using the `d0mess` [1] package [38] and only those events which contain the desired particles satisfying the required kinematic cuts are kept.

3.4.2 Detector Simulation

The output of the event generation step is passed through a full simulation of the DØ detector. This simulation consists of two programs: `DOGSTAR` [39] and `DOSIM` [40]. `DOGSTAR17` is based on the `CERN GEANT` (v3.21) program [41] which describes the true geometry of a detector by building it up from a library of known shapes.

`DOGSTAR` helps trace particles through the DØ detector, determines where their paths intersect active areas, and simulates their energy deposition and secondary interactions. The `DOSIM` program modifies the output of `DGSTAR` in order to account for various detector related effects. It simulates the digitization of analog signals from the detector and converts the simulated data to a form that real data takes when processed through the DØ electronics. It also takes into account various detector inefficiencies and noise from both the detector and the electronics. Additionally, it does pile-up of any additional interactions that might occur in the same bunch crossing as the signal event . Calorimeter pileup which occurs when significant energy is deposited before the energy from the previous bunch crossing has been read out, is also modeled in the program. The output of `DOSIM` is in the same format as the raw data and is passed onto the reconstruction program

[1] Abbreviation for **D**Ø **M**onte Carlo **E**vent **S**election **S**ystem.

DORECO . The format of the DORECO output is identical to that of the data processed offline, but contains additional Monte Carlo information that makes it possible to correlate reconstructed detector data with the original (or "true") generator output.

Chapter 4

Analysis

4.1 Measurement of the $\mathcal{B}\left(\Lambda_b^0 \to \mu^+\mu^-\Lambda^0\right)$

The number of observed Λ_b^0 events in the channel $\Lambda_b^0 \to \mu^+\mu^-\Lambda^0$ is:

$$\begin{aligned} N_{obs}[\Lambda_b \to \mu^+\mu^-\Lambda^0(p\pi^-)] = \quad & N_{produced}[\Lambda_b \to \mu^+\mu^-\Lambda^0(p\pi^-)] \\ & \times\epsilon_R[\Lambda_b \to \mu^+\mu^-\Lambda^0(p\pi^-)] \end{aligned} \tag{4.1}$$

where ϵ_R the corresponding efficiency and acceptance, and the true number of decays produced is given by:

$$\begin{aligned} N_{produced}[\Lambda_b \to \mu^+\mu^-\Lambda^0(p\pi^-)] = \quad & \mathcal{L} \times \sigma(p\overline{p} \to b\overline{b}) \times f(b \to \Lambda_b) \\ & \times\mathcal{B}\left(\Lambda_b \to \mu^+\mu^-\Lambda^0\right) \\ & \times\mathcal{B}\left(\Lambda^0 \to p\pi^-\right) \end{aligned} \tag{4.2}$$

where:

- $\mathcal{L}$ is the total integrated luminosity of the collected data sample,
- $\sigma(p\overline{p} \to b\overline{b})$ the b production cross section,

- $\mathcal{B}\left(\Lambda_b \to \mu^+\mu^-\Lambda^0\right)$ the branching fraction of $\Lambda_b \to \mu^+\mu^-\Lambda^0$
- $\mathcal{B}\left(\Lambda^0 \to p\pi^-\right)$ the branching fraction of $\Lambda^0 \to p\pi^-$

The measurement of the $\mathcal{B}\left(\Lambda_b^0 \to \mu^+\mu^-\Lambda^0\right)$ requires the determination of the integrated luminosity or the normalisation to a similar decay with a known branching fraction. For this search the decay of $\Lambda_b^0 \to J/\psi\Lambda^0$ has been used for normalisation. In necessary to measure the Relative Branching Ratio $\frac{\mathcal{B}\left(\Lambda_b \to \mu^+\mu^-\Lambda^0\right)}{\mathcal{B}(\Lambda_b \to J/\Psi\Lambda^0)}$. In the case of the branching fraction $\Lambda_b^0 \to J/\psi\Lambda^0$, the most recent study was reported by the CDF experiment in 1997 [3], using 110 pb^{-1} of $p\bar{p}$ collision data taken at $\sqrt{s} = 1.8$ TeV, and measuring $f(b \to \Lambda_b) \cdot \mathcal{B}(\Lambda_b^0 \to J/\psi\Lambda^0) = (4.7 \pm 2.3) \times 10^{-5}$, the uncertainties on this branching fraction is $\sim 50\%$. The first step in this analysis was to improve the measurement of the $\mathcal{B}\left(\Lambda_b^0 \to J/\psi\Lambda^0\right)$ and with the new value make an estimation of the upper limit on the branching fraction of $\Lambda_b^0 \to \mu^+\mu^-\Lambda^0$

The study for the $\mathcal{B}(\Lambda_b^0 \to J/\psi\Lambda^0)$ is performed using 6.1 fb^{-1}, and for the $\mathcal{B}(\Lambda_b^0 \to \mu^+\mu^-\Lambda^0)$ was used 8 fb^{-1} of $p\bar{p}$ collisions collected with the DØ detector between 2002–2010 at $\sqrt{s} = 1.96$ TeV at the Fermilab Tevatron Collider.

Details specific to this analysis are discussed in the following sections.

4.1.1 $f(b \to \Lambda_b) \cdot \mathcal{B}\left(\Lambda_b^0 \to J/\psi\Lambda^0\right)$ calculation

The $f(b \to \Lambda_b) \cdot \mathcal{B}\left(\Lambda_b^0 \to J/\psi\Lambda^0\right)$ is calculated by comparing with the well-known and topologically similar decay $B_d^0 \to J/\psi K_s^0$. The calculation proceeds as follows:

The number of observed Λ_b^0 events in the channel $\Lambda_b \to J/\psi(\mu^+\mu^-)\Lambda^0(p\pi^-)$ is:

$$\begin{aligned} N_{obs}[\Lambda_b \to J/\psi(\mu^+\mu^-)\Lambda^0(p\pi^-)] = \quad & N_{produced}[\Lambda_b \to J/\psi(\mu^+\mu^-)\Lambda^0(p\pi^-)] \\ & \times \epsilon_R[\Lambda_b \to J/\psi(\mu^+\mu^-)\Lambda^0(p\pi^-)] \end{aligned} \tag{4.3}$$

where the true number of decays produced is given by:

$$N_{produced}[\Lambda_b \to J/\psi(\mu^+\mu^-)\Lambda^0(p\pi^-)] = \quad \mathcal{L} \cdot \sigma(p\overline{p} \to b\overline{b}) \cdot f(b \to \Lambda_b)$$

$$\times\mathcal{B}\left(\Lambda_b \to J/\psi\Lambda^0\right)\cdot\mathcal{B}\left(J/\psi\to\mu^+\mu^-\right)$$
$$\times\mathcal{B}\left(\Lambda^0\to p\pi^-\right). \quad (4.4)$$

Here $\mathcal{L}$ is the integrated luminosity, $\sigma(p\overline{p}\to b\overline{b})$ is the cross-section for the production of $b\overline{b}$ quarks, $f(b\to\Lambda_b)$ is the $b\to\Lambda_b$ production fraction, and $\mathcal{B}(Z\to XY)$ is the branching fraction for the process $Z\to XY$. The "reconstruction" efficiency $\epsilon_R\left(\Lambda_b\to J/\psi(\mu^+\mu^-)\Lambda^0(p\pi^-)\right)$ encompasses acceptance effects as well as detector, trigger and reconstruction efficiencies for this decay.

Similarly,

$$\begin{aligned} N_{obs}[B^0\to J/\psi(\mu^+\mu^-)K^0_S(\pi^+\pi^-)] = \quad & \mathcal{L}\cdot\sigma(p\overline{p}\to b\overline{b})\cdot f(b\to B^0)\\ & \times\mathcal{B}\left(B^0\to J/\psi K^0_S\right)\cdot\mathcal{B}\left(J/\psi\to\mu^+\mu^-\right)\\ & \times\mathcal{B}\left(K^0_S\to\pi^+\pi^-\right)\\ & \times\epsilon_R[B^0\to J/\psi(\mu^+\mu^-)K^0_S(\pi^+\pi^-)]. \quad (4.5)\end{aligned}$$

Combining these expressions we have:

$$\begin{aligned}\frac{f(b\to\Lambda_b)\cdot\mathcal{B}\left(\Lambda_b\to J/\psi\Lambda^0\right)}{f(b\to B^0)\cdot\mathcal{B}\left(B^0\to J/\psi K^0_S\right)} = \quad & \frac{N_{obs}[\Lambda_b\to J/\psi(\mu^+\mu^-)\Lambda^0(p\pi^-)]}{N_{obs}[B^0\to J/\psi(\mu^+\mu^-)K^0_S(\pi^+\pi^-)]}\times\frac{\mathcal{B}\left(K^0_S\to\pi^+\pi^-\right)}{\mathcal{B}\left(\Lambda^0\to p\pi^-\right)}\\ & \times\frac{\epsilon_R[B^0\to J/\psi(\mu^+\mu^-)K^0_S(\pi^+\pi^-)]}{\epsilon_R[\Lambda_b\to J/\psi(\mu^+\mu^-)\Lambda^0(p\pi^-)].} \quad (4.6)\end{aligned}$$

Therefore, in order to determine the relative branching ratios for these two decays, it is sufficient to count the number of events observed of each type, and to measure the relative efficiencies. Monte Carlo simulation is used to extract these efficiencies, as follows. It is necessary to take into account the kinematic cuts applied at generation level, and also that both Λ^0 and K^0_S were allowed to decay 'naturally' (i.e. according to the decay branching fractions set by the simulation):

$$\begin{aligned}\epsilon_R[\Lambda_b\to J/\psi(\mu^+\mu^-)\Lambda^0(p\pi^-)] = \quad & \frac{1}{\mathcal{B}^{(MC)}\left(\Lambda^0\to p\pi^-\right)}\times\frac{N^{(MC)}_{reco}[\Lambda_b\to J/\psi(\mu^+\mu^-)\Lambda^0(p\pi^-)]}{N^{(no-cuts)}_{gen}[\Lambda_b\to J/\psi(\mu^+\mu^-)\Lambda^0]}\\ = \quad & \frac{1}{\mathcal{B}^{(MC)}\left(\Lambda^0\to p\pi^-\right)}\times\frac{N^{(MC)}_{reco}[\Lambda_b\to J/\psi(\mu^+\mu^-)\Lambda^0(p\pi^-)]}{N_{gen}[\Lambda_b\to J/\psi(\mu^+\mu^-)\Lambda^0]}\end{aligned}$$

$$\times \epsilon^{(cuts)}_{d0\_mess}[\Lambda_b \to J/\psi(\mu^+\mu^-)\Lambda^0]. \quad (4.7)$$

Here $N_{gen}[\Lambda_b \to J/\psi(\mu^+\mu^-)\Lambda^0]$ is the number of MC events generated that passed all our generation level cuts.

Note that $\epsilon^{(cuts)}_{d0\_mess}(\Lambda_b \to J/\psi(\mu^+\mu^-)\Lambda^0)) = \epsilon_{d0\_mess}(b \to \Lambda_b \to J/\psi(\mu^+\mu^-)\Lambda^0)/f^{(MC)}(b \to \Lambda_b)$, where $\epsilon^{(cuts)}_{d0\_mess}$ is the "only cuts" efficiency in `d0_mess` (in our case cuts on p_T and $|\eta|$ for both muons), and ϵ_{d0_mess} is the complete `d0_mess` efficiency, which apart from the kinematic cuts, accounts for the fact that only a fraction $f^{(MC)}(b \to \Lambda_b)$ hadronizes to Λ^0_b in Pythia (remember that $\mathcal{B}(\Lambda^0_b \to J/\psi\ \Lambda^0\ ) = \mathcal{B}(J/\psi \to \mu^+\mu^-) = 1$ and $b\overline{b}$ is forced from Pythia). Understanding this, let us denote

$$\epsilon_{d0\_mess}(\Lambda_b) \equiv \epsilon_{d0\_mess}[b \to \Lambda_b \to J/\psi(\mu^+\mu^-)\Lambda^0]. \quad (4.8)$$

Then

$$\epsilon \equiv \frac{\epsilon_R[B^0 \to J/\psi(\mu^+\mu^-)K^0_S(\pi^+\pi^-)]}{\epsilon_R[\Lambda_b \to J/\psi(\mu^+\mu^-)\Lambda^0(p\pi^-)]} = \frac{N^{(MC)}_{reco}[B^0 \to J/\psi(\mu^+\mu^-)K^0_S(\pi^+\pi^-)]}{N^{(MC)}_{reco}[\Lambda_b \to J/\psi(\mu^+\mu^-)\Lambda^0(p\pi^-)]} \times \frac{N_{gen}[\Lambda_b \to J/\psi(\mu^+\mu^-)\Lambda^0]}{N_{gen}[B^0 \to J/\psi(\mu^+\mu^-)K^0_S]} \times \frac{f^{(MC)}(\Lambda_b)}{f^{(MC)}(B^0)} \times \frac{\epsilon_{d0\_mess}(B^0)}{\epsilon_{d0\_mess}(\Lambda_b)} \times \frac{\mathcal{B}^{(MC)}\left(\Lambda^0 \to p\pi^-\right)}{\mathcal{B}^{(MC)}\left(K^0_s \to \pi^+\pi^-\right)} \quad (4.9)$$

Furthermore,the branching ratios:

$$\mathcal{B}^{(MC)}\left(\Lambda^0 \to p\pi^-\right) = \mathcal{B}\left(\Lambda^0 \to p\pi^-\right) \quad (4.10)$$

$$\mathcal{B}^{(MC)}\left(K^0_S \to \pi^+\pi^-\right) = \mathcal{B}\left(K^0_S \to \pi^+\pi^-\right) \quad (4.11)$$

then the ratio of Eq. (4.6) can be expressed as:

$$v \equiv \frac{f(b \to \Lambda_b) \cdot \mathcal{B}[\Lambda_b \to J/\psi\Lambda^0]}{f(b \to B^0) \cdot \mathcal{B}[B^0 \to J/\psi K^0_S]} = \frac{N_{obs}[\Lambda_b \to J/\psi(\mu^+\mu^-)\Lambda^0(p\pi^-)]}{N_{obs}[B^0 \to J/\psi(\mu^+\mu^-)K^0_S(\pi^+\pi^-)]} \times \frac{N^{(MC)}_{reco}[B^0 \to J/\psi(\mu^+\mu^-)K^0_S(\pi^+\pi^-)]}{N^{(MC)}_{reco}[\Lambda_b \to J/\psi(\mu^+\mu^-)\Lambda^0(p\pi^-)]} \times \frac{N_{gen}[\Lambda_b \to J/\psi(\mu^+\mu^-)\Lambda^0]}{N_{gen}[B^0 \to J/\psi(\mu^+\mu^-)K^0_S]}$$

$$\times \frac{\epsilon_{d0\_mess}(B^0)}{\epsilon_{d0\_mess}(\Lambda_b)} \times \frac{f^{(MC)}(\Lambda_b)}{f^{(MC)}(B^0)}. \qquad (4.12)$$

The different quantities required to perform this determination are extracted as follows:

- N_{obs} is extracted by fitting the appropriate invariant mass distributions in data after applying all selection criteria;
- N_{reco} is extracted from the MC simulated data after applying all selection criteria;
- N_{gen}, ϵ_{d0_mess} and $f^{(MC)}$ are extracted from the MC simulated data, at generation level.

N_{obs}, N_{reco} and N_{gen} are evaluated separately for Λ_b^0 and B_d^0 cases, for Run IIa, Run IIb1 and Run IIb2 data. In the case of ϵ_{d0_mess} and $f^{(MC)}$ will be the same value for all the runs.

Chapter 5

Λ_b^0 and B_d^0 Selection

5.1 Flow of the data

The simulation of physics processes is an important part of this analysis. Simulations of the production, decay and detection of $b\bar{b}$ events is the only way to determine many of the input parameters for this work. A variety of software tools are employed to acquire the simulated data required for these studies.

The $b\bar{b}$ production process is simulated by Pythia XX. In addition, it simulates the hadronization process by which the $b\bar{b}$ pair produce a Λ_b^0 and/or other B hadrons. And as was explained in the previous Chapter, the Monte Carlo (MC) simulations proceed through a number of different steps in order to have an aproximation to the real data of the RUN II. But in both cases, MC and real data, we apply the same reconstruction algorithms and selection analysis. The different steps for MC and real data are showed in the Fig. 5.1

With Monte Carlo is possible to know with good precision the numbers of events generated, the events that pass the `d0_mess` filter and the numbers of events reconstructed that pass through our entire reconstruction and final selection.

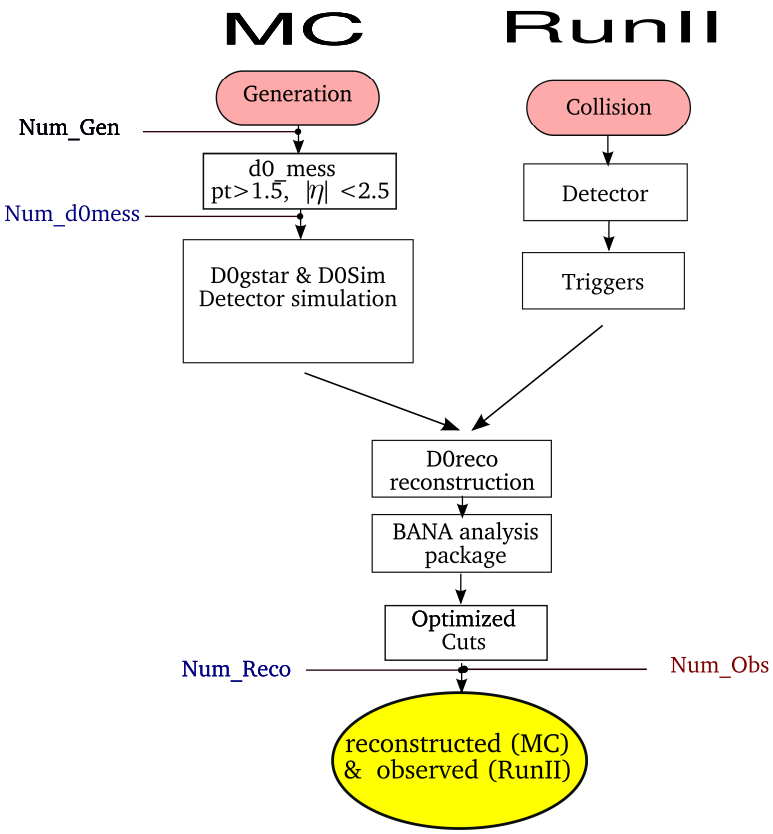

Figure 5.1: Diagram of the data seleccion for MC and RunII

5.2 MC Samples for the selection cuts

Two MC samples were generated to be use on the optimization of selection criteria, which will be described later in this note. Information on these MC samples is shown in Table II, with additional details given in Appendix A. These samples of Monte Carlo will not be used for computing reconstruction efficiencies

Here, charge conjugate decays are implied. Again, generation level constraints are applied to the muons using D0Mess:

- $p_T(\mu^{\pm}) > 1.0$ GeV/c
- $|\eta(\mu^{\pm})| < 2.5$

Table 5.1: MC signal used

Decay	Version	Sample Size	Req ID
$\Lambda_b^0 \to J/\psi\Lambda^0$	p17.09.08	$\sim$ 600 K	126235, 126236, 126237
	p20.09.03	$\sim$ 600 K	126238, 126239, 126240
	p20.09.03/p20.15.04	$\sim$ 600 K	124618,124619,124620
$B_d^0 \to J/\psi K_s^0$	p17.09.08	$\sim$ 600 K	126252, 126253, 126254
	p20.09.03	$\sim$ 600 K	126255, 126256, 126257
	p20.09.03/p20.15.04	$\sim$ 600 K	126258, 126259, 126260

5.3 Data samples

The analysis presented here is based on data collected by the D0 Detector between April 2002 and June 2009:

- Run IIa: April 20, 2002 - February 22, 2006 (runs 151,817-215,670)
- Run IIb-1: June 9, 2006 - August 4, 2007 (runs 221,698-234,913)
- Run IIb-2: October 28, 2007 - June 13, 2009 (runs 237,342-252,918)

We use the single muon data skims, produced from the thumbnails, and converted into a streamlined b-physics file format ("AADST") REF.

5.3.1 Event Selection Overview

In order to search for $\Lambda_b^0 \to J/\psi\Lambda^0$ and $B_d^0 \to J/\psi K_s^0$ decays, we begin by selecting events which contains a pair of muons passing some quality criteria (described in next subsection). Next, a preliminary selection of $\Lambda_b^0 \to J/\psi\Lambda^0$ and $B_d^0 \to J/\psi K_s^0$ events is made, by combining the dimuon system with a pair of tracks (Λ^0 and K_s^0 candidates, respectively) which form a common vertex and pass additional requirements. The decay channels are illustrated schematically in Fig. 5.2, and the selection criteria are described in detail below.

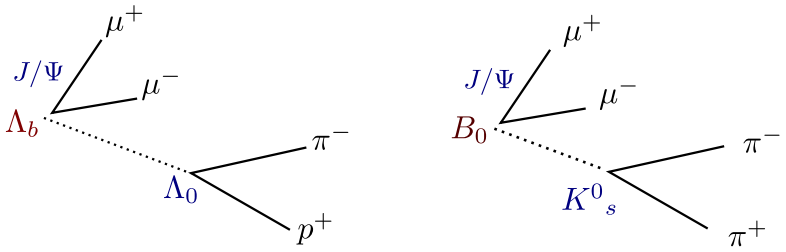

Figure 5.2: Decays

5.3.2 Muon Quality Definitions

Reconstructed muon candidates are classified using two parameters: muon type and muon quality. See Ref [**?** **?**] for details.

- The type of muon is given by the parameter nseg. In this analysis just the nseg=0,1,3 were used. The particularity of each value is the next:
  - $nseg = 0$, central track only
  - $nseg = 1$, central track + inner segment of system muon only
  - $nseg = 2$, central track + outer segment of system muon only
  - $nseg = 3$, central track + (outer + inner) segments of system muon
- The muon quality can be Loose, Medium or Tight, each one describe increasingly more stringent requirements for identifying an Muon .

5.3.3 Dimuon Sample

The first sample for this analysis is the selection of dimuon candidates using the BANA *JPsiFinder* package. Candidates are reconstructed using two tracks of opposite charge, with $p_T > 1.0$ GeV/c, and identified as muons by the muon system. Both tracks must have at least one hit in the CFT detector. At least one of the muons must have nseg = 3. For muons with nseg > 0, the additional criterion $p_T > 1.5$ GeV/c is applied. In cases where the second muon has nseg = 0, extra selection criteria are applied:

- The total momentum of the dimuon candidate must fulfill $p_{Tot}^{\mu\mu} < 7.0$ GeV/c;

- The matching between the local muon object and the central track must fulfill $\chi^2 < 25$ for both muons;
- The second muon must have $p_T > 2.5$ GeV/c;
- For muons identified by the calorimeter, nmtc() >= 0 (see MuonParticle-class), and CalEsig() > 0.015*CalNLayer().

Following this initial selection, additional quality cuts are applied:

- One muon is required be TIGHT and the other at least LOOSE;
- For both muons:
  - Candidates which only have reconstructed segments outside the toroid (nseg=2) are rejected;
  - $p_T(\mu) > 2$ GeV/c;
  - $|\eta(\mu)| < 2$;
  - The number of hits in the SMT must exceed $N_{smt} \geq 2$;
  - The number of hits in the CFT must exceed $N_{cft} \geq 2$.

Figure 5.3 shows the dimuon invariant mass distributions for the three running epochs, after application of the above constraints.

5.3.3.1 Preselection

For those events containing a J/Ψ candidate, the J/Ψ mass is required to be within the range 2.7-3.5GeV/c^2, passing the above criteria Λ^0 and K^0_S candidates are next selected. This is performed by combining pairs of oppositely-charged central tracks, which form a vertex satisfying the goodness-of-fit requirement $\chi^2 < 36$. No more than two hits in the detector between the primary and secondary vertex (Λ^0 or K^0_S vertex) are allowed, and a limited number of missed hits (< 5) are allowed downstream of the secondary vertex position. Each track must also be associated with at least one hit in the CFT system.

In the case of Λ^0 , for the computation of the invariant mass M($p\pi$), the track with the highest momentum is assumed to be the proton, and masses are

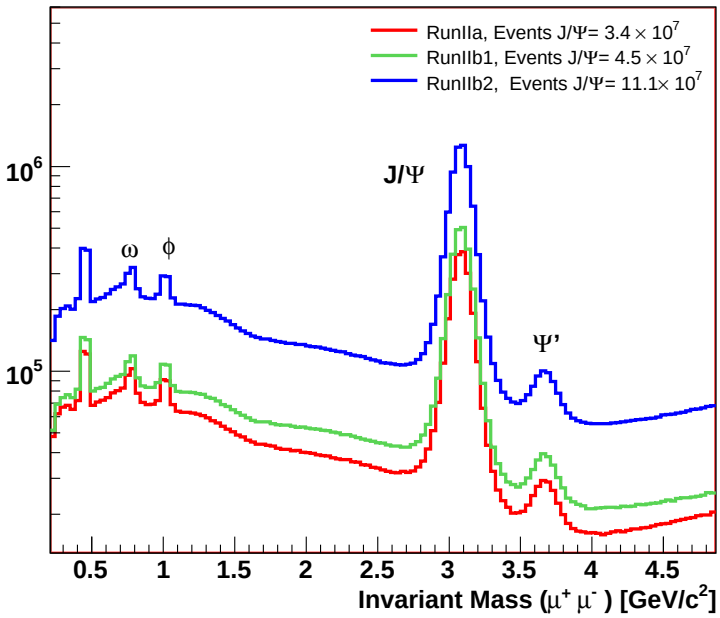

Figure 5.3: Mass distributions for dimuons in RunIIa, RunIIb1 and RunIIb2

allocated accordingly. For the K_S^0 case, the two tracks were assumed to be $\pi^+\pi^-$. Finally, $\Lambda_b^0 \to J/\psi\Lambda^0$ and $B_d^0 \to J/\psi K_s^0$ candidates are reconstructed by combining the dimuon system with the Λ^0 and K_S^0 candidates, respectively. To limit combinatorial backgrounds additional criteria are applied:

- $p_T(\Lambda_b) > 5$ GeV/c or $p_T(B_0) > 5$ GeV/c
- $p_T(J/\psi) > 3$ GeV/c
- $Collinearity(\Lambda^0) > 0.999$ or $Collinearity(K_s^0) > 0.999$

We require the cosine of the angle between the p_T vector of the Λ^0 and the vector in the perpendicular plane from the J/Ψ vertex to the Λ^0 decay vertex to be larger than 0.999, this quantity is called *Collinearity* . For Λ^0 's that decay from $\Lambda_b^0 \to J/\psi\Lambda^0$ the cosine of this angle is very close to 1. The K_S^0 selection follows the same criteria. Figure 5.4 shows the collinearity of Λ^0 .

Figure 5.5 shows the invariant mass distributions for K_S^0 and Λ^0 after application of all preselection constraints.

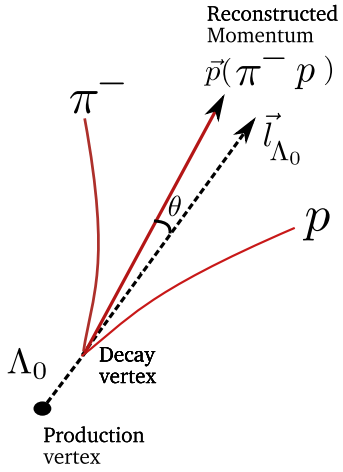

Figure 5.4: Collinearity angle. Here PV denotes the J/ψ vertex.

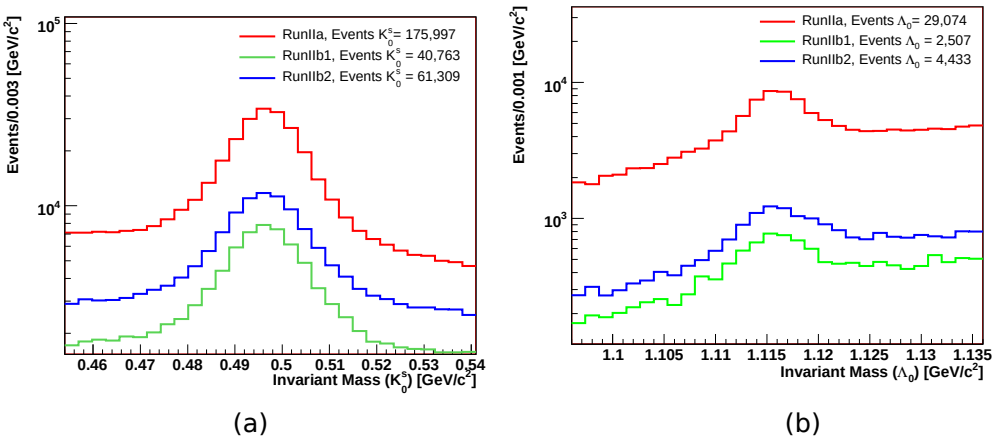

Figure 5.5: Mass distributions in the RunIIa, RunIIb1 and RunIIb2 for a) K^0_S and b) Λ^0

Figure 5.6 shows the invariant mass distributions for $B^0_d \to J/\psi K^0_s$ and $\Lambda^0_b \to J/\psi \Lambda^0$ after application of all preselection constraints. The mass range for $\Lambda^0_b \to J/\psi \Lambda^0$ is 4.5 GeV/c^2 to 6.7 GeV/c^2 and for $B^0_d \to J/\psi K^0_s$ is 4.3 GeV/c^2 to 6.5 GeV/c^2.

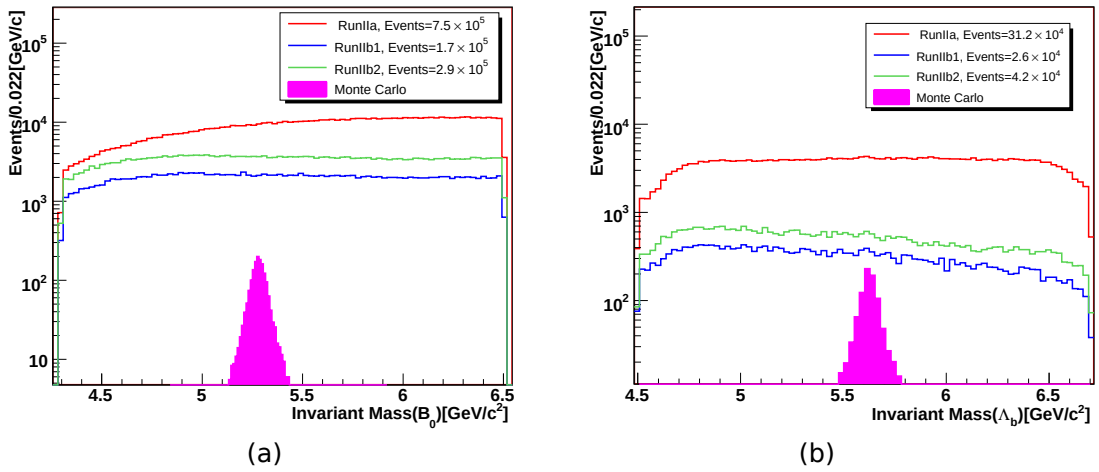

Figure 5.6: Mass distributions in the RunIIa, RunIIb1 and RunIIb2 for a) $B_d^0 \to J/\psi K_s^0$ and b) $\Lambda_b^0 \to J/\psi \Lambda^0$

5.4 Optimization

For the choise of the final selection criteria, we optimize

$$S = \frac{N_s}{\sqrt{N_s + N_b}} \tag{5.1}$$

where N_s and N_b are the number of signal and background candidates, respectively, by using Monte Carlo estimates for N_s and data for N_b.

The optimization procedure is done using a grid on the possible values of selected variables for signal optimization.

The Monte Carlo sample described in the Section II-B is used to model the signal. The mass range is taken from $\mu \pm 3\sigma$. The background events are taken from the mass sidebands of Λ_b^0 and B_d^0 candidates in real data, from $(\mu - 10\sigma$, $\mu - 4\sigma)$ and $(\mu + 4\sigma, \mu + 10\sigma)$.

N_s is the number of signal events that remain after applying these cuts on the Monte Carlo sample. In the same way N_b is the number of background events that remain after applying the same set of cuts.

5.5 Monte Carlo Samples

5.5.1 $\Lambda_b^0 \to J/\psi\Lambda^0$ and $B_d^0 \to J/\psi K_s^0$

As it was mentioned before, in order to select the final cuts for the search of$\Lambda_b^0 \to J/\psi\Lambda^0$ and $B_d^0 \to J/\psi K_s^0$ decays, we will use MC signal and background from sidabands data. To select the mass windows to be use from the sidebands, as well as the mass windows of Λ^0 and K_S^0 signals, several samples of MC data are used to extract the signal widths as a first approximation to what would be expected on data (in general the selected width in MC is few MeV wider than observed in data). Invariant mass distributions for the three particles are fitted with a Gaussian function, and the mean μ and width σ are extracted from the fit. The limits on the mass window for each distribution are then defined by $\mu \pm 3\sigma$, where σ is taken to be the largest value obtained from fits over the three epochs. This information will be used to define the limits on the signal and background in the next section 5.6.1, As indicated before, the sidebands will be defined as the windows $(\mu - 10\sigma,\ \mu - 4\sigma)$ and $(\mu + 4\sigma,\ \mu + 10\sigma)$. Also to define the limits to remove background coming from the misidentified Λ^0 and K_S^0 5.7.

Figures 5.7–5.8 and Table 5.2 show the results of these mass distribution fits for $\Lambda_b^0 \to J/\psi\Lambda^0$ and $B_d^0 \to J/\psi K_s^0$, over the three epochs. While the same number of events are generated for each epoch, there is a significant reduction on the reconstruction efficiency over time, and also a slight increase in the widths, expected as a consequence of detector ageing. A similar degredation in the real data is expected.

The mass distributions for both signal (Monte Carlo) and background (data sidebands) for the two channels are shown in Fig. 5.9, for Run IIa data. Similar distributions are observed for Run IIb1 and Run IIb2.

5.6 Final Selection Cuts

5.6.1 Variables selected for significance optimization

Table 5.3 shows the parameters chosen for the selection of final cuts and the values of each parameter found after the significance optimization. The values

Table 5.2: Limits for Mass Distributions in Monte Carlo

Particle	Minimum [GeV/c^2]	Maximum [GeV/c^2]	RunIIa [GeV/c^2]		RunIIb1 [GeV/c^2]		RunIIb2 [GeV/c^2]	
			μ	σ	μ	σ	μ	σ
Λ_b^0	5.475	5.787	5.625 ± 0.0010	0.040 ± 0.0010	5.624 ± 0.0025	0.052 ± 0.0028	5.636 ± 0.0021	0.062 ± 0.0056
B_d^0	5.016	5.541	5.280 ± 0.0007	0.037 ± 0.0007	5.279 ± 0.0010	0.036 ± 0.0009	5.282 ± 0.0018	0.043 ± 0.0014
Λ^0	1.105	1.127	1.116 ± 0.0001	0.0031 ± 0.0001	1.116 ± 0.0001	0.0036 ± 0.0001	1.116 ± 0.0001	0.0034 ± 0.0001
K_S^0	0.474	0.521	0.498 ± 0.0002	0.008 ± 0.0002	0.498 ± 0.0002	0.008 ± 0.0002	0.498 ± 0.0004	0.010 ± 0.0004
J/ψ	2.914	3.274	3.094 ± 0.002	0.06067 ± 0.002	3.094 ± 0.003	0.0595 ± 0.002	3.095 ± 0.004	0.0546 ± 0.003

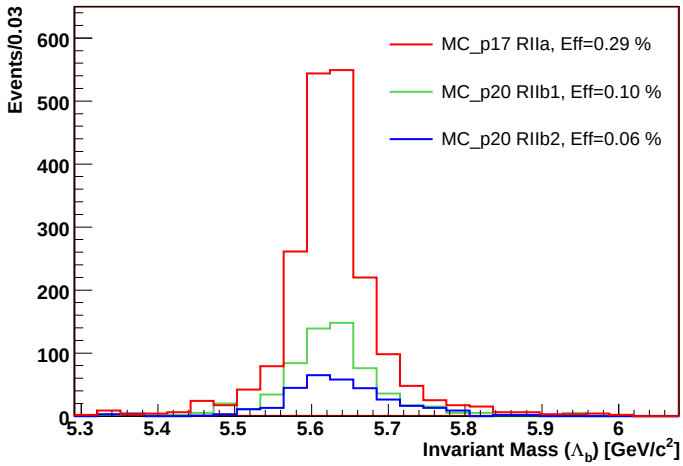

Figure 5.7: Invariant mass for $\Lambda_b^0 \to J/\psi\Lambda^0$ in Monte Carlo P17-RunIIa, P20-RunIIb1 and P20-RunIIb2. Monte Carlo sample described in the Section II-B

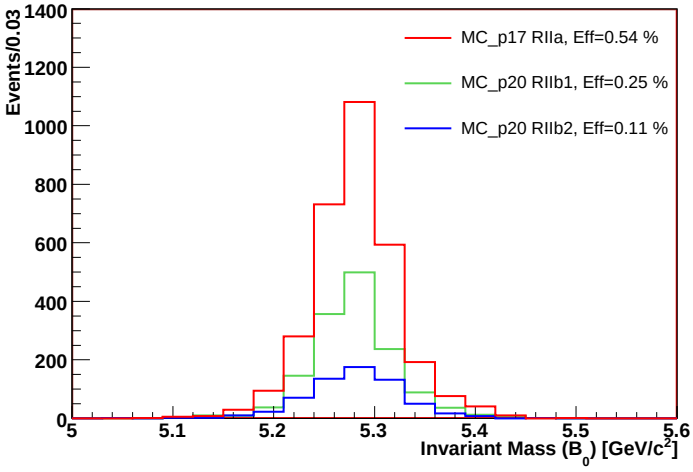

Figure 5.8: Invariant mass for $B_d^0 \to J/\psi K_s^0$ in Monte Carlo P17-RunIIa, P20-RunIIb1 and P20-RunIIb2. Monte Carlo sample described in the Section II-B

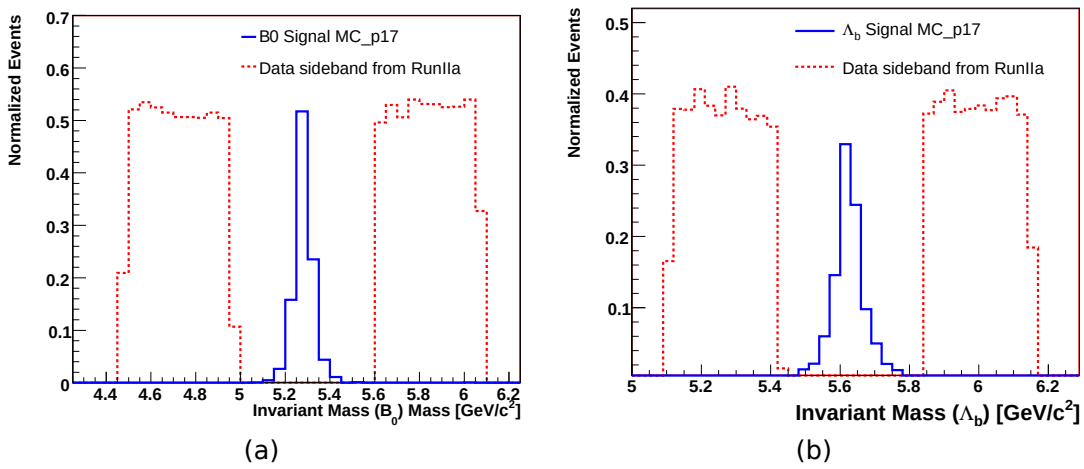

Figure 5.9: Signal and Background samples for $\Lambda_b^0 \to J/\psi\Lambda^0$ and $B_d^0 \to J/\psi K_s^0$ channels, used to determine the selection cuts for Run IIa data.

found for each epoch are similar, therefore a single cut value will be applied to all data the selection criteria. In cases where differences are found between epochs, the procedure is to use the loosest cut. The distributions of each variable, for Run IIa signal and background samples, are shown in Fig. 5.10 ($\Lambda_b^0 \to J/\psi\Lambda^0$) and Fig. 5.11 ($B_d^0 \to J/\psi K_s^0$) respectively.

5.7 Fake Λ^0 and K_S^0

The *Armenteros–Podolanski* [**?**] technique is used to classify the V0-particles and is a convenient way of displaying (identifying). In this analisys we only use this technique to check is we have removed background coming from the misidentified Λ^0 and K_S^0 .

This technique is a very useful method to analyze the decay of a parent particle into two tracks with opposite charges, when direct particle identification is not available. For each two-track event, a point is allocated on the two-dimensional plane defined by the two parameters q_T and α. Here, q_T is the transverse component of the two-track system's momentum with respect to the direction of the

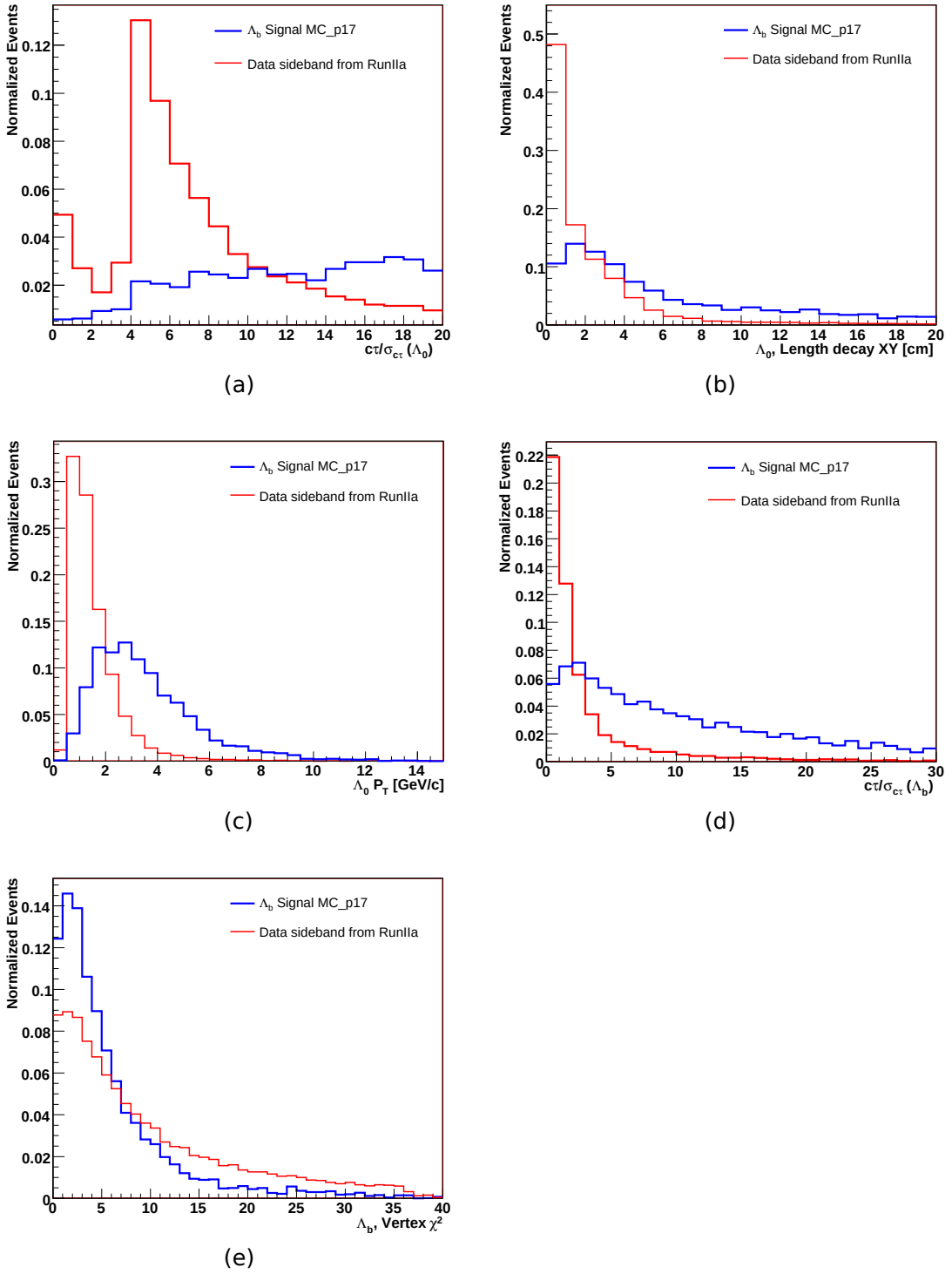

Figure 5.10: Comparation between $\Lambda_b^0 \to J/\psi\Lambda^0$ signal and background distributions for the selection variables for Run IIa

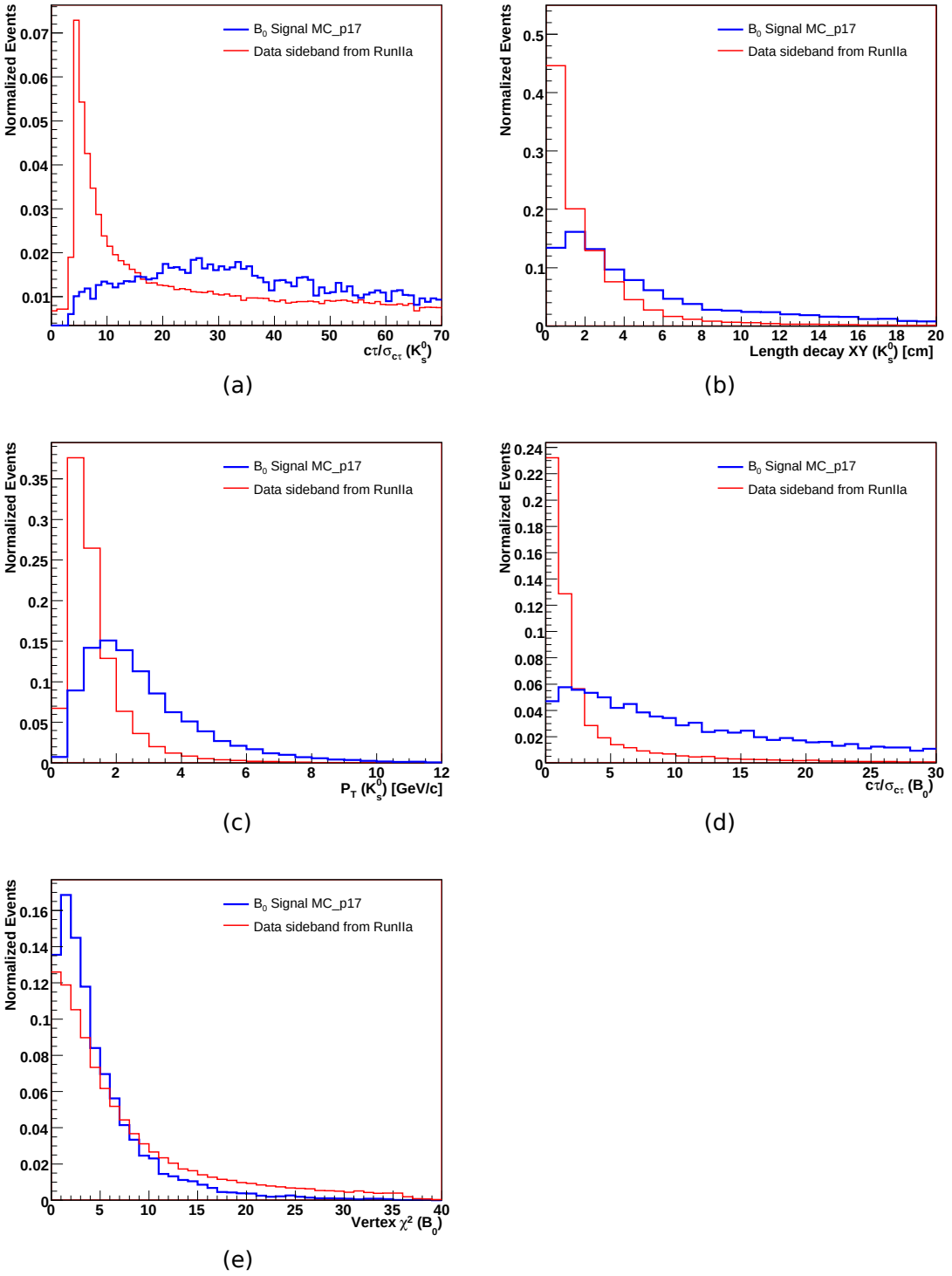

Figure 5.11: Comparation between $B_d^0 \to J/\psi K_s^0$ signal and background distributions for the selection variables for Run IIa

Table 5.3: Results from the optimization. In the Column of Final Cut Value are showed the selected cuts.

Decay	Parameter	Final Cut Value
$\Lambda_b^0 \to J/\psi\Lambda^0$	$c\tau/\sigma_{c\tau}$ (Λ^0)	> 4
	Length Decay XY (Λ^0)	> 0.8
	P_T (Λ^0)	> 1.6
	$c\tau/\sigma_{c\tau}$ (Λ_b^0)	> 2
	χ^2 (Λ_b^0)	< 20
$B_d^0 \to J/\psi K_s^0$	$c\tau/\sigma_{c\tau}$ (K_S^0)	> 9
	Length Decay XY (K_S^0)	> 0.4
	P_T (K_S^0)	> 1
	$c\tau/\sigma_{c\tau}$ (B_d^0)	> 3
	χ^2 (B_d^0)	< 14

parent particle, and α is defined as

$$\alpha = \frac{{q^+}_L - {q^-}_L}{{q^+}_L + {q^-}_L} \tag{5.2}$$

where ${q^+}_L$ and ${q^-}_L$ are the momentum components of the positive and negative tracks along the direction of the parent particle. Both these variables (α and q_T) are obtained from the measured momenta, and do not depend on the particle mass assignment. Figure 5.12 illustrates these varous momentum components graphically.

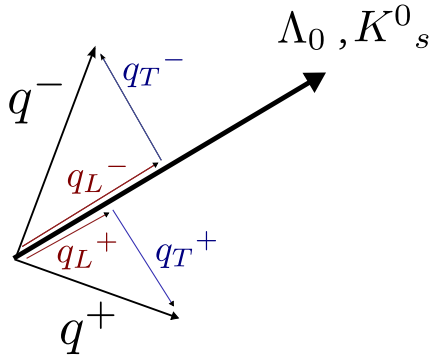

Figure 5.12: Armentaros diagram

Events from a definite decay will be concentrated around an elliptic locus, whose semi–axes and horizontal (α) position depend on the masses of the parent, in this case K^0_S or Λ^0 .

The (α, q_T) *Armenteros–Podolanski* scatter plots for Λ^0 and K^0_S candidates are shown in Fig. 5.13, using Run IIa Monte Carlo simulation of $\Lambda^0_b \to J/\psi\Lambda^0$ and $B^0_d \to J/\psi K^0_s$ channels respectively. The red points are $p^+ + \pi^-$ events, while the corresponding points for the $\pi^- + \pi^+$ events are shown in black. As is clear from the figure, there are two zones where Λ^0 and K^0_S candidates can be misidentified as each other. Additional selection requirements are therefore applied to prevent such mis-identification, as described below.

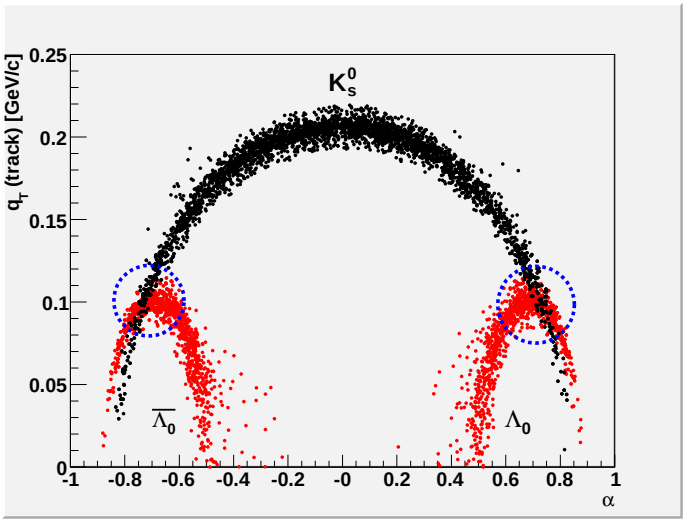

Figure 5.13: Podalski-Armenteros scatter plots for the MC p17 samples of $\Lambda^0_b \to J/\psi\Lambda^0$ and $B^0_d \to J/\psi K^0_s$ decays.

- Λ^0 candidates are removed from the sample if the two tracks have an invariant mass within the K^0_S mass window ($\mu \pm 3\sigma$) when the tracks are both assigned the charged pion mass. i.e. we require either one of the following conditions:
  - Invariant Mass (K^0_S hypothesis) < 0.474 GeV/c^2
  - Invariant Mass (K^0_S hypothesis) > 0.521 GeV/c^2

- Similarly, K_S^0 candidates are removed from the sample if the two tracks have an invariant mass within the Λ^0 mass window ($\mu \pm 3\sigma$) when the leading (trailing) track is assigned the proton (pion) mass. i.e. we require either one of the following conditions:
  - Invariant Mass (Λ^0 hypothesis) < 1.105 GeV/c^2
  - Invariant Mass (Λ^0 hypothesis) > 1.127 GeV/c^2

Having imposed these additional constraints, the resulting *Armenteros–Podolanski* scatter plots for the two channels can be seen in Fig. 5.14. It is clear that ambiguous events, which would be candidates for mis-identification, have been removed.

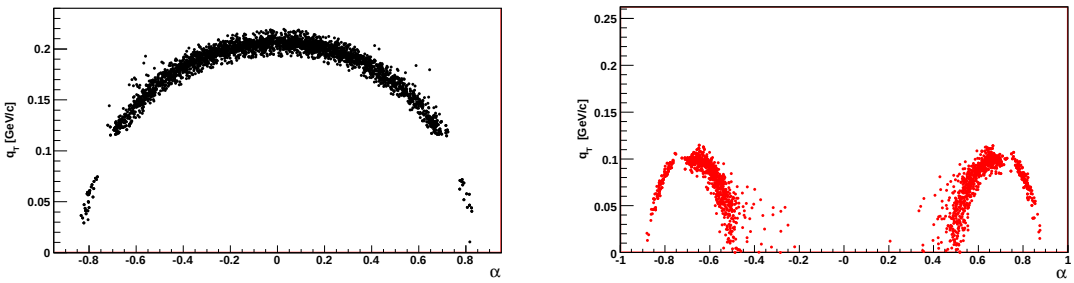

Figure 5.14: Podalski-Armenteros for the MC p17 samples in a) $B_d^0 \to J/\psi K_s^0$ and b) $\Lambda_b^0 \to J/\psi \Lambda^0$ decays, following the application of criteria designed to avoid mis-identification as described in the text.

5.8 Bad runs

Bad runs are removed from our selection. We define a "bad run" as one for which quality, according to the D0 data quality database, is bad, special or unknown in the CFT, SMT or Muon systems. The list of runs excluded for data quality reasons can be found in Ref. [**?**].

5.9 Reconstructed data

After finalizing the optimized set of analysis cuts, and the additional criteria to remove mis-identified particles and bad runs, these cuts are applied on data and MC samples. In addition, we select only one $\Lambda_b^0 \to J/\psi\Lambda^0$ and $B_d^0 \to J/\psi K_s^0$ candidate per event by choosing the one with best vertex χ^2.

The invariant mass distributions, and the corresponding fits to the data, for both real data and Monte Carlo, are shown in Fig. 5.15 ($\Lambda_b^0 \to J/\psi\Lambda^0$) and Fig. **??** ($B_d^0 \to J/\psi K_s^0$). The number of observed candidates are extracted from the fits in each case. Our nominal fitting model is a double Gaussian for the signal peak in both cases real data and Monte Carlo, for background a second order polynomial function is fitted in the case of real data and a linear function in the case of Monte Carlo. The Monte Carlo sample used in this part was described in the Section II-A.

5.9.1 Calculation of the parameter v

Using Pythia and `d0_mess` we generate 3 million Λ_b^0 and 3 million B_d^0 events. From these samples, the following production fractions are measured:

$$f^{(MC)}(B^0) = 0.3962 \pm 0.0001 \tag{5.3}$$

$$f^{(MC)}(\Lambda_b) = 0.0785 \pm 0.0001 \tag{5.4}$$

In the same way for `d0_mess` efficiencies, but now with the their decay products $\Lambda_b^0 \to J/\psi\Lambda^0$ and $B_d^0 \to J/\psi K_s^0$

$$\epsilon_{d0\_mess}(B^0) = 0.0666 \pm 0.0001 \tag{5.5}$$

$$\epsilon_{d0\_mess}(\Lambda_b) = 0.0130 \pm 0.0001 \tag{5.6}$$

We use this d0mess efficiency (same value) for IIa, IIb1 and IIb2.

The number of generated decays of each type is:

1. Run IIa:

$$N_{gen}\left(B^0 \to J/\psi(\mu^+\mu^-)K_S^0\right) = 806,749 \tag{5.7}$$

$$N_{gen}\left(\Lambda_b \to J/\psi(\mu^+\mu^-)\Lambda^0\right) = 725,591 \tag{5.8}$$

2. Run IIb1:

$$N_{gen}\left(B^0 \to J/\psi(\mu^+\mu^-)K_S^0\right) = 807,249 \tag{5.9}$$
$$N_{gen}\left(\Lambda_b \to J/\psi(\mu^+\mu^-)\Lambda^0\right) = 772,203 \tag{5.10}$$

3. Run IIb2:

$$N_{gen}\left(B^0 \to J/\psi(\mu^+\mu^-)K_S^0\right) = 582,896 \tag{5.11}$$
$$N_{gen}\left(\Lambda_b \to J/\psi(\mu^+\mu^-)\Lambda^0\right) = 764,817 \tag{5.12}$$

After reconstructing data and MC we have

1. Run IIa:

$$N_{reco}^{(MC)}\left(B^0 \to J/\psi(\mu^+\mu^-)K_S^0(\pi^+\pi^-)\right) = \quad 5,413 \pm 73 \tag{5.13}$$
$$N_{reco}^{(MC)}\left(\Lambda_b \to J/\psi(\mu^+\mu^-)\Lambda^0(p\pi^-)\right) = \quad 1,985 \pm 44 \tag{5.14}$$
$$N_{obs}\left(B^0 \to J/\psi(\mu^+\mu^-)K_S^0(\pi^+\pi^-)\right) = \quad 1008 \pm 49 \tag{5.15}$$
$$N_{obs}\left(\Lambda_b \to J/\psi(\mu^+\mu^-)\Lambda^0(p\pi^-)\right) = \quad 135 \pm 18 \tag{5.16}$$

Then from Eq. (4.12):

$$v = 0.333 \pm 0.048 \tag{5.17}$$

2. Run IIb1:

$$N_{reco}^{(MC)}\left(B^0 \to J/\psi(\mu^+\mu^-)K_S^0(\pi^+\pi^-)\right) = \quad 3,167 \pm 56 \tag{5.18}$$
$$N_{reco}^{(MC)}\left(\Lambda_b \to J/\psi(\mu^+\mu^-)\Lambda^0(p\pi^-)\right) = \quad 1,073 \pm 33 \tag{5.19}$$
$$N_{obs}\left(B^0 \to J/\psi(\mu^+\mu^-)K_S^0(\pi^+\pi^-)\right) = \quad 535 \pm 37 \tag{5.20}$$
$$N_{obs}\left(\Lambda_b \to J/\psi(\mu^+\mu^-)\Lambda^0(p\pi^-)\right) = \quad 60 \pm 13 \tag{5.21}$$

Then:

$$v = 0.321 \pm 0.074 \tag{5.22}$$

3. Run IIb2:

$$N_{reco}^{(MC)}\left(B^0 \to J/\psi(\mu^+\mu^-)K_S^0(\pi^+\pi^-)\right) = \quad 931 \pm 31 \tag{5.23}$$
$$N_{reco}^{(MC)}\left(\Lambda_b \to J/\psi(\mu^+\mu^-)\Lambda^0(p\pi^-)\right) = \quad 520 \pm 23 \tag{5.24}$$
$$N_{obs}\left(B^0 \to J/\psi(\mu^+\mu^-)K_S^0(\pi^+\pi^-)\right) = \quad 773 \pm 38 \tag{5.25}$$
$$N_{obs}\left(\Lambda_b \to J/\psi(\mu^+\mu^-)\Lambda^0(p\pi^-)\right) = \quad 114 \pm 19 \tag{5.26}$$

Then:

$$v = 0.351 \pm 0.063 \tag{5.27}$$

The results for the three epochs are summarised in Table 5.4, and illustrated graphically in Fig. 5.16; excellent agreement is observed.

Table 5.4: Summary of the parameter v for the three running epochs.

Run	$v + \Delta v$
RunIIa	0.333 ± 0.048
RunIIb1	0.321 ± 0.074
RunIIb2	0.351 ± 0.063

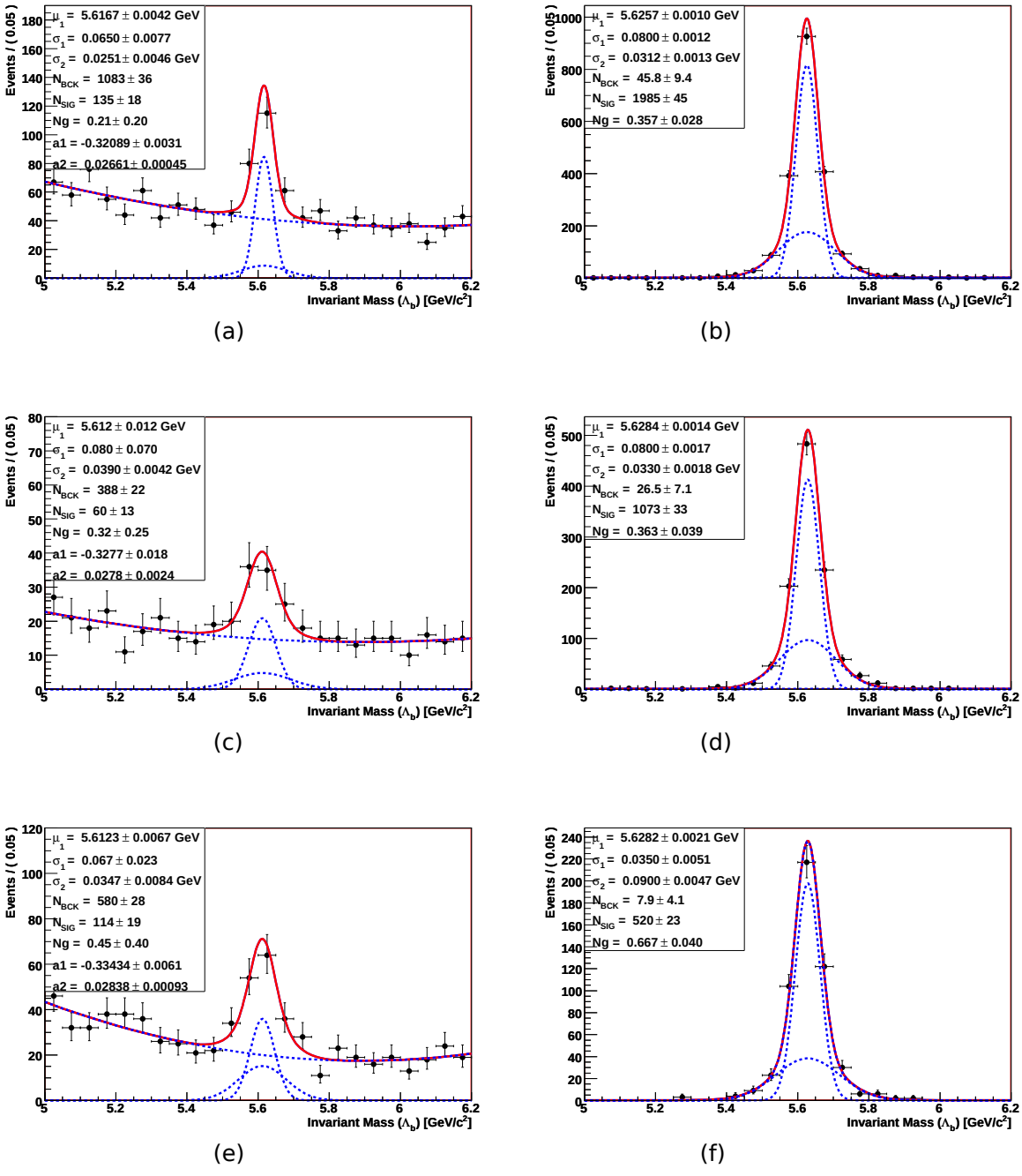

Figure 5.15: Events observed from the decay $\Lambda_b^0 \to J/\psi\Lambda^0$ in *a*) Run IIa data, *b*) Run IIa MC; *c*) Run IIb1 data, *d*) Run IIb1 MC; *d*) Run IIb2 data, *e*) Run IIb2 MC;

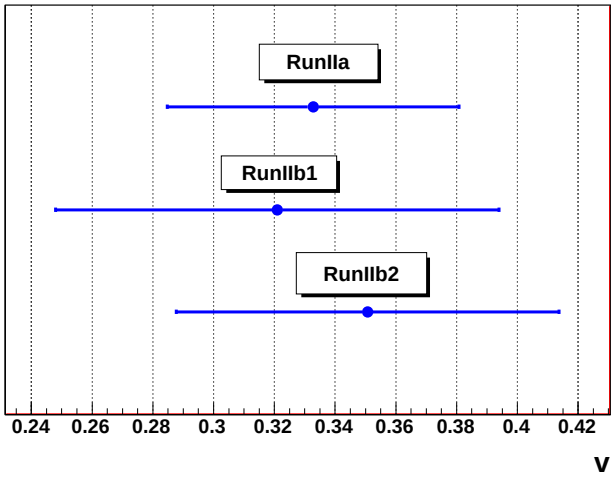

Figure 5.16: Comparation of the measured value of v for different data taken periods.

Chapter 6

Measurement of the $\mathcal{B}\left(\Lambda_b^0 \to J/\psi\Lambda^0\right)$

6.1 Combining data taken periods

From eqs. 4.9 and 4.12 we have:

$$v = \frac{f(b \to \Lambda_b) \cdot \mathcal{B}(\Lambda_b \to J/\psi\Lambda)}{f(b \to B^0) \cdot \mathcal{B}(B^0 \to J/\psi K_s^0)} = \epsilon \cdot \frac{N_{\Lambda_b \to J/\psi\Lambda}}{N_{B^0 \to J/\psi K_S^0}} \cdot \frac{\mathcal{B}(K_s^0 \to \pi^+\pi^-)}{\mathcal{B}(\Lambda \to p\pi^-)} \tag{6.1}$$

where ϵ is the ratio of efficiencies $\frac{\epsilon_{B^0 \to J/\psi K_S^0}}{\epsilon_{\Lambda_b \to J/\psi\Lambda}}$, and as we mentioned before, this value is obtained by:

$$\epsilon = \frac{N_{\Lambda_b}^{MCgen}}{N_{B^0}^{MCgen}} \cdot \frac{N_{B^0}^{MCreco}}{N_{\Lambda_b}^{MCreco}} \cdot \frac{\epsilon_{B^0}^{d0mess}}{\epsilon_{\Lambda_b}^{d0mess}} \cdot \frac{f^{(MC)}(b \to \Lambda_b)}{f^{(MC)}(b \to B^0)} \cdot \frac{\mathcal{B}(\Lambda \to p\pi^-)}{\mathcal{B}(K_s^0 \to \pi^+\pi^-)} \tag{6.2}$$

using this equation and the numbers reported in the previos section, plus $\mathcal{B}(\Lambda \to p\pi^-) = 0.639$ and $\mathcal{B}(K_s^0 \to \pi^+\pi^-) = 0.6920$ (these values are fixed in our generators), the results for the three epochs are summarised in Table 6.1

We can obtain an average efficiency for the three data taken periods by a $\chi^2 = \sum_{i=1}^{3} \frac{\epsilon_i - \overline{\epsilon}}{\sigma_i^2}$ fit which lead us to a weighted average:

$$\overline{\epsilon} = \frac{\sum_{i=1}^{3} \frac{\epsilon_i}{\sigma_i^2}}{\sum_{i=1}^{3} \frac{1}{\sigma_i^2}} \tag{6.3}$$

Table 6.1: Summary of the parameter ϵ for the three running epochs.

Run	$\epsilon + \Delta\epsilon$
RunIIa	2.299 ± 0.061
RunIIb1	2.646 ± 0.094
RunIIb2	2.202 ± 0.122

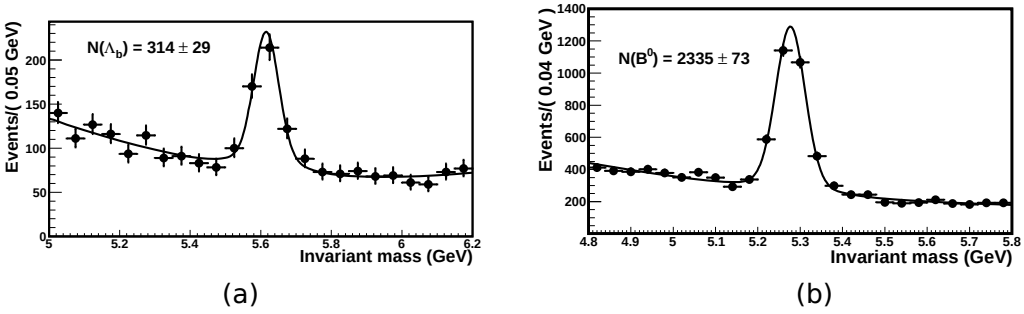

Figure 6.1: Invariant mass distribution in data for $\Lambda_b \to J/\psi\Lambda$ (a) and $B^0 \to J/\psi K_s^0$ (b) decays.

$$\sigma_{\overline{\epsilon}} = \sqrt{\frac{1}{\sum_{i=1}^{3} \frac{1}{\sigma_i^2}}} \tag{6.4}$$

Using these equations we found: $\overline{\epsilon} = 2.370 \pm 0.047$. In addition, if we combine all three data periods in one data set, we find $N_{\Lambda_b} = 314 \pm 29$ and $N_{B^0} = 2335 \pm 73$. This is shown in figure 6.1. If we plug in these numbers and the average ratio of efficiencies in equation 6.1, we obtain

$$\overline{v} = \frac{f(b \to \Lambda_b) \cdot \mathcal{B}[\Lambda_b \to J/\psi\Lambda^0]}{f(b \to B^0) \cdot \mathcal{B}[B^0 \to J/\psi K_S^0]} = 0.345 \pm 0.034\ (stat.) \pm 0.003\ (PDG) \tag{6.5}$$

The last uncertainty comes from $\frac{\mathcal{B}(K_s^0 \to \pi^+\pi^-)}{\mathcal{B}(\Lambda \to p\pi^-)} = 1.083 \pm 0.009$ which has been obtained from the reported values [**?**] $\mathcal{B}(K_s^0 \to \pi^+\pi^-) = 0.6920 \pm 0.0005$ and $\mathcal{B}(\Lambda \to p\pi^-) = 0.639 \pm 0.005$. The uncertainty on the $\frac{\mathcal{B}(K_s^0 \to \pi^+\pi^-)}{\mathcal{B}(\Lambda \to p\pi^-)}$ ratio is estimated assuming no correlations between the uncertainty of each branching fraction.

This measurement is consistent with what we obtain for each data taken periods separately reported in Table 5.4. This new measurement is the most precise to date and exceeds the precision of the current value reported as the world-average 0.27 ± 0.12 (stat.) ± 0.05 (syst.) [**?**]. If we use $f(b \to B^0) \cdot \mathcal{B}(B^0 \to J/\psi K_s^0) = (1.74 \pm 0.08) \times 10^{-5}$ from [**?**], we can obtain

$$f(b \to \Lambda_b) \cdot \mathcal{B}(\Lambda_b \to J/\psi\Lambda) = (6.0 \pm 0.6 \text{ (stat.)} \pm 0.3 \text{ } (\mathcal{B})) \times 10^{-5}. \tag{6.6}$$

The result in eq. 6.6 can be compared directly to the reported world-average $(4.7 \pm 2.3) \times 10^{-5}$ [**?**].

6.2 Systematic Errors

For the measurement of v we consider de following sources of systematics uncertainties.

6.2.1 Mass Model and Background Model

To extract the Λ_b and B^0 yields, we use a model of two Gaussians for signal (as observed in MC) and a second polynomial distribution for background. To investigate a possible source of systematic uncertainty due to the choice of the model, the fit is repeated with an exponential function to model the background and a single Gaussian for signal. This is done separately for both, Λ_b and B^0. We observed a deviation of 2.6% to the central value of v. We consider this as a sistematic due to this source.

6.2.2 Background Model and Mass Model

The signal peak is fitted with one Gaussian and the background with a exponential function.

We studied various background models, such as those tried by the referee, and we selected the model that returns the best χ^2 when projected on data (all our fits are actually unbinned log-likelihood fits). In the case of the linear background

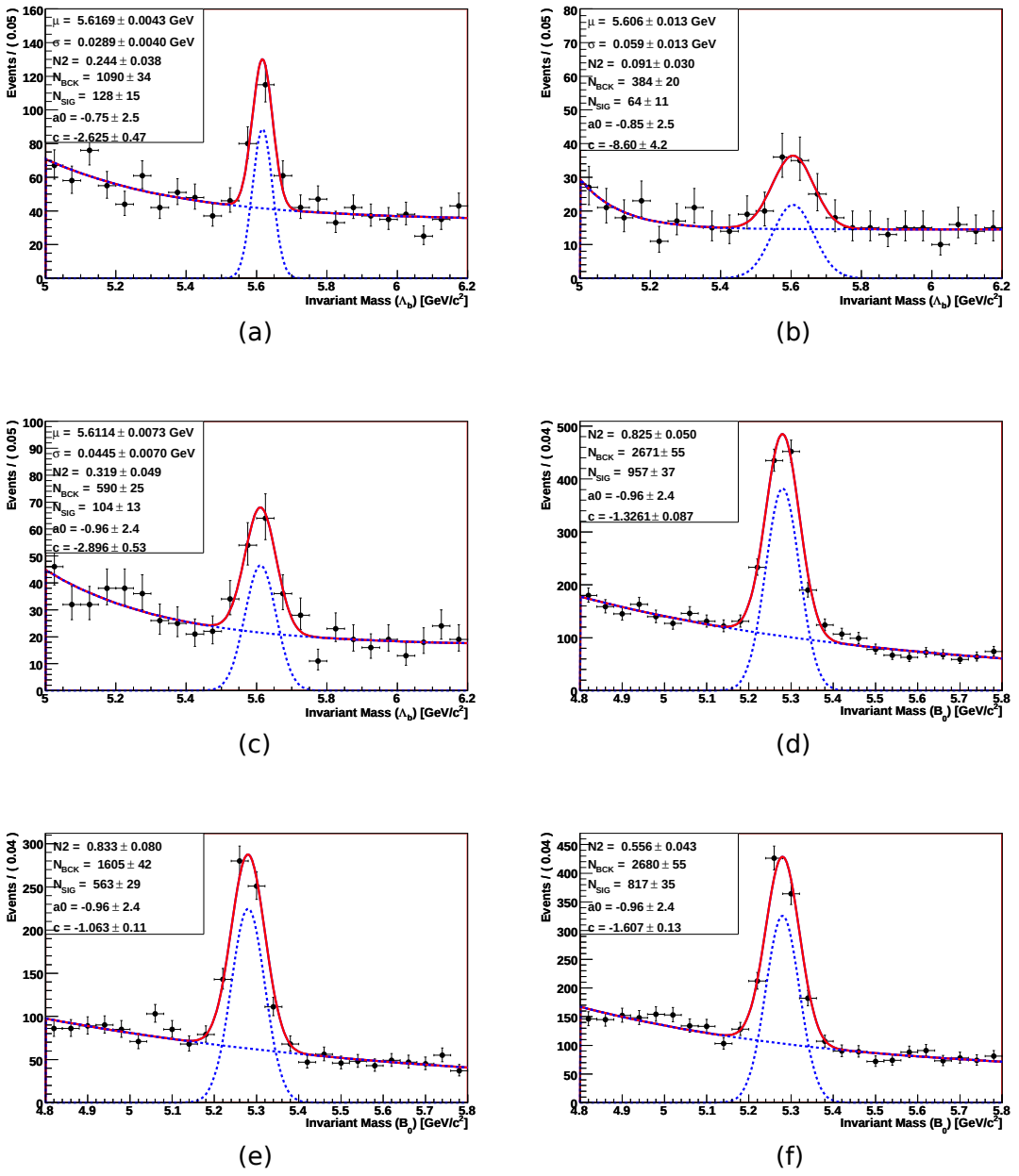

Figure 6.2: Fit for the events observed from the decay Λ_b^0 ; *a*) Run IIa, *c*) Run IIb1 and *c*) Run IIb2. Fit for the events observed from the decay $B_d^0 \to J/\psi K_s^0$ *d*) Run IIa, *e*) Run IIb1 and *f*) Run IIb2;

for describing the background, this yields substantial variation in the number of Λ_b, and also the χ^2 for linear fit is rather poor, so this is clearly not the way to fit the background and variations in the number of Λ_b is overestimated in this case.

In the next two tables are the results of the fits combining the 3 different models for the background and a double Gaussian for the signal.

Model	Numbers Λ_b	Δ
	Nominal Value, $N_{\Lambda_b} = 314 \pm 29$	
Nominal Mass Range $(5.0, 6.2)$		
2 Gauss + Pol 1	262 ± 26	16.5 %
2 Gauss + Pol 2	314 ± 29	0.0 %
2 Gauss + Exp	312 ± 24	0.6 %

Model	Numbers B^0	Δ
	Nominal Value, $N_{B^0} = 2335 \pm 73$	
Nominal Mass Range $(4.8, 5.8)$		
2 Gauss + Pol 1	2229 ± 64	4.5 %
2 Gauss + Pol 2	2335 ± 73	0.0 %
2 Gauss + Exp	2297 ± 58	1.6 %

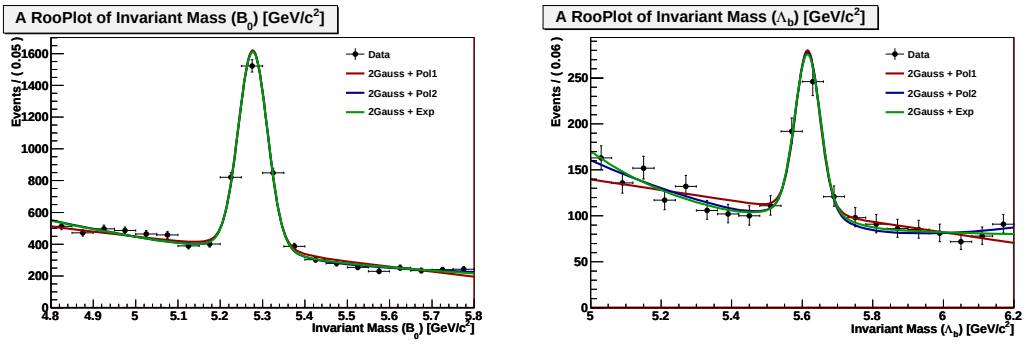

Figure 6.3: Combining the 3 different models for the background and double Gaussian for the signal.

To clear any doubt on the assigned systematic, we selected a narrow mass window, such that there is almost no difference between the background models (exponential, 1st or 2sd order polynomial), and performed a fit for each model.

The results in the relative yield did no changed by more than the assigned 5.5% systematic, reinforcing our previous studies and assignment of this uncertainty.

In the next two tables are the results of the fits combining the 3 different models for the background and a double Gaussian for the signal in a narrow mass window.

Model	Numbers Λ_b	Δ
	Nominal Value, $N_{\Lambda_b} = 314 \pm 29$	
Mass Range $(5.35, 5.85)$		
2 Gauss + Pol 1	305 ± 41	2.8 %
2 Gauss + Pol 2	312 ± 32	0.6 %
2 Gauss + Exp	310 ± 24	1.2 %

Model	Numbers B^0	Δ
	Nominal Value, $N_{B^0} = 2335 \pm 73$	
Mass Range $(5.05, 5.5)$		
2 Gauss + Pol 1	2380 ± 71	1.9 %
2 Gauss + Pol 2	2279 ± 71	2.4 %
2 Gauss + Exp	2408 ± 61	3.1 %

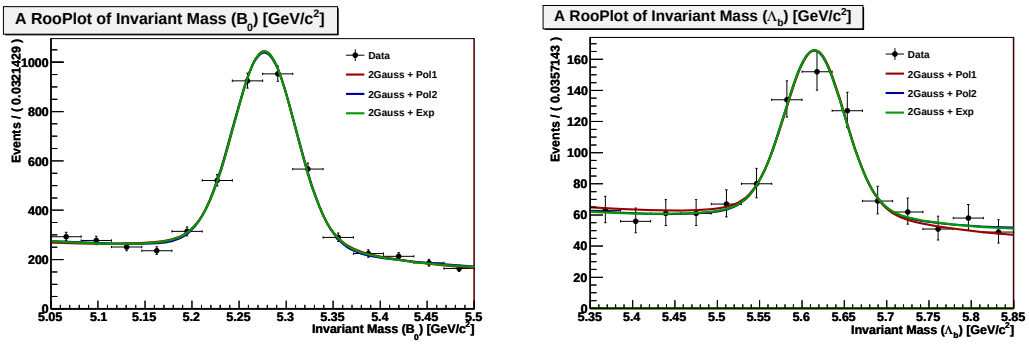

Figure 6.4: Combining the 3 different models for the background and double Gaussian for the signal.

6.2.3 Signal Decay Model for B_0

The extraction of Monte Carlo parameters was repeated using an independently generated sample, in which the decay model SVS_CP was set in the evtgen pack-

age instead of the default 'phase space' model that was used for the nominal analysis. The SVS_CP model is the decay of a scalar to a vector and a scalar and allows for CP violating time asymmetries. This model uses the decay amplitudes together with the time evolution of the $B\bar{B}$ system and the flavor of the other B to generate the time distributions. See Ref [**?**] for details. We observed a deviation in v of 2.0%. We quote this a systematic uncertainty due to the decay model of B^0.

6.2.4 Background from B_d^0 and Λ_b^0

Due to the similar topology of both decays, we may have contamination from B_d^0 candidates identified as Λ_b^0 and vice versa. To estimate this contamination, in the B_d^0 MC sample we look for Λ_b^0 candidates reconstructed as B_d^0 . Then we estimate the expected number of events due to this contamination by using the number of reconstructed Λ_b^0 candidates in data. The results of these studies are summarised in Table 6.2, and show that the number of expected background events from such reflections is small. When we consider this in the computation of v we find a change of 2.3% that we quote as a systematic due to this source.

Table 6.2: Background information

Particle	Run	Reconstructed correctly # events	Reconstructed incorrectly # events	Expected in data # events
Λ_b^0	IIa	1926	9	1
B_d^0	IIa	5193	3	4
Λ_b^0	IIb1	1044	14	1
B_d^0	IIb1	3010	3	7
Λ_b^0	IIb2	642	4	1
B_d^0	IIb2	616	3	5

6.2.5 Λ_b^0 Polarization

In this section we study the effect of the Λ_b^0 polarization and decay parameters on the reconstruction efficiency. The decay $\Lambda_b^0 \to J/\psi\Lambda$ can be described completely in terms of four helicity amplitudes $A(\lambda_\Lambda, \lambda_{J/\psi})$ and follows an angular distribution given by

$$w(\vec{\theta}; \vec{A}; P_b, \alpha_\Lambda) \propto \sum_{i=0}^{i=19} f_{1i}(\vec{A}) f_{2i}(P_b, \alpha_\Lambda) F(\vec{\theta}). \tag{6.7}$$

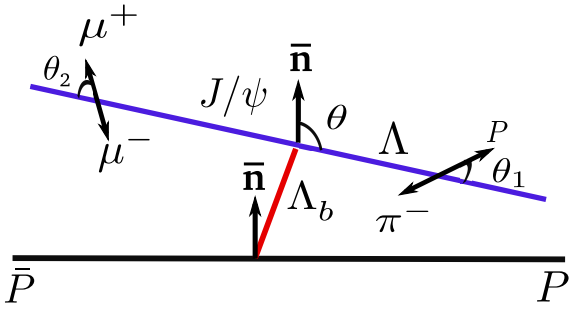

Figure 6.5: Cascade decay for Λ_b^0 , $\Lambda_b^0 \to J/\psi\Lambda^0$, $\Lambda^0 \to p + \pi^-$, $J/\psi \to \mu^+ + \mu^-$

The five angles $\vec{\theta} = (\theta, \theta_1, \theta_2, \phi_1, \phi_2)$ in this probability function are depicted in Figure 6.5 (a detailed description can be found in Ref. [**?**]). P_b denotes the Λ_b^0 polarization and α_Λ is the decay asymmetry parameter of Λ. The amplitudes and polarization are independent unknown parameters, and can be varied to obtain the maximum deviation from our nominal value. By integrating Eq. (6.7) in four angles, it can be shown that only the distributions of θ and ϕ_1 depend on P_b (θ being the most relevant). In particular, θ obeys the simple relation

$$w(\theta; \vec{A}, P_b) = \frac{1}{2}\left(1 + P_b \alpha_b \cos\theta\right), \tag{6.8}$$

where α_b is the Λ_b decay asymmetry parameter, which is given in terms of the helicity amplitudes.

In order to determine which combination of $\alpha_b P_b$ changes more our reconstruction efficiency, the shape of the $\cos\theta$ distribution is manually ajusted in MC to account for all possible polarizations, allowing $P_b\alpha_b$ to vary in the full range

from -1 to 1. This test is performed exclusively on Run IIa Monte Carlo data, as described below.

For each trial (i.e. for each value of $P_b\alpha_b$), the events are filtered using random rejection at the generation level, and the reconstruction efficiency corresponding to this trial is measured. Figure 6.6 shows an example of the distributions produced by this method.

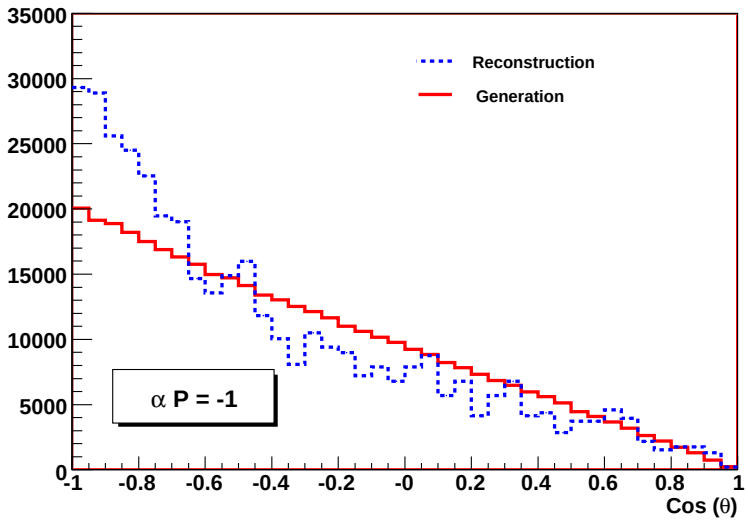

Figure 6.6: An example of the effect of adjusting the generation level polarization on the corresponding reconstructed $\cos\theta$ distribution, using Run IIa Monte Carlo, for the case $P_b\alpha_b = -1$. The continuous line is the distribution after filtering at generation level and the dashed line is the reconstructed distribution.

The results of these tests are summarized in Table 6.3, which shows the measured efficiencies using different values of $P_b\alpha_b$.

We take $P_b\alpha_b = 0$ as a reference because this sample did not require random event filtering. Figure 6.7 show the relative change (in percentage) in the measured reconstruction efficiency, with respect to the reference value at $P_b\alpha_b = 0$. The maximum change corresponds to $P_b\alpha_b = -1$, where the fractional change in efficiency is around 4.2%.

Having determined that the largest shift in efficiency for Run IIa is coming from the extreme values $P_b\alpha_b = \pm 1$, we produced MC including Λ_b polarization at the level of EvtGen and passing our detector simulation. The procedure is

Table 6.3: Summary of the effect of varying the Λ_b^0 polarization on the final measured rreconstruction efficiency. The observed variation is very small.

$P_b\alpha_b$	$\epsilon_{\Lambda_b^0} \times 10^{-3}$
0	2.74 ± 0.06
-1	2.62 ± 0.09
-0.75	2.66 ± 0.09
-0.5	2.64 ± 0.09
-0.25	2.74 ± 0.09
0.25	2.73 ± 0.09
0.5	2.70 ± 0.09
0.75	2.72 ± 0.09
1	2.68 ± 0.09

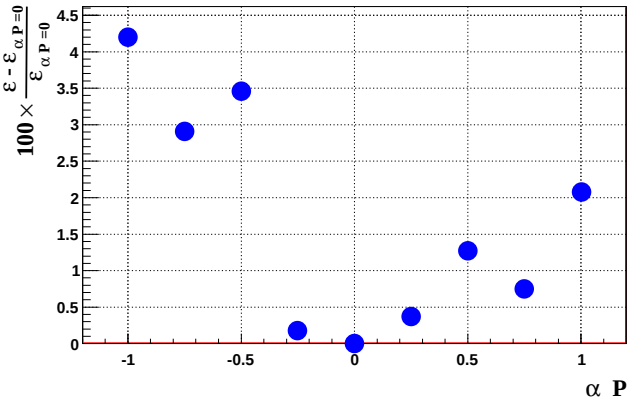

Figure 6.7: The relative change (in percentage) in the measured reconstruction efficiency with respect to the reference value at $P_b\alpha_b = 0$.

described in the following subsection.

6.2.6 Λ_b^0 polarization with EvtGen

To have a better estimation of the Λ_b^0 polarization effect on our branching ratio measurement, instead of using the simple accept-reject approach, here we generated Monte Carlo with Λ_b^0 initially polarized. We use the EvtGen package to achieve this goal.

The procedure is as follows: we generate $p\overline{p}$ Monte Carlo events forcing

$b\overline{b}$ production. Λ_b^0 particles are set stable in Pythia and EvtGen forces the decays to $J/\psi(\mu^+\mu^-)\Lambda^0$. We still let Geant to decay Λ^0. EvtGen class HELAMP was modified (extended) to receive an odd number of parameters (in our case, polarization is set only if 9 parameters are found), the last one being the value of the Λ_b^0 polarization (along the z axis). The polarization vector is

$$\vec{P} = \frac{\hat{z} \times \vec{p}}{|\hat{z} \times \vec{p}|} \tag{6.9}$$

and the spin desinty matrix

$$\vec{\rho} = \frac{1}{2}\left(\mathbf{I} + \vec{\sigma} \cdot \vec{p}\right) \tag{6.10}$$

is associated to the Λ_b^0 particle. Here $\vec{\sigma}$ are Pauli Matrices and $\vec{p}$ is the momentum of the Λ_b^0 particle in the lab system. Once the spin densinty matrix is set to Λ_b^0, the HELAMP method (which from now remains unchanged) decays the particle acording to (user's) established helicity amplitudes. As already mentioned, four helicty amplitudes describe the decay $\Lambda_b^0 \to J/\psi\Lambda$:

$$a_+ = \mathcal{M}_{+\frac{1}{2},0}, \;\; a_- = \mathcal{M}_{-\frac{1}{2},0}, \;\; b_+ = \mathcal{M}_{-\frac{1}{2},-1}, \;\; b_- = \mathcal{M}_{\frac{1}{2},+1}, \tag{6.11}$$

where $\mathcal{M}_{\lambda,\lambda'}$ denotes the amplitude for the Λ_b^0 to decay into Λ^0 and J/ψ with helicities λ and λ'. The amplitudes obey a normalization condition (sum of the square norms equals to 1) and from them the asymmetry parameter α_b caused by the parity non-conservation of the weak interactions can be defined:

$$\alpha_b \equiv \frac{|a_+|^2 + |b_+|^2 - |a_-|^2 - |b_-|^2}{|a_+|^2 + |b_+|^2 + |a_-|^2 + |b_-|^2} \tag{6.12}$$

We generated three samples, aproximately 800k each.

1. $\alpha P = 1$: $P = -1$ and $\alpha = -1$.

   $a_+ = b_+ = 0$,
   $a_- = 0.269016 \exp(1.10715i) = 0.120307 + 0.240615i$,
   $b_- = 0.963135 \exp(1.53331i) = 0.0360922 + 0.962459i$

2. $\alpha P = -1$: $P = 1$ and $\alpha = -1$.

$a_+ = b_+ = 0,$
$a_- = 0.269016 \exp(1.10715i) = 0.120307 + 0.240615i,$
$b_- = 0.963135 \exp(1.53331i) = 0.0360922 + 0.962459i$

3. $\alpha P = 0.37$: $P = -0.8$ and $\alpha = -0.457$.

   $a_+ = 0.429 \exp(-1.612i),$
   $b_+ = 0.295 \exp(-1.849i),$
   $a_- = 0.260 \exp(1.231i),$
   $b_- = 0.813 \exp(1.534i)$

In Fig. 6.8 we show $\cos\theta$ for the generated samples, where θ is the polar angle of the Λ^0 momentum in the Λ_b^0 rest frame (z-axis parallel to the normal of the production plane). As mentioned earlier in this note, the main effect of the polarization is observed through this angle.

To exemplify the use of the extended EvtGen class, below we show the contents of the "user.dec" file for the first case above.

```
Alias myJ/psi J/psi
Decay Lambda_b0
1.0000  Lambda0 myJ/psi HELAMP 0.963 1.533 0.0 0.0 0.269 1.107 0.0 0.0 -1;
#                                b-(1/2,1) a+(1/2,0) a-(-1/2,0) b+(-1/2,-1)
Enddecay
Decay myJ/psi
1.000    mu+  mu-             PHOTOS VLL;
Enddecay
End
```

From these fully simulated samples we compute new efficencies including polarization and found a maximum deviation is 7.2% in the determination of v, when $\alpha_b P = +1$. This is included as a systematic due to a possible polarization of the Λ_b.

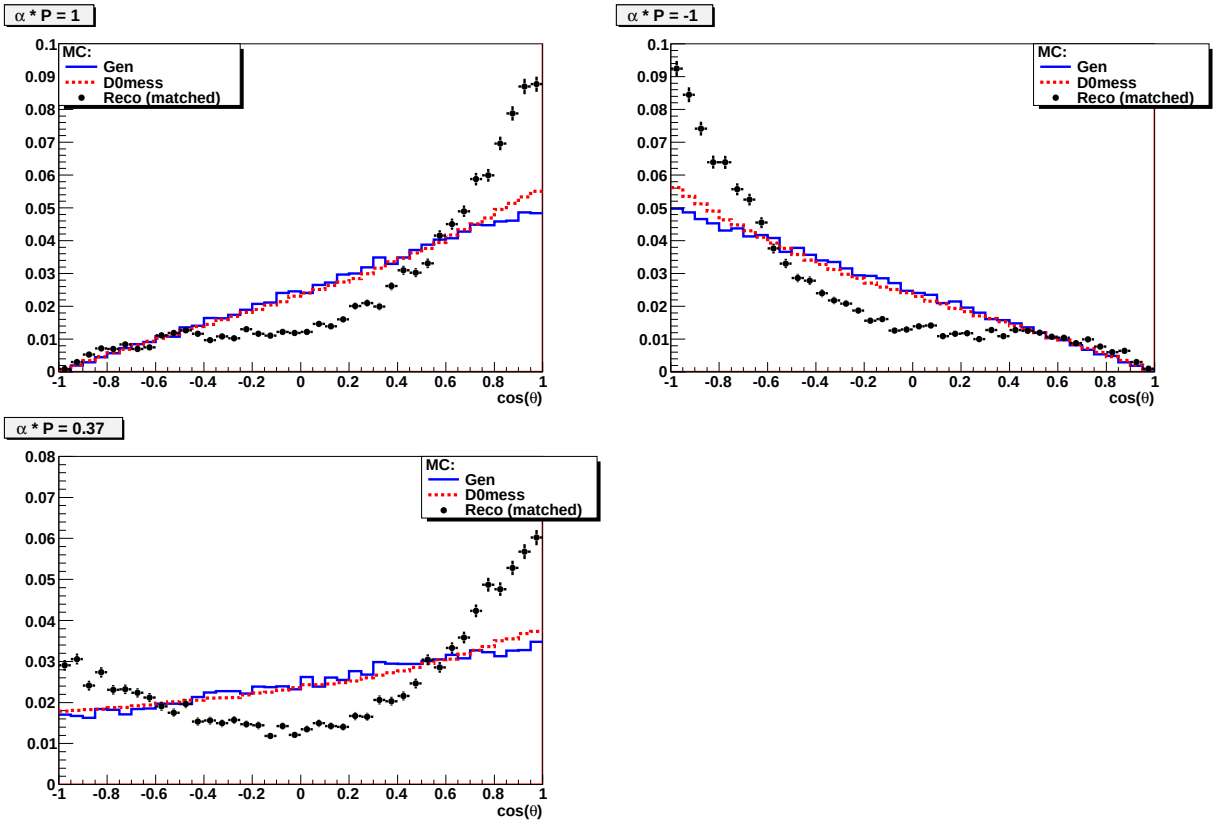

Figure 6.8: Polarized Λ_b^0 Monte Carlo, $\cos\theta$ angle: Generated (solid blue), after D0mess (dotted red), and after reconstruction (black points). Histograms are normalized to have the same area.

6.3 Summary of estimated systematic uncertainties

In the previous section we studied the sources of systematic uncertainties for the measurement of v. Table 6.4 list all the sources of systematic uncertainty considered in this analysis, and their effects on the parameter of interest.

Table 6.4: Systematic error for v

Test	Systematic uncertainty (%)
Fit Model	5.5
Signal Decay Model for B_0	2.0
Background from B_d^0 and Λ_b^0	2.3
Λ_b^0 Polarization ($P_b\alpha_b = +1$)	7.2
Total (in quatdrature)	9.6

6.4 Consistency Studies

In order to test the stability of our measurement we do the following cross checks.

6.4.1 Trigger efficiencies for Λ_b^0 and B_d^0

In this analysis, for both,Λ_b^0 and B_d^0 , triggers affect mainly p_T distribution on the leading muon of the J/Ψ. In order to check any difference due to triggers efficiency for these decay channels, we compare the p_T distribution of the leading muon for the two decays. The next plot illustrates this comparison.

The top part of the plot shows the p_T distribution of the leading muon for both decays (after background subtraction). The bottom part of the plot shows the ratio of the two distributions on the top plot. There is good agreement in the leading μ_{p_T} distributions within 2 and 8 GeV/c . This is the p_T region where most ($\sim 75\%$) of the Λ_b^0 and $\bar{\Lambda}_b^0$ candidates are found. For high p_T the agreement is within 2σ.

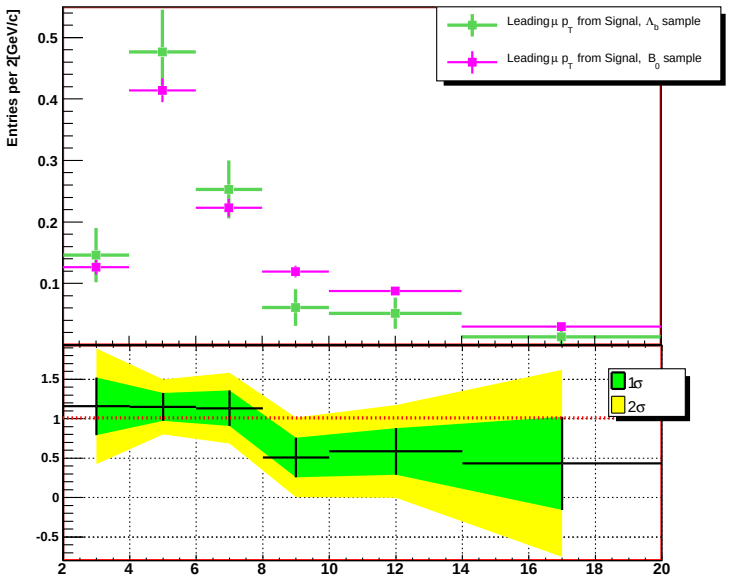

Figure 6.9: Comparison between the p_T distribution of the leading muon for Λ_b^0 and B_d^0

6.4.2 Data and MC comparison

We produced comparison plots for MC and data (signal after background subtracted) for the variables used in the optimization. The bottom part of the plot shows the ratio of data to MC distributions. All distributions are consistent, specially in the regions where most of the Λ_b^0 and $B_d^0 \to J/\psi K_s^0$ candidates are mainly found.

The next plots show the collinearity distribution. This cut is used to romeved contamination coming from $\Sigma \to \Lambda + \gamma$. We have produced some plots of this variable comparing MC vs data (signal after background subtracted). The distributions are normalized to 1.

6.4.3 Data efficiency ratio and the MC efficiency ratio

To perform this test we add the run IIa, runIIb1 and runIIb2 in one data sample, and the same was done for the MC. We divided the sample in just two bins due to the low statistics , for three different variables.

Table 6.5: Test with pT (Λ_b)

	Central value	pT $(\Lambda_b) < 12$	pT $(\Lambda_b) > 12$
$\frac{\frac{N_{obs}[\Lambda_b \to J/\psi \Lambda^0]}{N_{obs}[B^0 \to J/\psi K_S^0]}}{\frac{N_{reco}^{(MC)}[\Lambda_b \to J/\psi \Lambda^0]}{N_{reco}^{(MC)}[B^0 \to J/\psi K_S^0]}}$	0.37 ± 0.05	0.34 ± 0.06	0.41 ± 0.08

Table 6.6: Test with Decay Length (Λ^0)

	Central value	D. L. $(\Lambda^0) < 8$	D. L. $(\Lambda^0) > 8$
$\frac{\frac{N_{obs}[\Lambda_b \to J/\psi \Lambda^0]}{N_{obs}[B^0 \to J/\psi K_S^0]}}{\frac{N_{reco}^{(MC)}[\Lambda_b \to J/\psi \Lambda^0]}{N_{reco}^{(MC)}[B^0 \to J/\psi K_S^0]}}$	0.37 ± 0.05	0.38 ± 0.07	0.35 ± 0.08

Table 6.7: Test with $|\eta|$ (Λ_b)

	Central value	$\|\eta\|$ $(\Lambda_b) < 1$	$\|\eta\|$ $(\Lambda_b) > 1$
$\frac{\frac{N_{obs}[\Lambda_b \to J/\psi \Lambda^0]}{N_{obs}[B^0 \to J/\psi K^0_S]}}{\frac{N^{(MC)}_{reco}[\Lambda_b \to J/\psi \Lambda^0]}{N^{(MC)}_{reco}[B^0 \to J/\psi K^0_S]}}$	0.37 ± 0.05	0.32 ± 0.07	0.43 ± 0.1

6.4.4 Λ^0 and K^0_S life time

We have estimated the lifetime of the K^0_S and Λ^0 in our data, taking into account detector efficiencies as obtained from Monte Carlo simulation. The parameter $p1$ in the plots below is the value of the lifetime (in cm) obtained from a fit to the K^0_S and Λ^0 proper decay length Signal distribution (data after background subtraction) once corrected by the detector efficiency.

For K^0_S

- PDG: $c\tau = 2.69$ cm
- Fit: $c\tau = 2.44 \pm 0.26$ cm

For Λ^0

- PDG: $c\tau = 7.89$ cm
- Fit: $c\tau = 9.028 \pm 6.53$ cm

Also the comparison between signal and MC after reconstruction is showed below. It's worth to mention that the Monte-Carlo follows data really well. For Λ^0 the statistics is low ~ 300 events, compared with the kS ~ 2300 events. These results are in agreement wit h the PDG and no bias is observed. We conclude that any detector efficiency on the decay length is modeled correctly by our Monte Carlo (detector simulation), and since this is taken into account in our Branching Ratio calculation, there is not bias from this source in our result.

6.4.5 Λ^0_b and $\bar{\Lambda}^0_b$ reconstruction efficiency

To be sure that both $\Lambda^0_b \to J/\psi\Lambda^0$ and $\bar{\Lambda}^0_b \to J/\psi\bar{\Lambda}_0$ decays have a similar reconstruction efficiency, the samples were separated and the reconstruction effi-

ciency determined separately for each sub-set of data. The results are shown in Table 6.8

Table 6.8: Comparison of reconstruction efficiencies for the decay $\Lambda_b^0 \to J/\psi\Lambda^0$ and its conjugate process.

Run	$\epsilon_{\Lambda_b^0}$	$\epsilon_{\bar{\Lambda}_b^0}$	$\epsilon_{\Lambda_b^0}/\epsilon_{\bar{\Lambda}_b^0}$
RunIIa	28.05×10^{-4}	26.92×10^{-4}	1.05
RunIIb1	13.62×10^{-4}	14.30×10^{-4}	0.95
RunIIb2	6.55×10^{-4}	6.73×10^{-4}	0.97

In addition, the channels Λ_b^0 and $\bar{\Lambda}_b^0$ are separated in real data, by cutting on the parameter α corresponding to the *Armenteros–Podolanski* plot. The condition $\alpha > 0$ isolates Λ_b^0 -like events, and $\alpha < 0$ isolates $\bar{\Lambda}_b^0$ -like events. The results are summarized in Table 6.9

Table 6.9: Comparison of the final branching ratio measurements for the decay $\Lambda_b^0 \to J/\psi\Lambda^0$ and its conjugate process, where the separation of the two processes is achieved using the *Armenteros–Podolanski* parameter α.

Test	v	$\mathcal{B}(\Lambda_b \to J/\psi\Lambda^0) \times f(b \to \Lambda_b) \times 10^{-5}$
Central Value	0.335 ± 0.040	5.84 ± 0.70
Only Λ_b^0	0.292 ± 0.073	5.09 ± 1.10
Only $\bar{\Lambda}_b^0$	0.367 ± 0.062	6.38 ± 0.99

6.4.6 Random Selection

The entire data-set is randomly divided into two equally-sized sub-samples, and the measurement performed separately in each sub-sample. The results are shown in Table 6.10

Table 6.10: Results determined separately in one subsamples, defined by random allocation of events.

Test	v	$\mathcal{B}(\Lambda_b \to J/\psi\Lambda^0) \times f(b \to \Lambda_b) \times 10^{-5}$
Central Value	0.335 ± 0.040	5.84 ± 0.70
Random	0.327 ± 0.059	5.69 ± 0.93

6.5 Calculating $\mathcal{B}(\Lambda_b \to J/\psi\Lambda)$

The branching fraction $\mathcal{B}(\Lambda_b^0 \to J/\psi\Lambda^0)$ is slightly more difficult to report since there is not a published measurement of $f(b \to \Lambda_b)$. On the other hand, the D0 and CDF experiments have observed other weakly decaying baryons such as the Ξ_b^-,Ξ_b^0 and Ω^- , as was explained in the Chapter 2, the general assumption that $f(b \to b_{baryon}) = f(b \to \Lambda_b)$ is not correct. A better approximation is to include the contribution of the Ξ_b^0 in the calculation, such that $f(b \to b_{baryon}) = f(b \to \Lambda_b) + f(b \to \Xi_b^0) + f(b \to \Xi_b^-)$. Furthermore, we can assume isospin invariance to set $f(b \to \Xi_b^-) = f(b \to \Xi_b^0)$. It was also observed in Ref. [42] that

$$\frac{f(b \to B_s)}{f(b \to B^0)} \sim \frac{f(b \to \Xi_b^-)}{f(b \to \Lambda_b)} \tag{6.13}$$

Using the PDG values of $f(b \to B^0)$, $f(b \to B_s)$ and $f(b \to b_{baryon})$ (from the combination of LEP and Tevatron results) and their correlations (see section), we obtain

$$\begin{aligned} \mathcal{B}(\Lambda_b \to J/\psi\Lambda) \approx & \quad \frac{f(b \to B^0)}{f(b \to b_{baryon})} \times [1 + 2\frac{f(b \to Bs)}{f(b \to B^0)}] \times \mathcal{B}(B^0 \to J/\psi K_s^0) \times \sigma_{rel} \\ = & \quad (11.08 \pm 1.09(stat) \pm 1.06(syst) \pm 2.94(PDG)) \times 10^{-4} \\ = & \quad (11.08 \pm 3.31) \times 10^{-4} \end{aligned} \tag{6.14}$$

The same assumptions on $\sigma_{rel}^{W.A.}$ [1] leads to $\mathcal{B}(\Lambda_b \to J/\psi\Lambda) = (8.67 \pm 4.84) \times$

[1] σ_{rel} of the World Average

10^{-4}. Both results are consistent within errors and favor theoretical models which predict a larger value for this branching ratio.

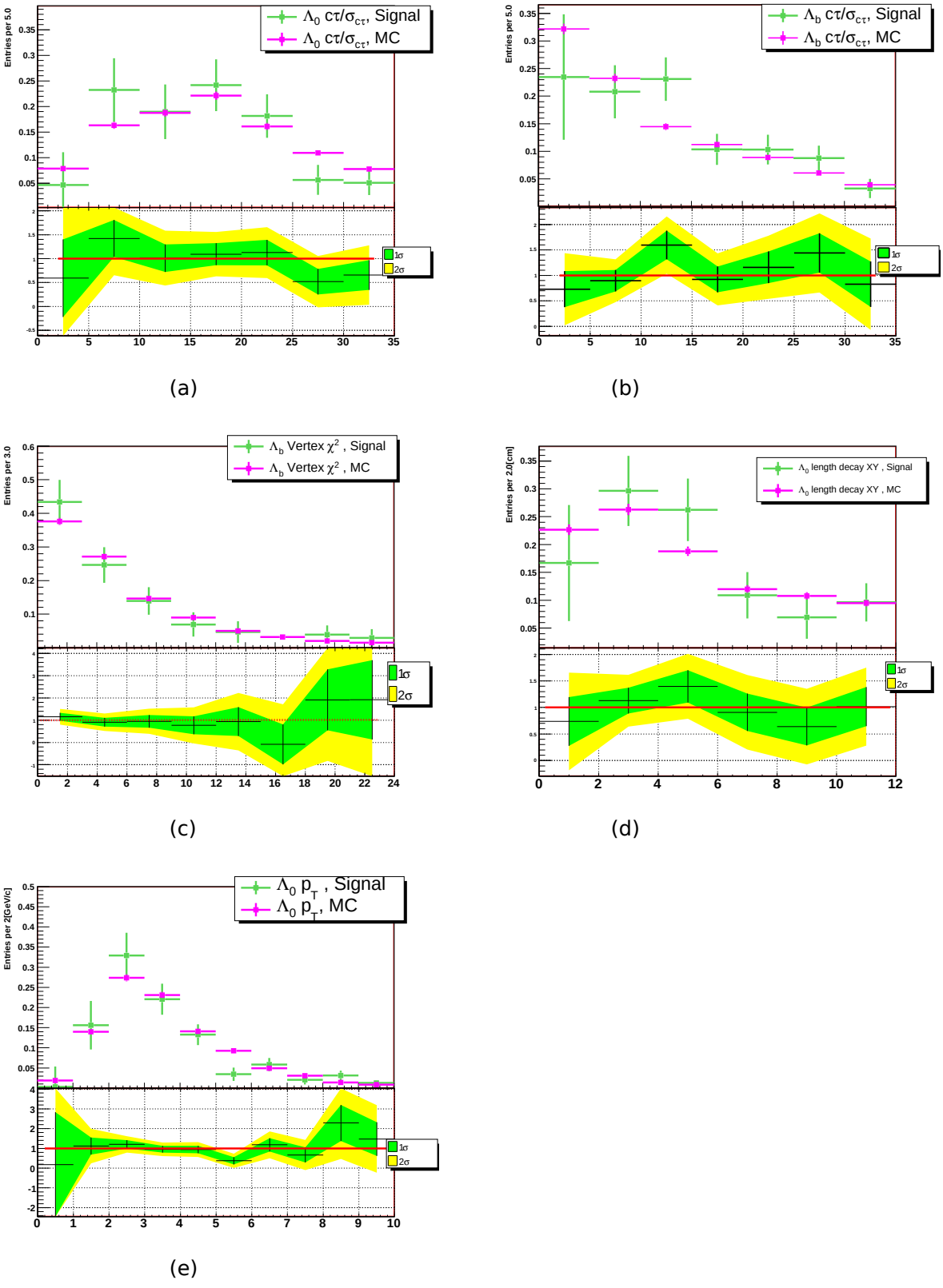

Figure 6.10: Data and MC comparison, *a*) $c\tau/\sigma_{c\tau}$ (Λ^0), *b*) $c\tau/\sigma_{c\tau}$ (Λ_b^0), *c*) χ^2 (Λ_b^0) , *d*) Length Decay XY (Λ^0) and ~~e~~) P_T (Λ^0)

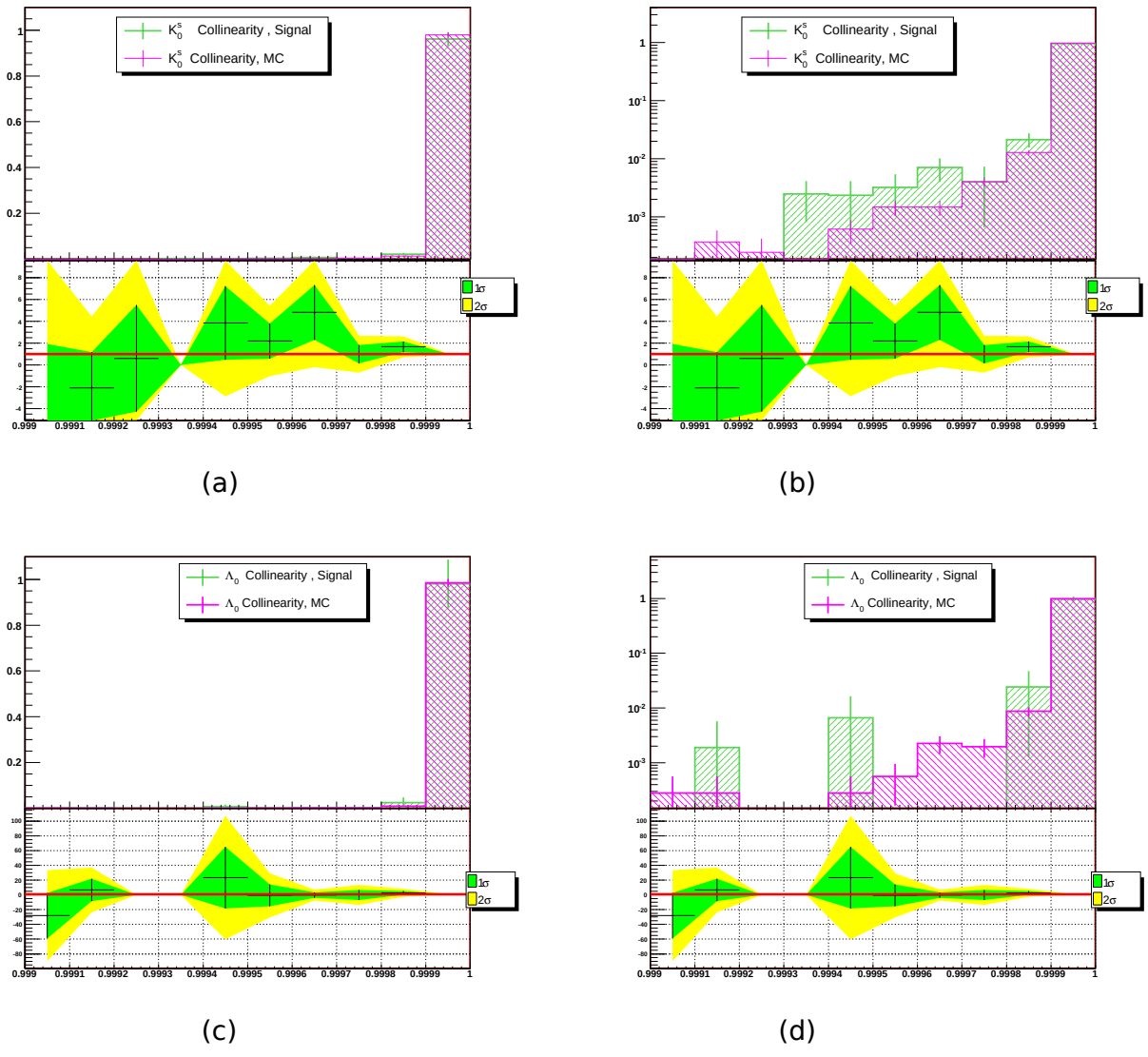

Figure 6.11: Data and MC comparison. Collinearity for Λ^0 *a*) normal scale, *b*) logarithmic scale and K^0_S *c*) normal scale, *d*) logarithmic scale

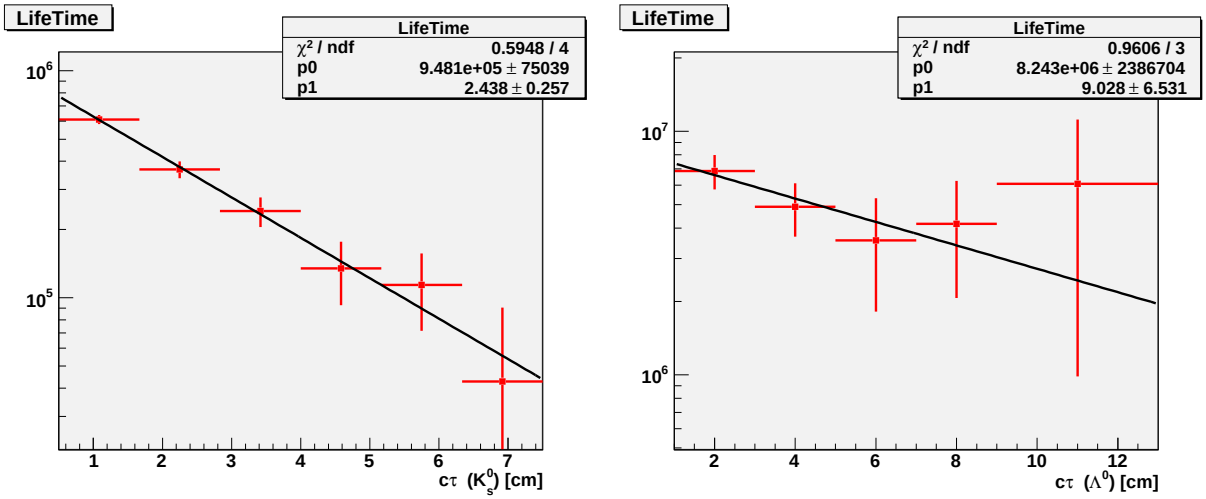

Figure 6.12: Fit to the K_S^0 and Λ^0 proper decay length signal distribution

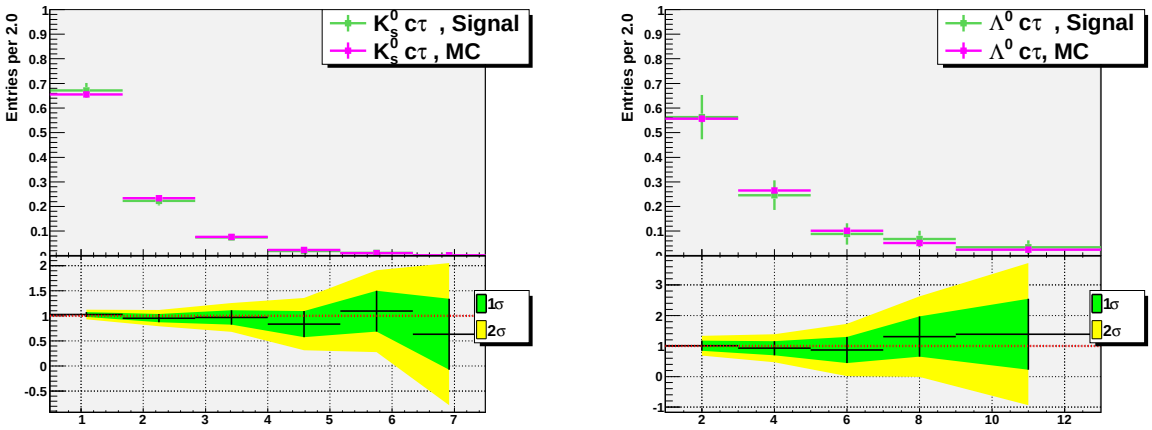

Figure 6.13: Comparison between signal and MC after reconstruction

Chapter 7

Search for the rare Decay $\Lambda_b^0 \to \mu^+\mu^-\Lambda^0$

In this Chapter the search for the rare decay $\Lambda_b^0 \to \mu^+\mu^-\Lambda^0$ will be presented. The measurement of a branching fraction requires the determination of the integrated luminosity or the normalisation to a similar decay with a known branching fraction. For this search the decay of $\Lambda_b^0 \to J/\psi\Lambda^0$ has been used for normalisation. The decay channels are illustrated schematically in Fig. 7.1

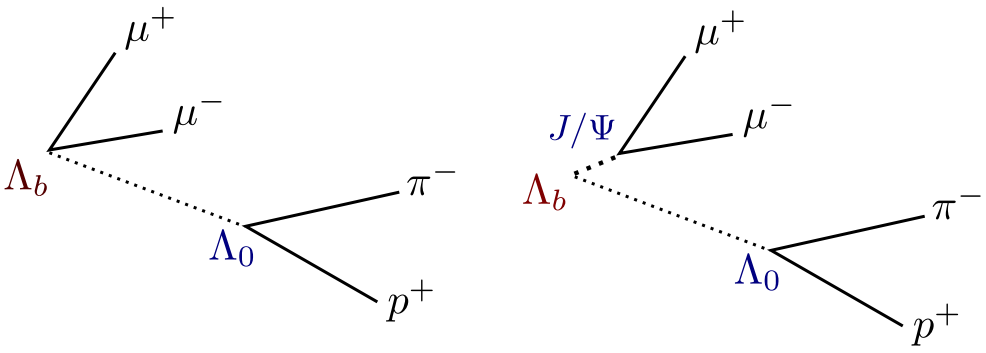

Figure 7.1: Topological view of the decays $\Lambda_b^0 \to \mu^+\mu^-\Lambda^0$ and $\Lambda_b^0 \to J/\psi\Lambda^0$

The search was performed as a "blind box" analysis, with the signal region hidden during all analysis steps. The strategy of the analysis is to start with a pre-selection and then use discriminating variables in an optimisation procedure to further reduce the expected background. The estimation of the background

in the signal region is obtained by interpolating the remaining background from sidebands into the signal region.

7.1 Data samples

The analysis presented here is based on data collected by the D0 Detector between April 2002 and July 2010:

- Run IIa: April 20, 2002 - February 22, 2006
- Run IIb-1: June 9, 2006 - August 4, 2007
- Run IIb-2: October 28, 2007 - June 13, 2009
- Run IIb-3: September 15, 2009 - July 18, 2010

We use the single muon data skims, produced from the thumbnails, and converted into a streamlined b-physics file format ("AADST"). In the case of Monte Carlo samples, for the RunIIb-2 and RunIIb-3 was considered the same version.

7.2 $\mathcal{B}\left(\Lambda_b^0 \to \mu^+\mu^-\Lambda^0\right)$ calculation

The $\mathcal{B}\left(\Lambda_b^0 \to \mu^+\mu^-\Lambda^0\right)$ is calculated by comparing with the well-known and topologically similar decay $\Lambda_b^0 \to J/\psi\Lambda^0$. Following the same steps than in the Chapter (**??**), the calculation proceeds as follows:

The number of observed Λ_b^0 events in the channel $\Lambda_b^0 \to \mu^+\mu^-\Lambda^0$ is:

$$\begin{aligned} N_{obs}[\Lambda_b \to \mu^+\mu^-\Lambda^0(p\pi^-)] = \quad & N_{produced}[\Lambda_b \to \mu^+\mu^-\Lambda^0(p\pi^-)] \\ & \times \epsilon_R[\Lambda_b \to \mu^+\mu^-\Lambda^0(p\pi^-)] \end{aligned} \tag{7.1}$$

where the true number of decays produced is given by:

$$N_{produced}[\Lambda_b \to \mu^+\mu^-\Lambda^0(p\pi^-)] = \quad \mathcal{L}\cdot\sigma(p\overline{p}\to b\overline{b})\cdot f(b\to\Lambda_b) \times\mathcal{B}\left(\Lambda_b\to\mu^+\mu^-\Lambda^0\right) \times\mathcal{B}\left(\Lambda^0\to p\pi^-\right) \tag{7.2}$$

We proceed in the same way for $\Lambda_b^0 \to J/\psi\Lambda^0$, we can get combining with $\Lambda_b^0 \to \mu^+\mu^-\Lambda^0$,

$$\frac{\mathcal{B}\left(\Lambda_b\to\mu^+\mu^-\Lambda^0\right)}{\mathcal{B}\left(\Lambda_b\to J/\psi\Lambda^0\right)} = \quad \frac{N_{obs}[\Lambda_b\to\mu^+\mu^-\Lambda^0(p\pi^-)]}{N_{obs}[\Lambda_b\to J/\psi(\mu^+\mu^-)\Lambda^0(p\pi^-)]} \times\frac{\epsilon_R[\Lambda_b\to J/\psi(\mu^+\mu^-)\Lambda^0(p\pi^-)]}{\epsilon_R[\Lambda_b\to\mu^+\mu^-\Lambda^0(p\pi^-)]} \times\mathcal{B}\left(J/\psi\to\mu^+\mu^-\right) \tag{7.3}$$

Therefore, in order to determine the relative branching ratios for these two decays, it is sufficient to count the number of events observed of each type, and to measure the relative efficiencies. Monte Carlo simulation is used to extract these efficiencies, and as the same way that the Chapter (**??**)

$$\epsilon \equiv \frac{\epsilon_R[\Lambda_b\to J/\psi(\mu^+\mu^-)\Lambda^0(p\pi^-)]}{\epsilon_R[\Lambda_b\to\mu^+\mu^-\Lambda^0(p\pi^-)]} = \quad \frac{N_{reco}^{(MC)}[\Lambda_b\to J/\psi(\mu^+\mu^-)\Lambda^0(p\pi^-)]}{N_{reco}^{(MC)}[\Lambda_b\to\mu^+\mu^-\Lambda^0(p\pi^-)]} \times\frac{N_{gen}^{(MC)}[\Lambda_b\to\mu^+\mu^-\Lambda^0]}{N_{gen}^{(MC)}[\Lambda_b\to J/\psi(\mu^+\mu^-)\Lambda^0]} \times\frac{\epsilon_{d0\_mess}(\Lambda_b\to J/\psi(\mu^+\mu^-)\Lambda^0)}{\epsilon_{d0\_mess}(\Lambda_b\to\mu^+\mu^-\Lambda^0)} \tag{7.4}$$

$N_{reco}^{(MC)}$ and $N_{gen}^{(MC)}$ are evaluated separately for each MC version.

7.3 Pre-selection Requirements

The pre-selection requirementes were the same that for the $\mathcal{B}\left(\Lambda_b^0\to J/\psi\Lambda^0\right)$ analysis, see Chapter (5). The strategy to search for these decays is the following:

- Look for events with two oppositely charged reconstructed muons, forming a common vertex, and with invariant mass $1.2\ GeV/c^2 < Mass(\mu^+\mu^-) < 4.5\ GeV/c^2$, Muons are identified by matching tracks reconstructed in the central tracking system with track segments in the muon spectrometer.

  In this mass region, the J/ψ , Ψ' and ϕ resonances are excluded with cut-out regions that cover $\pm 5\sigma$ wide windows around the observed resonance masses as indicated in Figure 7.2.

  - Region A: $1.2\ GeV/c^2 < Mass(\mu^+\mu^-) < 2.7\ GeV/c^2$.
  - Region B: $4.0\ GeV/c^2 < Mass(\mu^+\mu^-) < 4.5\ GeV/c^2$.

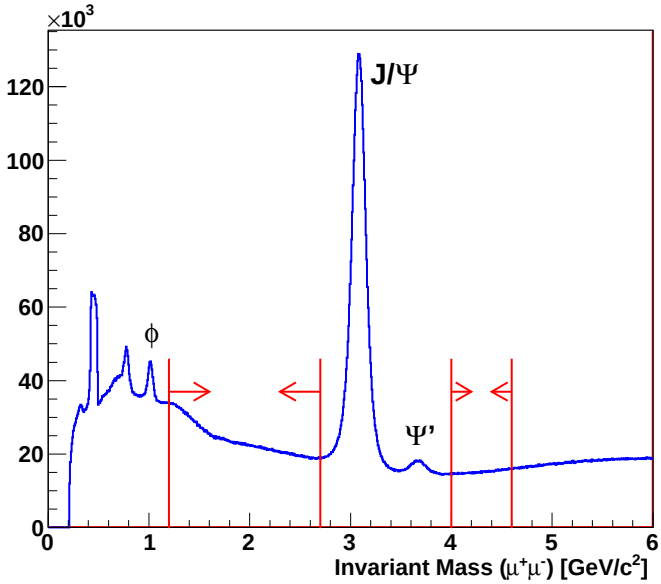

Figure 7.2: The arrows show the regions that are selected

The upper cut of $4.5 GeV/c^2$ in the Mass selection is comming from Monte Carlo. In the Figure 7.5 is shown the generation and recontruction level.

- Search for pairs of oppositely charged tracks with a common vertex in those events satisfying the dimuon selection. For the Λ^0 reconstruction, Monte Carlo (MC) studies support that the track with the highest pT is the proton.

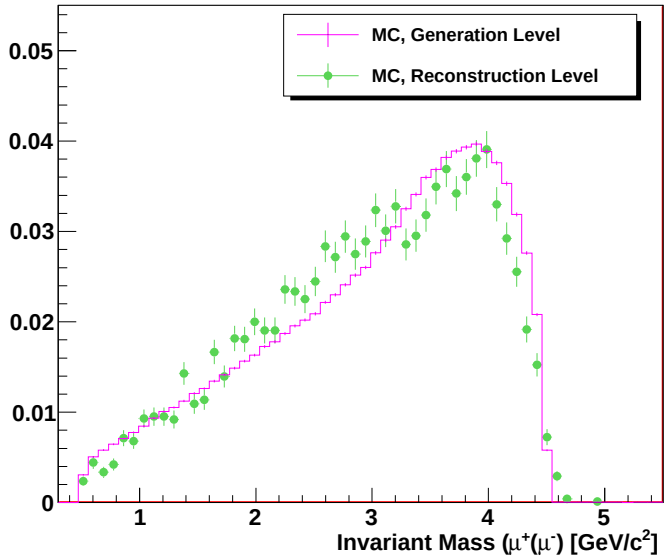

Figure 7.3: DiMuon mass at Generation and Recontruction level in Montecarlo Simulation

- Λ_b^0 candidates are reconstructed by performing a constrained fit to a common vertex of Λ^0 and the two muon tracks.
- Track pairs simultaneously identified as both Λ^0 and K_S^0 due to different mass assignments to the same tracks are removed.
- The pointing angle of the Λ^0 track to the J/Ψ vertex in the transverse plane must not exceed 2.5^o

7.4 Optimisation of Discriminating Variables

An optimisation criterion proposed by G. Punzi [**?**] has been used in order to find the optimal set of cuts. It consists in maximising the ratio P defined as:

$$P = \frac{\epsilon}{\frac{a}{2} + \sqrt{N_{Back}}} \tag{7.5}$$

Here, ϵ is the reconstruction efficiency of the signal Monte Carlo relative to

a preselected sample and N_{Back} is the expected number of background events interpolated from the sidebands. The constant a is the number of standard deviations corresponding to the confidence level at which the signal hypothesis is tested. The value of a should be defined before the statistical test and has been set to 2, corresponding to about 95% CL. The expression P has been used as an optimisation criterion in the grid search.

Before the optimisation of the discriminating variables, the mass region of interest was restricted to 5.3 $GeV/c^2 < M(\Lambda_b) < 5.9 GeV/c^2$, containing the signal region.

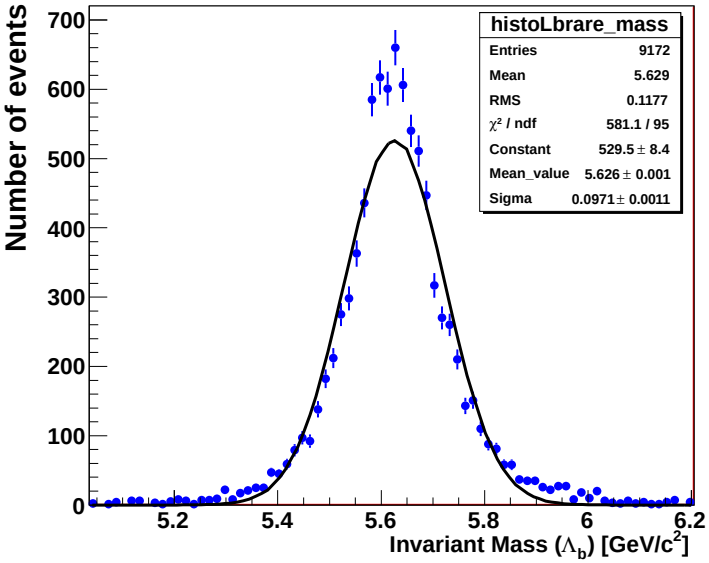

Figure 7.4: The mass resolution in the signal Monte Carlo after pre-selection

The signal region is blinded during the optimisation of cuts to avoid overtuning of the cuts into statistical fluctuations as well as biases in the optimisation procedure.

Table 7.1 defines the mass ranges for the sidebands and the blinded signal region that were used. The given values translate the size of the blind signal region to a window of $800 \pm MeV/c^2$ around the expected reconstructed $\Lambda_b^0 \to \mu^+\mu^-\Lambda^0$ mass. The signal region corresponds to approximately $\pm\ 3\sigma$ of the expected mass resolution for $\Lambda_b^0 \to \mu^+\mu^-\Lambda^0$ in the Monte Carlo. The width of

the sidebands that are used for background estimation was set to 6σ each.

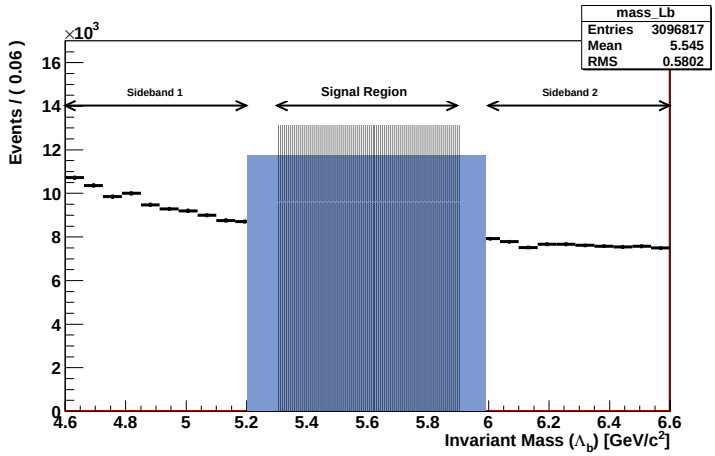

Figure 7.5: Invariant $\Lambda_b^0 \to J/\psi\Lambda^0$ mass distribution of data events after preselection

Table 7.1: Invariant mass regions for signal and sidebands used for background.

Region	min Mass GeV/c^2	max Mass GeV/c^2
region of interest	5.3	5.9
blinded signal	5.2	6.0
sideban I	4.6	5.2
sideban II	6.0	6.6

7.5 Grid Search

The optimisation on the four discriminating variables was performed as described previously. The sideband data sample used during this optimisation corresponded to a third of the total data sample. The result for the cut combination which maximised P of Eq. 7.24 is shown in Table 7.2.

The distributions of the three discriminating variables for signal Monte Carlo and sideband data are shown in Figure 7.6.

Table 7.2: Results from the optimization. In the Column of Final Cut Value are showed the selected cuts.

cut parameter	cut value
P_T (Λ^0)	> 4 GeV/C
Length Decay XY (Λ^0)	> 2 cm
$c\tau/\sigma_{c\tau}$ (Λ^0)	> 16
$c\tau/\sigma_{c\tau}$ (Λ_b^0)	> 12

7.6 Reconstructed MC and data samples

Using Pythia and `d0_mess` , we generate 3 million $\Lambda_b^0 \to \mu^+\mu^-\Lambda^0$ and 3 million $\Lambda_b^0 \to J/\psi\Lambda^0$ events and from these samples, the following `d0_mess`efficiencies are measured:

$$\epsilon_{d0\_mess}(\Lambda_b \to \mu^+\mu^-\Lambda^0) = 0.0055 \pm 0.0001 \tag{7.6}$$
$$\epsilon_{d0\_mess}(\Lambda_b \to J/\psi\Lambda^0) = 0.0130 \pm 0.0001 \tag{7.7}$$

The number of generated decays of each type is:

1. MC for Run IIa:

$$N_{gen}\left(\Lambda_b^0 \to \mu^+\mu^-\Lambda^0\right) = 671,250 \tag{7.8}$$
$$N_{gen}\left(\Lambda_b \to J/\psi(\mu^+\mu^-)\Lambda^0\right) = 725,591 \tag{7.9}$$

2. MC for Run IIb1:

$$N_{gen}\left(\Lambda_b^0 \to \mu^+\mu^-\Lambda^0\right) = 697,500 \tag{7.10}$$
$$N_{gen}\left(\Lambda_b \to J/\psi(\mu^+\mu^-)\Lambda^0\right) = 772,203 \tag{7.11}$$

3. MC for Run IIb2:

$$N_{gen}\left(\Lambda_b^0 \to \mu^+\mu^-\Lambda^0\right) = 862,750 \tag{7.12}$$

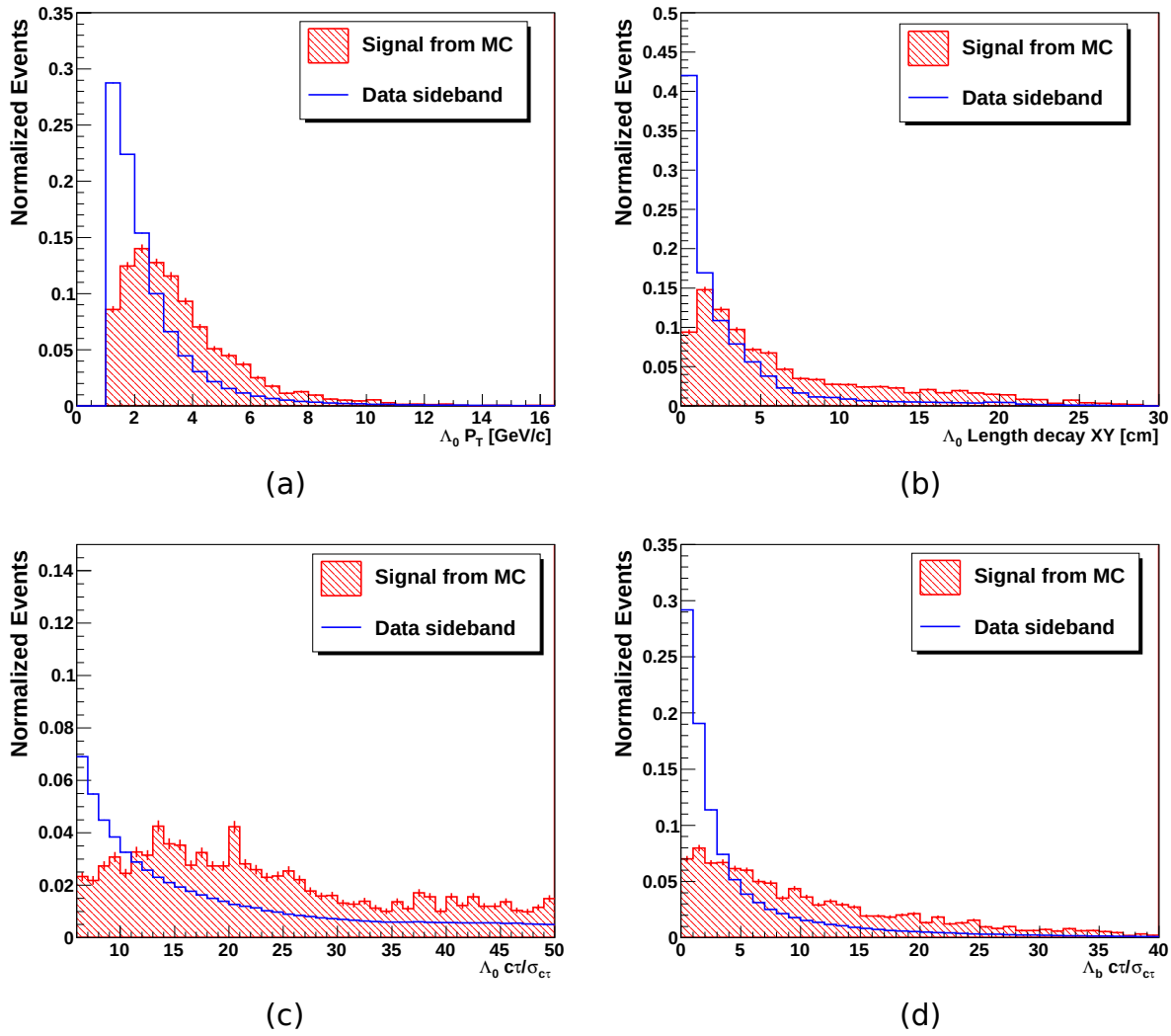

Figure 7.6: Discriminating Variables after pre-selection for signal MC and data events from the sidebands.

$$N_{gen}\left(\Lambda_b \to J/\psi(\mu^+\mu^-)\Lambda^0\right) = 764,817 \tag{7.13}$$

After finalizing the optimized set of analysis cuts, these cuts are applied on data and MC samples. In addition, we select only one $\Lambda_b^0 \to J/\psi\Lambda^0$ candidates per event by choosing the one with best vertex χ^2.

1. MC for Run IIa:

$$N_{reco}^{(MC)}\left(\Lambda_b^0 \to \mu^+\mu^-\Lambda^0\right) = \quad 98 \pm 10 \tag{7.14}$$
$$N_{reco}^{(MC)}\left(\Lambda_b \to J/\psi(\mu^+\mu^-)\Lambda^0(p\pi^-)\right) = \quad 195 \pm 14 \tag{7.15}$$
$$\tag{7.16}$$

2. MC for Run IIb1:

$$N_{reco}^{(MC)}\left(\Lambda_b^0 \to \mu^+\mu^-\Lambda^0\right) = \quad 30 \pm 5 \tag{7.17}$$
$$N_{reco}^{(MC)}\left(\Lambda_b \to J/\psi(\mu^+\mu^-)\Lambda^0(p\pi^-)\right) = \quad 157 \pm 12 \tag{7.18}$$
$$\tag{7.19}$$

3. MC for Run IIb2 and Run IIb3:

$$N_{reco}^{(MC)}\left(\Lambda_b^0 \to \mu^+\mu^-\Lambda^0\right) = \quad 19 \pm 4 \tag{7.20}$$
$$N_{reco}^{(MC)}\left(\Lambda_b \to J/\psi(\mu^+\mu^-)\Lambda^0(p\pi^-)\right) = \quad 61 \pm 7 \tag{7.21}$$
$$\tag{7.22}$$

7.6.1 The normalization channel

In order to obtain a branching ratio limit for $\Lambda_b^0 \to \mu^+\mu^-\Lambda^0$, the decay chain $\Lambda_b^0 \to J/\psi\Lambda^0$ with$J/\Psi \to \mu^+\mu^-$ was used as normalisation. The J/Ψ decaying into $\mu^+\mu^-$ has the big advantage that the $\mu^+\mu^-$ efficiencies are canceled. Therefore, the same cuts on the discriminating variables were applied to $\Lambda_b^0 \to J/\psi\Lambda^0$ as in the $\Lambda_b^0 \to \mu^+\mu^-\Lambda^0$ search.

The mass spectrum of the reconstructed $\Lambda_b^0 \to J/\psi\Lambda^0$ for the full data sample is shown in Figure 7.7. A fit using a Gaussian function for the signal and a second order polynomial for the background yielded 38±8 signal events, where the uncertainty is statistical. The mass resolution of the $\Lambda_b^0 \to J/\psi\Lambda^0$ is $79 MeV/c^2$.

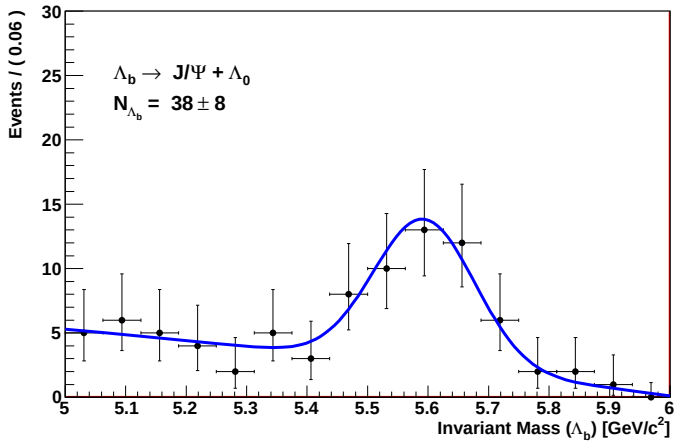

Figure 7.7: Invariant $\Lambda_b^0 \to J/\psi\Lambda^0$ mass distribution of data events after preselection

7.6.2 Efficiencies

The efficiency, ϵ, is the ratio of efficiencies $\frac{\epsilon_{\Lambda_b^0 \to J/\psi\Lambda^0}}{\epsilon_{\Lambda_b^0 \to \mu^+\mu^-\Lambda^0}}$, and as we mentioned before, this value is obtained by:

$$\epsilon = \frac{N^{MCgen}_{\Lambda_b^0 \to \mu^+\mu^-\Lambda^0}}{N^{MCgen}_{\Lambda_b^0 \to J/\psi\Lambda^0}} \cdot \frac{N^{MCreco}_{\Lambda_b^0 \to J/\psi\Lambda^0}}{N^{MCreco}_{\Lambda_b^0 \to \mu^+\mu^-\Lambda^0}} \cdot \frac{\epsilon^{d0mess}_{\Lambda_b^0 \to J/\psi\Lambda^0}}{\epsilon^{d0mess}_{\Lambda_b^0 \to \mu^+\mu^-\Lambda^0}} \tag{7.23}$$

using this equation and the numbers reported in the previos section, plus $\mathcal{B}(J/\psi \to \mu^+\mu^-) = (5.93 \pm 0.06) \times 10^{-2}$ and the results for the three epochs are summarised in Table 7.3

Table 7.3: Summary of the parameter ϵ for the three running epochs.

Run	$\epsilon + \Delta\epsilon$
RunIIa	4.351 ± 0.542
RunIIb1	10.67 ± 1.973
RunIIb2	8.560 ± 2.032

Using 6.3, we found: $\overline{\epsilon} = 5.030 \pm 0.506$

7.7 Deriving an upper limit

To calculate an upper limit on the branching ratio for the decay $\Lambda_b^0 \to \mu^+\mu^-\Lambda^0$, the number of reconstructed events 46 ± 9 of Λ_b^0 decaying into $J/\psi\Lambda^0$ were used as normalisation. Thus, $\mathcal{B}(\Lambda_b^0 \to \mu^+\mu^-\Lambda^0)$ was calculated as:

$$\frac{\mathcal{B}(\Lambda_b^0 \to \mu^+\mu^-\Lambda^0)}{\mathcal{B}(\Lambda_b^0 \to J/\psi\Lambda^0)} = \frac{\mu(n_{obs}, n_{back})}{N_{\Lambda_b^0 \to J/\psi\Lambda^0}} \cdot \epsilon \cdot \mathcal{B}(J/\psi \to \mu^+\mu^-) \tag{7.24}$$

where:

- $\mu(n_{obs}, n_{back})$ is the upper limit on the number of observed events
- ϵ is the efficiencie of the signal and normalisation channel, obtained from Monte Carlo simulation
- the branching ratio $\mathcal{B}(J/\psi \to \mu^+\mu^-) = (5.93 \pm 0.06) \times 10^{-2}$ was taken from PDG.

The efficiencie ϵ is the global signal efficiencies for the search signal and normalisation channel, respectively, including pre-selection cuts, the acceptance and trigger efficiency. They were determined from Monte Carlo and the uncertainties are due to Monte Carlo statistics.

7.8 Sensitivity and Results

The analysis has used the technique of a "blind box" analysis, which means that the signal region was kept hidden throughout all analysis steps presented so far.

Before exploring the "blinded" invariant signal mass region, one can calculate an "expected upper limit", as introduced in Section XX, without knowing the actual number of signal $\Lambda_b^0 \to \mu^+\mu^-\Lambda^0$ events. In Equatio XX the upper limit $\mu(n_{obs}, n_{back})$ has to be replaced by $< (n_{back}) >$. Using the numbers presented in Section XX, without their statistical uncertainties, one obtains a sensitivity of

$$\langle \mathcal{B}(\Lambda_b^0 \to \mu^+\mu^-\Lambda^0) \rangle < 7.77 \times 10^{-5} \tag{7.25}$$

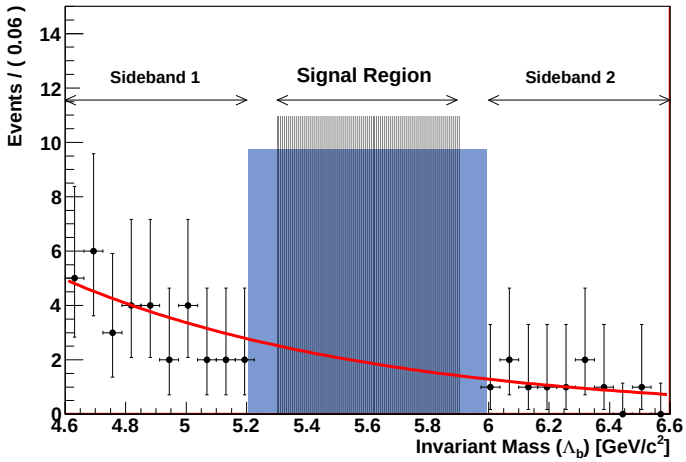

Figure 7.8: The remaining background for the full data sample

at a 95% CL was obtained and

$$\langle \mathcal{B}(\Lambda_b^0 \to \mu^+\mu^-\Lambda^0) \rangle < 6.04 \times 10^{-5} \tag{7.26}$$

at a 90% CL was obtained.

The CDF collaboration reported the first observation of the flavorchanging neutralcurrent decay $\Lambda_b^0 \to \mu^+\mu^-\Lambda^0$ This decay is sensitive to new b physics in the differential branching fraction and asymmetries in angular distributions. CDF reported a signal of 24 ± 5 decays with a significance of about 6 Gaussian sigmas. The branching fraction is

$$\mathcal{B}(\Lambda_b^0 \to \mu^+\mu^-\Lambda^0) = 1.73 \pm 0.69 \times 10^{-6} \tag{7.27}$$

the smallest Λ_b^0 branching fraction yet measured.

Chapter 8

Conclusions

A new measurement of $f(b \to \Lambda_b) \cdot \mathcal{B}\left(\Lambda_b^0 \to J/\psi\Lambda^0\right)$ has been performed and is found to be:

$$f(b \to \Lambda_b) \cdot \mathcal{B}(\Lambda_b \to J/\psi\Lambda) = (6.0 \pm 0.6\ (\text{stat.}) \pm 0.6\ (\text{syst.}) \pm 0.3\ (\mathcal{B})) \times 10^{-5} \quad (8.1)$$

The current world average for this product from the PDG is $(4.7 \pm 2.3) \times 10^{-5}$. This new measurement therefore represents a significant improvement on previous results.

Finally, without requiring many inputs from the PDG, the production cross-section times branching fraction for the decay $\Lambda_b^0 \to J/\psi\Lambda^0$ relative to that for the decay $B_d^0 \to J/\psi K_s^0$ has been measured as:

$$\frac{f(b \to \Lambda_b) \cdot \mathcal{B}(\Lambda_b \to J/\psi\Lambda)}{f(b \to B^0) \cdot \mathcal{B}(B^0 \to J/\psi K_s^0)} = 0.345 \pm 0.034\ (\text{stat.}) \pm 0.033\ (\text{syst.}) \pm 0.003\ (\mathcal{B}) \quad (8.2)$$

The current PDG value is $v = 0.27 \pm 0.13$.

A graphical comparison of the precision of this measurement, with respect to the current PDG values for v and $f(b \to \Lambda_b) \cdot \mathcal{B}(\Lambda_b^0 \to J/\psi\Lambda^0)$, is given in Fig. 8.1.

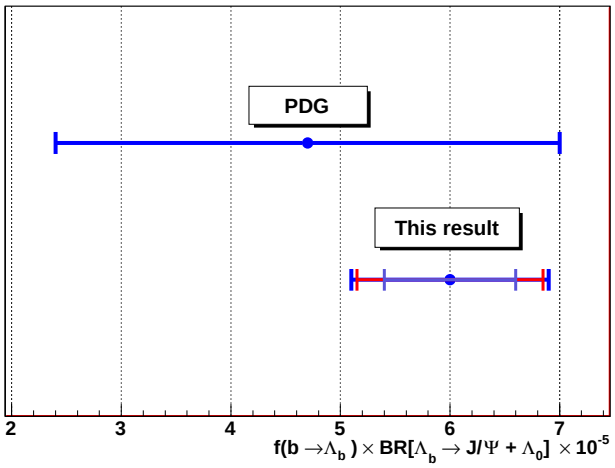

Figure 8.1: Comparison of the precision of this measurement with the current PDG world-averages for v and $f(b \to \Lambda_b) \cdot \mathcal{B}(\Lambda_b^0 \to J/\psi\Lambda^0)$.

An upper limit on the branching fraction $\mathcal{B}(\Lambda_b^0 \to \mu^+\mu^-\Lambda^0)$ was set. Including statistical and systematic uncertainties, and using branching ratio for $\mathcal{B}\left(\Lambda_b^0 \to J/\psi\Lambda^0\right)$ that was estimated previously, a limit of

$$\langle \mathcal{B}(\Lambda_b^0 \to \mu^+\mu^-\Lambda^0) \rangle < 7.77(6.04) \times 10^{-5} \tag{8.3}$$

at a 95% (90%) CL was found

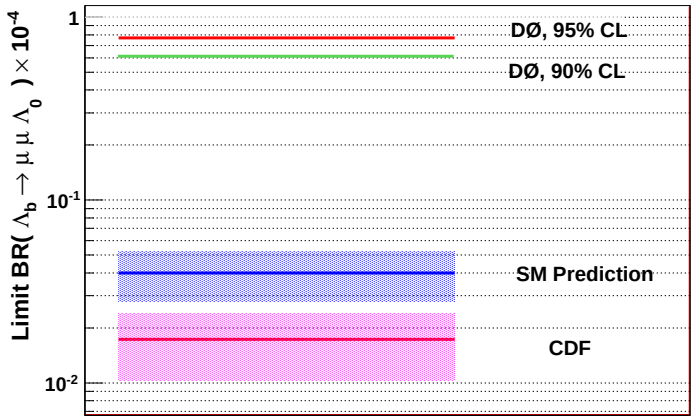

Figure 8.2: Expected average upper limit at a 95% CL and 90% for the decay $\Lambda_b^0 \to \mu^+\mu^-\Lambda^0$

Appdx A

.1 MC configuration

.1.1 MC Samples for the Calculation of $\mathcal{B}\left(\Lambda_b^0 \to J/\psi\Lambda^0\right)$

.1.1.1 Λ_b^0

For these studies we have simulated $p\overline{p}$ collisions using PYTHIA (MSEL=5) and chosen only those events that contain a Λ_b^0 . The Λ_b^0 is forced to decay to $J/\psi\ \Lambda^0$ with the PHSP EvtGen model. The J/ψ is forced to decay to $\mu^+\mu^-$ using VLL and PHOTOS models. The Λ^0 is left to D0gstar (Geant) which manages the decay. Only events with $p_T(\mu^\pm) > 1.5$ GeV and $|\eta(\mu^\pm)| < 2.5$ are saved and fully simulated:

d0_mess.rcp :

```
string Cut1 = "PdgId == 5"
string Cut2 = "PdgId == -5"
string Cut3 = "PdgId == 443 && ParentId == 5122"
string Cut4 = "PdgId == 13 && Pt > 1.50 && AbsEta < 2.5 && ParentId == 443"
string Cut5 = "PdgId == -13 && Pt > 1.50 && AbsEta < 2.5 && ParentId == 443"
string Cut6 = "PdgId == 3122 && ParentId == 5122"
```

user.dec :

```
Alias myJ/psi J/psi
Decay Lambda_b0
1.000 Lambda0    myJ/psi                                  PHSP;
Enddecay
Decay myJ/psi
1.000    mu+  mu-               PHOTOS  VLL;
Enddecay
End
```

.1.1.2 $B_d^0 \to J/\psi K_s^0$

Similarly to the samples of Λ_b^0 , B_d^0 events were simulated, forced to decay to J/ψ $(\mu^+\mu^-)K_S^0$

d0_mess.rcp :

```
string Cut1 = "PdgId == 5"
string Cut2 = "PdgId == -5"
string Cut3 = "PdgId == 443 && ParentId == 511"
string Cut4 = "PdgId == 13 && Pt > 1.50 && AbsEta < 2.5 && ParentId == 443"
string Cut5 = "PdgId == -13 && Pt > 1.50 && AbsEta < 2.5 && ParentId == 443"
string Cut6 = "PdgId == 310 && ParentId == 511"
```

user.dec :

```
noMixing
Alias myJ/psi J/psi
Decay B0
```

```
1.000 K_S0    myJ/psi                                  PHSP;
Enddecay
Decay myJ/psi
1.000    mu+  mu-               PHOTOS  VLL;
Enddecay
End
```

.1.2 MC Samples for the Optimization of $\mathcal{B}\left(\Lambda_b^0 \to J/\psi\Lambda^0\right)$

.1.2.1 Λ_b^0

d0_mess.rcp :

```
string Cut1 = "AbsPdgId == 3122 && AbsParentId == 5122"
string Cut2 = "AbsPdgId == 443 && AbsParentId ==5122"
string Cut3 = "PdgId ==  13 && Pt > 1.0 && AbsEta < 2.5 && AbsParentId == 443"
string Cut4 = "PdgId == -13 && Pt > 1.0 && AbsEta < 2.5 && AbsParentId == 443"
```

user.dec :

```
Alias myJ/psi   J/psi
Decay Lambda_b0
1.000 myJ/psi    Lambda0    PHSP;
Enddecay
Decay anti-Lambda_b0
1.000 myJ/psi    anti-Lambda0    PHSP;
Enddecay
Decay myJ/psi
```

```
1.000 mu+    mu-        PHOTOS VLL;
Enddecay
End
```

.1.2.2 $B_d^0 \to J/\psi K_s^0$

d0_mess.rcp :

```
int NumberOfCuts = 4
string Cut1 = "AbsPdgId == 310 && AbsParentId == 511"
string Cut2 = "AbsPdgId == 443 && AbsParentId ==511"
string Cut3 = "PdgId ==  13 && Pt > 1.0 && AbsEta < 2.5 && AbsParentId == 443"
string Cut4 = "PdgId == -13 && Pt > 1.0 && AbsEta < 2.5 && AbsParentId == 443"
```

user.dec :

```
Alias myJ/psi J/psi
Alias myKshort K_S0
Decay B0
1.000    myJ/psi  myKshort   SVS_CP beta  dm -1 1.0 0.0 1.0 0.0;
Enddecay
Decay anti-B0
1.000    myJ/psi  myKshort   SVS_CP beta  dm -1 1.0 0.0 1.0 0.0;
Enddecay
Decay myJ/psi
1.000    mu+  mu-            PHOTOS  VLL;
Enddecay
End
```

.2 MC Samples

.2.1 Λ_b^0

Now is showed the invariant mass distributions for Λ_b^0 , Λ^0 and J/ψ

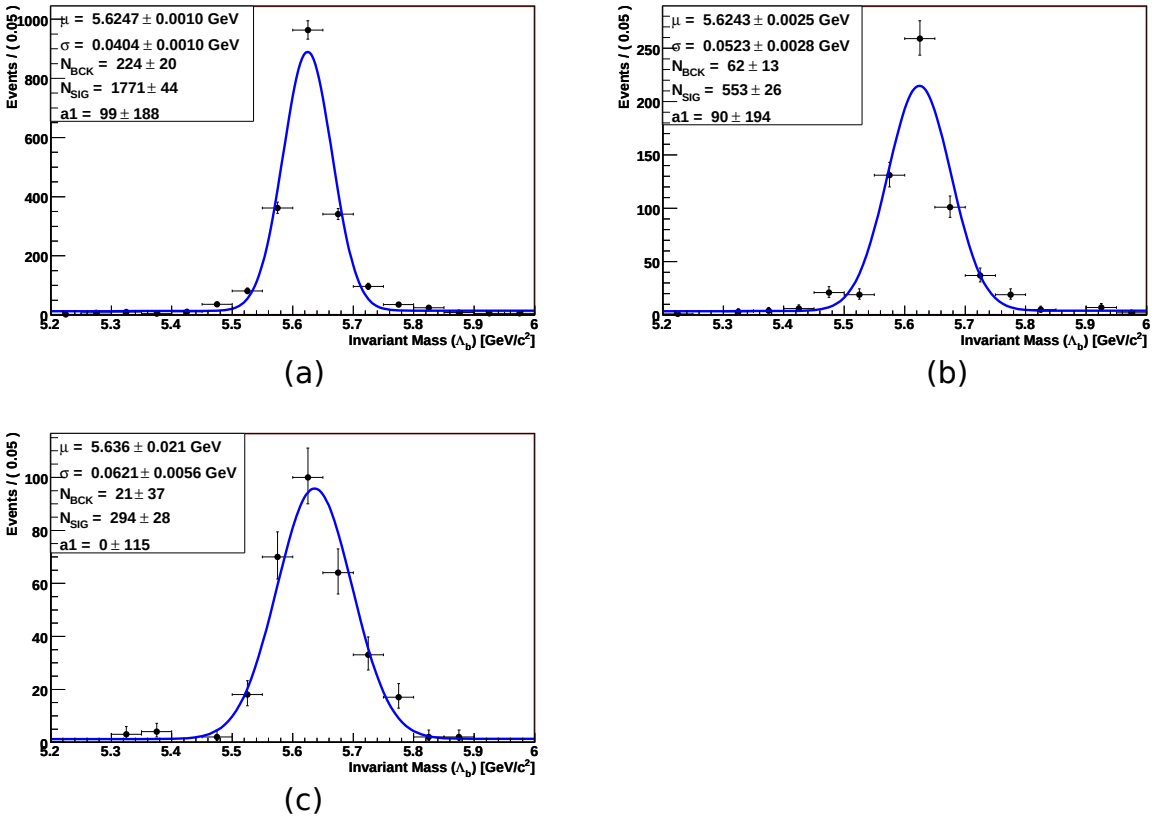

Figure 3: Monte Carlo sample of Λ_b^0 mass in *a*) p17 Run IIa, *b*) p20 Run IIb1 and *c*) p20 Run IIb2

.2.2 $B_d^0 \to J/\psi K_s^0$

Now is showed the invariant mass distributions for B_d^0 , K_S^0

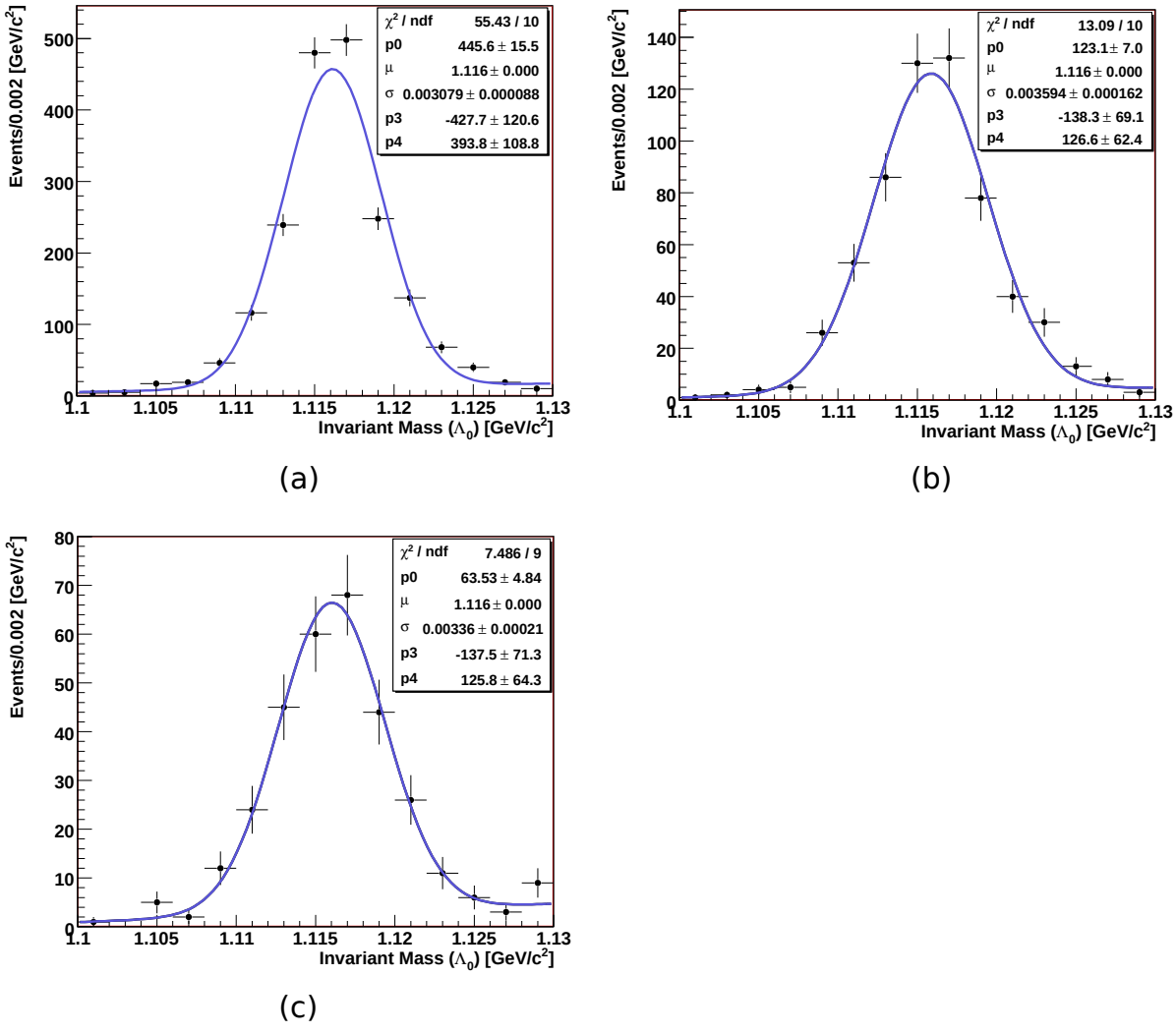

Figure 4: Monte Carlo sample of Λ^0 mass in *a*) p17 Run IIa, *b*) p20 Run IIb1 and *c*) p20 Run IIb2

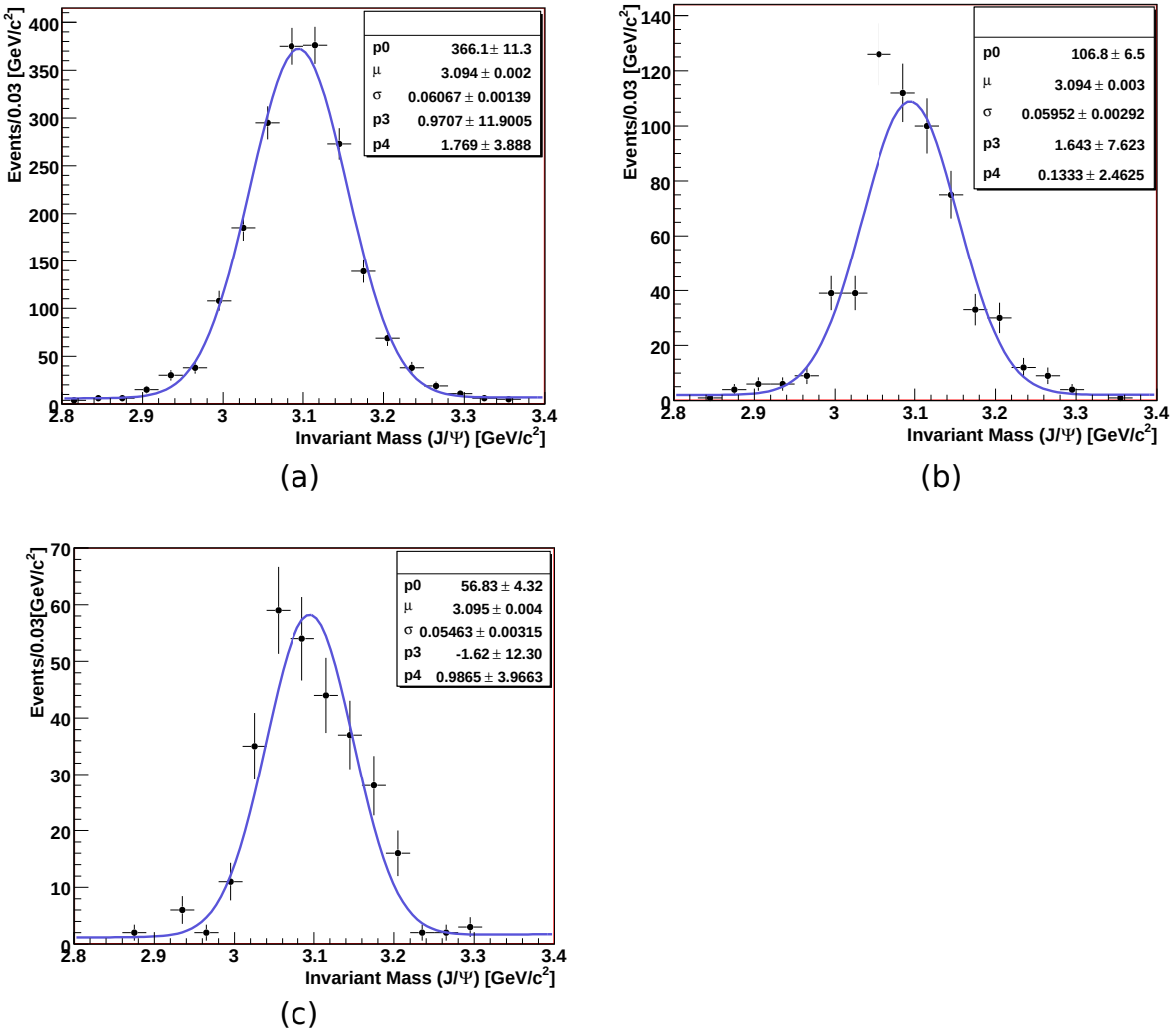

Figure 5: Monte Carlo sample of J/ψ mass in *a*) p17 Run IIa, *b*) p20 Run IIb1 and *c*) p20 Run IIb2

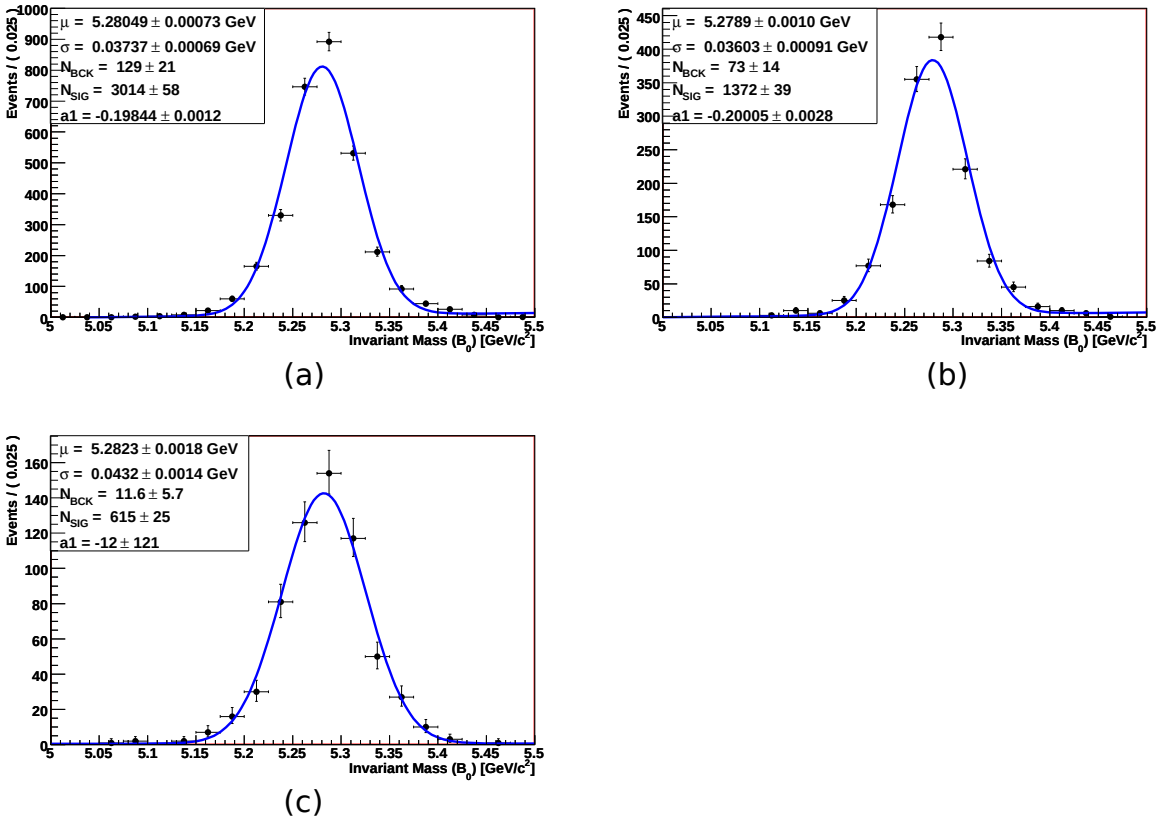

Figure 6: Monte Carlo sample of Λ_b^0 mass in *a*) p17 Run IIa, *b*) p20 Run IIb1 and *c*) p20 Run IIb2

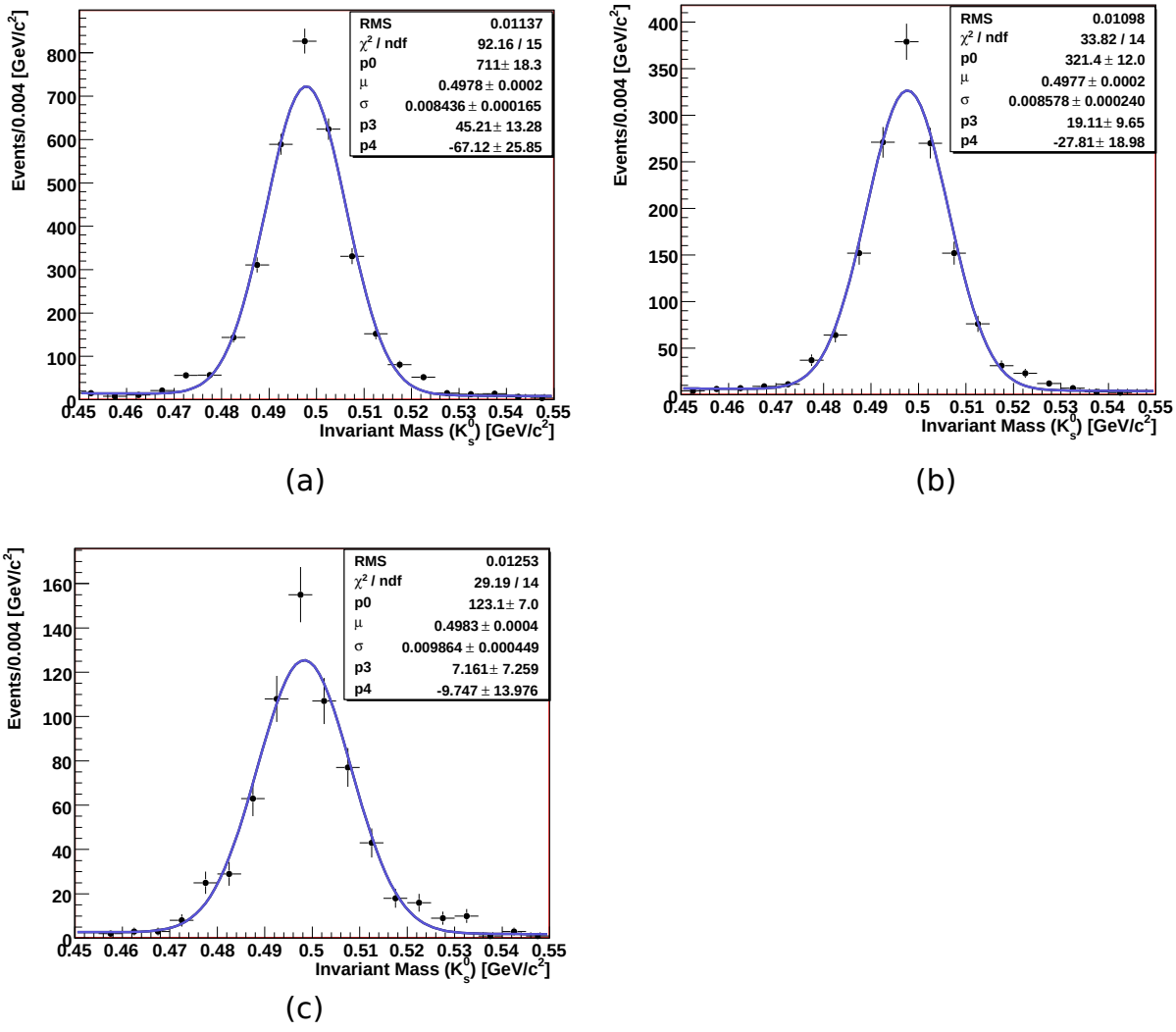

Figure 7: Monte Carlo sample of Λ^0 mass in *a*) p17 Run IIa, *b*) p20 Run IIb1 and *c*) p20 Run IIb2

Calculating Limits

.3 Probabilities

The most common definition of a probability is the Frequentist approach. If an identical experiment is performed N times, and a certain outcome A occurs M times then the probability $p(A)$ for the event A to occur tends to the ratio M/N as $N \to \infty$. The set of all N cases is called a collective or ensemble and can be obtained by repeating one experiment N times or by measuring N experiments simultaneously. This is a very useful definition but also has some problems. One problem is the repeatability of an experiment. How can it be ensured that the conditions between the experiments have not changed and that the initial conditions are exactly the same? The next problem is that the limit $N \to \infty$ in a strict mathematical interpretation does not exist. How can one deduce from N experiments the outcome of the $N+1st$ experiment? Also, when does it converge to the limit? Nobody can perform an infinite number of experiments.

Another definition is that of a subjective probability, also known as the Bayesian definition of probability. This definition is based on the plausibility or credibility of the observed occurrence. It allows to test the probability of a hypothesis, which is not defined in the Frequentist approach. In the Bayesian definition, the actual knowledge about the observed event is taken into account, which makes this definition of probability subjective. The probability $p(A)$ depends on the information the observer has and transforms it into a degree of belief. If subsequent experiments are performed, the initial degree of belief can be modified, depending on the additional information obtained.

.4 Confidence Intervals

.5 Confidence Intervals for Poisson Distributions

.6 Observing fewer Events than Expected

.7 Expected Upper Limit

Phys.Rev. D84 (2011) 031102

Measurement of the procucion faction times branching faction...
doi: 10.1103/PhysRevD.84.031102
Article removed due to copyright

Result of the week at Fermilab

Every Thursday, a new Fermilab Result of the Week appears in Fermilab Today. Results of the Week highlight science from Fermilab experiments. Each Result of the Week is a showcase of the scientific research and results achieved at Fermilab.

The DZero spokesmen designated my analysis of the $f(b \to \Lambda_b) \cdot \mathcal{B}\left(\Lambda_b^0 \to J/\psi \Lambda^0\right)$ to be translated for the public and be published in the Fermilab Today at May 5, 2011.

Fermilab Today May 5, 2011

Result of the week

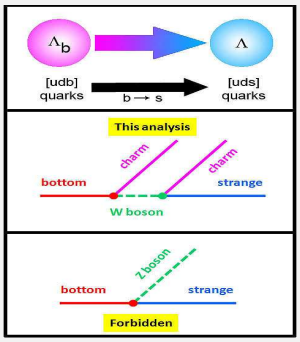

The Standard Model forbids direct production of a strange quark from the decay of a bottom. Indirect decay of the kind illustrated here is possible and is the focus of this analysis. Since observation of direct production of strange quarks from bottom quarks would indicate a discovery, we need to understand very well the indirect production described here.

Subatomic particles called quarks are some of the building blocks of our universe. The heaviest of the six types of quarks are the top and the bottom quark, and the bottom quark is where we begin our story.

Today's result explores the decay of a particle called the Λb (pronounced lambda sub b), which contains an up, down and bottom quark, into a regular Λ (lambda) particle, which contains an up, down and strange quark. This decay requires the transmutation of the bottom quark to a strange one.

Historically, the quark type is called flavor, so when a quark decays from one kind to another, we call it flavor changing. If the bottom quark could decay this way, it would do so by emitting a neutral particle, since the bottom, strange and down quarks all have the same electric charge. Because of this, physicists call a possible decay of a bottom quark into a strange quark a flavor-changing neutral current or FCNC.

According to the Standard Model, FCNCs are impossible and to observe one would be a sign of new and interesting physics (and a trip to Stockholm). However, we need to be careful: It is only impossible for a bottom quark to directly decay into a strange quark. The Standard Model allows indirect decays of bottom quarks into strange ones (see above figure). This happens when a bottom quark turns into a charm quark and a W boson, followed by a subsequent decay of the W into a charm quark and a strange quark. This kind of indirect decay is the basis of today's result. Given that observing direct FCNC would be the sign of a very surprising discovery, we need to understand very well the phenomenon of indirect FCNC so we can account for it in our calculations.

The precision of the measurements in this study are over three times better than all earlier measurements combined. This is a necessary achievement if we ever hope to convincingly observe direct flavor changing neutral currents.

— Don Lincoln

Enrique Camacho-Perez | Eduard de la Cruz-Burelo | Ivan Heredia de la Cruz

These physicists from CINVESTAV in Mexico performed this analysis.

My service on site

As a member of the DØ experiment my main physics interest has been b-physics, where I developed a new analysis that aimed to measure the branching ratio $\mathcal{B}(\Lambda_b \to J/\psi\Lambda^0)$, which improved the precision by a factor of 3 compared to the previous Tevatron result. With this result the CDF experiment was able to report the branching ratio $\mathcal{B}(\Lambda_b \to \mu\mu\Lambda^0)$, and they found no significant deviation from the Standard Model

Apart from my specific analysis I was an active member in the DØ community. I gave a talk at SUSY 2011 conference related to the first search for pair production of isolated jets of charged leptons in association with a large imbalance in transverse energy in $p\bar{p}$ collisions using 5.8 fb^{-1} of integrated luminosity collected by the DØ detector.

I contributed to the operation of the detector by getting involved in two detector sub groups as both DAQ shifter and L2 trigger expert. I had an active role in the data taking group, where I was responsible for maximizing data taking efficiency during 1064 hours of DAQ shifts, beyond of my own DAQ shifts, I took an interest in helping other DAQ shifters, by streamlining the procedures at the start and end of stores, by training 8 new DAQ shifters, and by giving L2 tutorials. In recognition of these contributions to the detector operations, I was invited to be part of the team of 8 people in the control room for the last Tevatron store. As a L2-expert I covered 41 weeks as primary on-call expert, this means that I was responsible for fixing problems with the L2 system at any time of the day or night as rapidly as possible to maintain efficient data taking. I also worked to improve the overall performance of L2. I performed studies in the sync-errors and missing inputs, both related with the muon system, with these studies I contributed to

developing a GUI to detect Muon sync-errors that only the L2 system was able to detect. This tool helped to avoid possible stops in the data taking.

Figure 8: The DZero L2 group: These physicists monitor and maintain one of the critical trigger systems that ensure data flow. From left to right: Enrique Camacho, CINVESTAV, Mexico; Shannon Zelitch, University of Virginia; James Kraus, Michigan State University; Mandy Rominsky, University of Oklahoma; Joel Piper, Michigan State University; Emmanuel Munyangabe, University of Virginia. On the TV screen is Bob "Max Headroom" Hirosky, University of Virginia.

Figure 9: This group of data acquisition shifters have undertaken a major commitment to operate the DZero detector and take 42 shifts during the course of four months. They are responsible for ensuring that the data is efficiently collected and moved to tape. The physicists shown above are just a fraction of the people involved.

Figure 10: Last crew for data taking at DZero detector at September 30, 2011. From left to right Stefan Gruenendahl, Horst Wahl, George Ginther , Yuriy Yatsunenko , Jadzia Warchol, Bill Frank, Enrique Camacho-Perez, Joe Haley, Dean Schamberger and Bill Lee.

CURRICULUM VITAE

Enrique Camacho Pérez

Physics Department
CINVESTAV-IPN
Av. IPN 2508, Col. San Pedro Zacatenco,
Mexico City, Mexico, 07360
http://www-clued0.fnal.gov/~ecamacho/

Phone: +(52) 55-5747 3831
Fax: +(52) 55-5747 3838
Email: ecamacho@fis.cinvestav.mx

E D U C A T I O N

- **Ph.D.**, Physics 2008 - present
  CINVESTAV-IPN, Mexico City, Mexico
  Advisor: Eduard de la Cruz Burelo
  Thesis title: *Measurement of* $\mathcal{B}(\Lambda_b^0 \to J/\Psi\Lambda_0)$ *at DØ experiment*
- **M. Sc.**, Physics 2005 - 2007
  CINVESTAV-IPN, Mexico City, Mexico
  Advisor: Luis Manuel Montaño Zetina
  Thesis title: *Calibration of the V0A detector and study of longitudinal polarization of* Λ^0 *in the ALICE experiment at CERN*
- **B. Sc.**, Physical Engineering 2000 - 2005
  Universidad Autonoma de Yucatan, Merida, Mexico
  Advisor: Guillermo Contreras Nuño
  Thesis title: *Study of the light transmission in scintillator plastics for the V0A detector of the ALICE experiment at CERN*

F E L L O W S H I P S

- **Aug 2008 - present:** Fellow granted by *CONACyT* in order to obtain the Ph. D. degree.
- **Nov 2008 - Oct 2011:** Fellow granted by *Fermilab Research Alliance, LLC* at Fermilab, USA.
- **Nov 2010 - Jan 2011:** Fellow granted by *Redes Tematicas CONACyT De Investigacion* at Fermilab, USA.
- **Apr 2007 - Oct 2007:** Fellow granted by *HELEN (High Energy Physics Latinamerican-European Network)* at CERN, Switzerland.
- **Sept 2005 - Aug 2007:** Fellow granted by *CONACyT* in order to obtain the M. Sc. degree.

- **Sept 2004- Sept 2005:** Fellow granted by *CONACyT*, in the project "Physics of the Quark−Gluon Plasma in the ALICE experiment" in order to obtain the B. Sc. degree.
- **Jun 2005 - Aug 2005:** Fellow *"IV Summer program for the scientific research"* at CINVESTAV-Merida, granted by the Universidad Autonoma de Yucatan.
- **Jun 2004 - Sept 2004:** Fellow *"X Summer program for the scientific research"* at CINVESTAV-Mexico and ICN-UNAM, granted by the Mexican Academy of Science.
- **Jun 2003 - Aug 2003:** Fellow *"II Summer program for the scientific research"* at CINVESTAV-Merida, granted by the Universidad Autonoma de Yucatan.

H E P E X P E R I E N C E

- **Fermilab (Nov 2008 - Oct 2011):** Member of the B-Physics group of the DØ experiment at Fermilab, USA.
  - Measurement of the branching ratio $\mathcal{B}(\Lambda_b^0 \to J/\Psi\Lambda_0)$.
  - First searchers decays $\Lambda_b^0 \to \mu\mu\Lambda_0$ and $\Lambda_b^0 \to \Psi(2s)\Lambda_0$.
- **Fermilab (Nov 2008 - Oct 2011):** Expert of the L2-trigger in the DØ experiment at Fermilab, USA.
  - 41 weeks covered as primary expert.
  - Control and monitoring developer for the L2-trigger.
  - Developed a GUI for monitoring the sync-errors from Muon-L2 trigger system.
- **Fermilab (Jan 2009 - Oct 2011):** Member of the data acquisition system group in the DØ experiment at Fermilab, USA.
  - Responsible for maximizing data taking efficiency during 1064 hours of DAQ shifts.
  - 8 trained DAQ shifters
  - Ensured that the DAQ system keeps data flowing and recording.
  - Investigated and solved sources of data flow interruption or redirected to the appropiate subdetector expert.
  - Due to the dedication, the effort and to the amount of DAQ shifts done during my stay at DØ, I was invited to be part of the crew for the last DAQ shift in the DØ control room, participating directly in the activities associated with the conclusion of the final Tevatron store.
- **Fermilab (Jul 2010):** Participation in the *Tevatron roll measurements* during the July Tevatron-Shutdown with measuring the rolls on the Tev dipoles and quads. at Fermilab, USA.
- **CERN (Apr 2007 - Oct 2007):** I was part of the crew that mounted the V0A detector for the ALICE experiment in the PS test beam at CERN. I was also responsible in the data analysis for determining the performance of that detector.

- **CINVESTAV-Mexico and ICN-UNAM (Jun 2004 - Sept 2004):** I was responsible for testing a PCI-DAQ card developed for the Mexican Collaboration in ALICE. This card was designed for the characterization of the 60 ACORDE modules.

T A L K S

- **"Search for events with leptonic jets and missing transverse energy in $p\bar{p}$ collisions at DØ Experiment"** SUSY 2011 (19th International Conference on Supersymmetry and the Unification of Fundamental Interactions), Fermilab, USA, August 2011.
- **"Measurement of $\mathcal{B}(\Lambda_b^0 \to J/\Psi\Lambda_0)$ using 6.1 fb^{-1} of DØ data"** April Meeting of the American Physical Society, California, USA, May 2011.
- **"Paper presentation: Measurement of the branching ratio $\mathcal{B}(\Lambda_b^0 \to J/\Psi\Lambda_0)$"** All DØ Meeting, Fermilab, USA, April 2011.
- **"Protocol modules characterization of the ACORDE detector"** II Meeting of Summer Students, Yucatan, Mexico, Sept 2004.

M A I N P U B L I C A T I O N S A N D N O T E S

- **"Measurement of the production fraction times branching fraction $f(b \to \Lambda_b) \cdot \mathcal{B}(\Lambda_b \to J/\psi\Lambda)$"**
  Phys. Rev. **D84**, 031102 (2011).
  arXiv:1105.0690
- **" Measurement of the Branching Ratio $\mathcal{B}(\Lambda_b^0 \to J/\Psi\Lambda_0)$ using 6.1 fb^{-1} of Run II Data "**
  Internal D0 Note 6155 (2011).
- **"Analysis of the longitudinal anti-Λ_0 polarization in ALICE"**
  E. Camacho, L. Montano, D. Perez-Astudillo
  Proceedings of the XI Mexican Workshop on Particles and Fields, Tuxtla Gutierrez, Chiapas, Mexico, AIP Conf.Proc. 1026 (2008) 254-258
- **"Results of the calibration for the V0A detector with a beam of negative pions "**
  R. Alfaro, A. Anzo, E. Belmont-Moreno, Gonzalez-Trueba , H. Leon, A. Menchaca-Rocha, A. Sandoval, G. Herrera-Corral, L.M. Montano, E. Camacho.
  L Mexican Physics Meeting at Veracruz, Mexico, (2007).
- **"PCI DAQ card for experiments of high energy physics "**
  S. Vergara, G. Paic, M. A. Vargas, G. Tejeda, E. Camacho and A. Fernandez.
  INTERNAL NOTE ICN/LD/04-04 Version 1.00, (2004)

T E A C H I N G A C T I V I T I E S

- **Jan. 2010 - May 2010:** Teaching Assistant for a course in "Quantum Mechanics I" at the Physics Department, CINVESTAV-IPN, Mexico City, Mexico.

- **Jan. 2010 - May 2010:** Teaching Assistant for a course in "Introduction to Classical Mechanics" at the Physics Department, CINVESTAV-IPN, Mexico City, Mexico.
- **Jan. 2010 - May 2010:** Teaching Assistant for a course in "Introduction to Thermodynamics" at the Physics Department, CINVESTAV-IPN, Mexico City, Mexico.
- **May. 2010:** Lecturer for a course in "Introduction to Mathematica" at the Physics Department, CINVESTAV-IPN, Mexico City, Mexico.
- **Apr. 2009:** Shifter Tutorial at DØ experiment "Level 2 Trigger System" Fermilab,USA.

L A N G U A G E S K I L L S

- **Spanish**, Mother tongue.
- **English**, Fluent.
- **French**, Intermediate.

P R O G R A M M I N G S K I L L S

- Windows and Linux platforms
- Programming languages: C++, Python and Bash.
- Software: Wolfram Mathematica, LaTex editor, Corel Draw and ROOT.
- Web page development: HTML and PHP.
- Software framework for DØ experiment

F U L L P U B L I C A T I O N L I S T

- V. M. Abazov *et al.* [DØ], Phys. Rev. Lett. **107**, 121802 (2011).
- V. M. Abazov *et al.* [DØ], Phys. Rev. Lett. **107**, 011804 (2011).
- V. M. Abazov *et al.* [DØ], Phys. Rev. **D84**, 012007 (2011).
- V. M. Abazov *et al.* [DØ], Phys. Rev. Lett. **105**, 211803 (2010).
- V. M. Abazov *et al.* [DØ], Phys. Rev. **D82**, 011102 (2010).
- V. M. Abazov *et al.* [DØ], Phys. Lett. **B690**, 108-117 (2010).
- V. M. Abazov *et al.* [DØ], Phys. Lett. **B693**, 531-538 (2010).
- V. M. Abazov *et al.* [DØ], Nucl. Instrum. Meth. **A620**, 490-517 (2010).
- V. M. Abazov *et al.* [DØ], Phys. Rev. Lett. **104**, 061802 (2010).
- V. M. Abazov *et al.* [DØ], Phys. Rev. Lett. **104**, 061804 (2010).
- V. M. Abazov *et al.* [DØ], Phys. Lett. **B693**, 515-521 (2010).
- V. M. Abazov *et al.* [DØ], Phys. Rev. Lett. **104**, 071801 (2010).
- V. M. Abazov *et al.* [DØ], Phys. Rev. **D81**, 052012 (2010).

- V. M. Abazov *et al.* [DØ], Phys. Lett. **B690**, 5-14 (2010).
- V. M. Abazov *et al.* [DØ], Phys. Rev. Lett. **104**, 151801 (2010).
- V. M. Abazov *et al.* [DØ], Phys. Rev. Lett. **104**, 061801 (2010).
- V. M. Abazov *et al.* [DØ], Phys. Rev. **D82**, 032002 (2010).
- V. M. Abazov *et al.* [DØ], Phys. Rev. **D80**, 111107 (2009).
- K. Aamodt *et al.* [ALICE], Phys. Rev. **D82**, 052001 (2010).
- K. Aamodt *et al.* [ALICE], Phys. Lett. **B693**, 53-68 (2010).
- K. Aamodt *et al.* [ALICE], Phys. Rev. Lett. **105**, 072002 (2010).
- K. Aamodt *et al.* [ALICE], Eur. Phys. J. **C68**, 89-108 (2010).
- K. Aamodt *et al.* [ALICE], Eur. Phys. J. **C68**, 345-354 (2010).
- K. Aamodt *et al.* [ALICE], JINST **5**, P03003 (2010).
- K. Aamodt *et al.* [ALICE], Eur. Phys. J. **C65**, 111-125 (2010).

List of Figures

List of Tables

References

[1] C. Albajar *et al.* [UA1 Collaboration], Phys. Lett. B **273**, 540 (1991). 3

[2] F. Abe *et al.* [CDF Collaboration], Phys. Rev. D **47**, 2639 (1993). 3

[3] F. Abe *et al.* [CDF Collaboration], Phys. Rev. D **55** (1997) 1142. 3, 31

[4] P. Abreu *et al.* [DELPHI Collaboration], Phys. Lett. B **289**, 199 (1992). 5
P. D. Acton *et al.* [OPAL Collaboration], Phys. Lett. B **295**, 357 (1992).
D. Buskulic *et al.* [ALEPH Collaboration], Phys. Lett. B **361**, 221 (1995).

[5] P. Abreu *et al.* [DELPHI Collaboration], Z. Phys. C **68**, 375 (1995).

[6] R. Barate *et al.* [ALEPH Collaboration], Eur. Phys. J. C **2**, 197 (1998).

[7] D. Buskulic *et al.* [ALEPH Collaboration], Phys. Lett. B **384**, 449 (1996). 5

[8] J. Abdallah *et al.* [DELPHI Collaboration], Eur. Phys. J. C **44**, 299 (2005) [hep-ex/0510023]. 5

[9] P. Abreu *et al.* [DELPHI Collaboration], Z. Phys. C **68**, 541 (1995). 5

[10] R. Barate *et al.* [ALEPH Collaboration], Eur. Phys. J. C **5** (1998) 205. 5

[11] J. Abdallah *et al.* [DELPHI Collaboration], Phys. Lett. B **576**, 29 (2003) [hep-ex/0311005]. 5

[12] T. Affolder *et al.* [CDF Collaboration], Phys. Rev. Lett. **84**, 1663 (2000) [hep-ex/9909011]. 5

[13] T. Aaltonen *et al.* [CDF Collaboration], Phys. Rev. D **77**, 072003 (2008) [arXiv:0801.4375 [hep-ex]]. 5

[14] T. Aaltonen *et al.* [CDF Collaboration], Phys. Rev. D **79**, 032001 (2009) [arXiv:0810.3213 [hep-ex]]. 5

[15] F. Abe *et al.* [CDF Collaboration], Phys. Rev. D **60** (1999) 092005. 5

[16] V. M. Abazov *et al.* [D0 Collaboration], Phys. Rev. Lett. **99**, 052001 (2007) [arXiv:0706.1690 [hep-ex]]. 6, 75

[17] V. M. Abazov *et al.* [D0 Collaboration], Phys. Rev. Lett. **101**, 232002 (2008) [arXiv:0808.4142 [hep-ex]]. 6

[18] T. Aaltonen *et al.* [CDF Collaboration], Phys. Rev. D **80**, 072003 (2009) [arXiv:0905.3123 [hep-ex]]. 6

[19] D. Abbaneo *et al.* [ALEPH and CDF and DELPHI and L3 and OPAL and SLD Collaborations], hep-ex/0009052. 6

[20] Abazov *et al.* [D0 Collaboration], Phys. Rev. Lett. **94**, 102001 (2005) 8

[21] Abazov *et al.* [D0 Collaboration], Phys. Rev. Lett. **99**, 142001 (2007) 8

[22] Abazov *et al.* [D0 Collaboration], Phys. Rev. Lett. **99**, 182001 (2007)

[23] Abazov *et al.* [D0 Collaboration], Phys. Rev. Lett. **99**, 052001 (2007) 8

[24] Abazov *et al.* [D0 Collaboration], Phys. Rev. Lett. **101**, 232002 (2008) 8

[25] A. Ali, P. Ball, L. T. Handoko and G. Hiller, Phys. Rev. D **61**, 074024 (2000) [hep-ph/9910221]. 9

[26] D. Melikhov, N. Nikitin and S. Simula, Phys. Rev. D **57**, 6814 (1998) [hep-ph/9711362]. 9

[27] Q. Chang and Y. -H. Gao, Nucl. Phys. B **845** (2011) 179 [arXiv:1101.1272 [hep-ph]]. 9

[28] Y. -M. Wang, M. J. Aslam and C. -D. Lu, Eur. Phys. J. C **59**, 847 (2009) [arXiv:0810.0609 [hep-ph]]. 9

[29] Y. -m. Wang, Y. Li and C. -D. Lu, Eur. Phys. J. C **59**, 861 (2009) [arXiv:0804.0648 [hep-ph]]. 10

[30] C. -H. Chen and C. Q. Geng, Phys. Rev. D **64**, 074001 (2001) [hep-ph/0106193]. 10

[31] T. M. Aliev, K. Azizi and M. Savci, Phys. Rev. D **81**, 056006 (2010) [arXiv:1001.0227 [hep-ph]]. 10

[32] M. J. Aslam, Y. -M. Wang and C. -D. Lu, Phys. Rev. D **78**, 114032 (2008) [arXiv:0808.2113 [hep-ph]]. 10

[33] T. Aaltonen *et al.* [CDF Collaboration], Phys. Rev. Lett. **107**, 201802 (2011) [arXiv:1107.3753 [hep-ex]]. 10

[34] V. M. Abazov *et al.* [D0 Collaboration], Nucl. Instrum. Meth. A **565**, 463 (2006) [physics/0507191 [physics.ins-det]]. 13

[35] S. Abachi *et al.* [D0 Collaboration], Phys. Rev. Lett. **74**, 2632 (1995) 13

[36] T. Sjostrand, L. Lonnblad and S. Mrenna, [arXiv:hep-ph/0108264]. 28

[37] D. J. Lange, NIM A **462** 152 (2001); `http://www.slac.stanford.edu/~lange/EvtGen` 28

[38] DZero Montecarlo Event Selection System, `http://www-clued0.fnal.gov/d0_mess/` 28

[39] Y. Fisyak, J. Womersley, DGSTAR: DGEANT Simulation of the Total Apparatus Response, DØ Note **3191** (1997). 28

[40] S. Youssef et al., DSIM User Manual, DØ Note **407** (1986). 28

[41] Application Software Group, Detector Description and Simulation Tool,CERN Program L 28

[42] V. M. Abazov *et al.* [D0 Collaboration], Phys. Rev. Lett. **99**, 052001 (2007) [arXiv:0706.1690 [hep-ex]]. 6, 75